9810509

EVALUATION OF ISOCLINIC PARAMETER IN DIGITAL PHOTOELASTICITY

by
VINAYAK YESHWANT GADRE

TH
ME/2000/M
G1117e

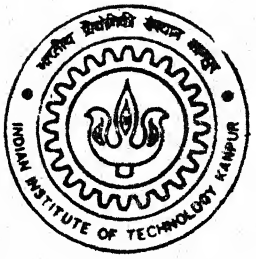

DEPARTMENT OF MECHANICAL ENGINEERING
INDIAN INSTITUTE OF TECHNOLOGY KANPUR

February, 2000

EVALUATION OF ISOCLINIC PARAMETER IN DIGITAL PHOTOELASTICITY

A Thesis Submitted
in Partial Fulfillment of the Requirements
for the Degree of

MASTER OF TECHNOLOGY

February, 2000

by

VINAYAK YESHWANT GADRE

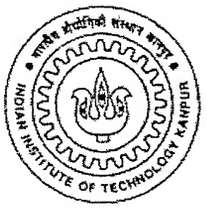

DEPARTMENT OF MECHANICAL ENGINEERING
INDIAN INSTITUTE OF TECHNOLOGY
KANPUR – 208016 (INDIA)

15 MAY 2000 ME
CENTRAL LIBRARY
I. I. T., KANPUR
A 130863
Th
ME/2000/M
G117c
A130863

CERTIFICATE

25.02.2000

It is certified that the work contained in the thesis entitled, "EVALUATION OF ISOCLINIC PARAMETER IN DIGITAL PHOTOELASTICITY" by *Mr. Gadre Vinayak Yeshwant* has been carried out under my supervision and that this work has not been submitted elsewhere for a degree.

25/2/2000

(Dr. K. Ramesh)
Professor
Department of Mechanical Engineering,
Indian Institute of Technology, Kanpur.

February, 2000

ACKOWLEDGEMENTS

I wish to express my deep sense of gratitude and indebtedness towards Dr. K. Ramesh for his inspiring guidance, invaluable suggestions and constructive criticism. He was always a constant source of encouragement throughout my thesis work.

I am very much thankful to Dr. S. K. Mangal for his support to me. I thank my friends Dhiraj, Rohit and Anant for their help to me. I would like to thank my all friends for making my stay at IITK memorable.

I appreciate the help provided by Mr. Radheshayam and Mr. Lavendra for conducting the experiments. I express my thanks to ESA laboratory staff for extending their assistance. I thank all those who have contributed directly or indirectly to my thesis.

ABSTRACT

Photoelasticity is an optical method of experimental stress analysis, which yields a whole field representation of the principal stress difference and its orientations. With advancements in digital image processing techniques applied to photoelasticity it has now became possible to get fringe order and isoclinics at every pixel in the domain. Usually the retardation calculated is represented in the form of a phase map. Due to isoclinic-isochromatic interaction on isochromatics, the phase map has ambiguity in the sign of fractional retardation in some zones. The present work discusses different methods of improving the phase map at least for particular cases. The effect of slow and fast model axis in the calculation of isochromatic parameter is verified experimentally.

The various difficulties related to the evaluation of isoclinic parameter are presented systematically. A new approach to unwrap isoclinic parameter by using isochromatic parameter is discussed. Various methods for obtaining the isoclinic parameter in plane and circular polariscopes are implemented. A quantitative comparative study has been conducted on the performance of these methods on the isoclinic for the problem of ring under diametral compression. The study has showed in general the PST methods in plane polariscope are better compared to PST methods based on circular polariscope. Among the polarization stepped methods, the method proposed by Brown and Sullivan is found to be good. In PST methods in plane polariscope, the method proposed by Ramesh and Mangal is found to be good.

CONTENTS

Certificate....ii
Acknowledgements....iii
Abstract....iv
Contents....v
List of Figures....vi
List of Tables.... xiii

1. INTRODUCTION
1.1. Introduction....1
1.2. Present Work....2
1.3. Thesis Layout....2

2. RETARDATION CALCULATION IN DIGITAL PHOTOELASTICITY....4
2.1. Introduction....4
2.2. Intensity of Light Transmitted for a Generic Arrangement of a Circular Polariscope 4
2.3.Six-step Phase Shifting Algorithm....6
2.4.Advantages and Limitations of Six-step Phase Shifting Algorithm....7
2.5 New Approaches for Plotting the Phase map....10
2.5.1 Quadrant Approach....13
2.5.1.1Using the Circularity of Tan Function 13
2.5.1.2 Using the Absolute Value of Intensity Difference 16
2.5.2 Using Only Positive Value of Twotheta....18
2.6 Effect of Swapping Images on Phase map.... 20
2.7 Obtaining Phase map by Logical NOT.... 24
2.8 Closure 26

3. ISOCLINIC PARAMETER CALCULATION IN DIGITAL PHOTOELASTICITY

3.1. Introduction..... 27

3.2. Study of Intensity Pattern Over the Domain..... 28

3.2.1 Study of Intensity Variation in Theoretical Images.28

3.2.2 Study of Intensity Pattern in Experimental Images. 35

3.3. Evaluation of Isoclinic Parameter by Using Retardation Parameter 42

3.4. Evaluation of Isoclinic Parameter in Circular Polariscope 46

3.4.1 Algorithm by Patterson and Wang..... 46

3.4.2 Algorithm by Ajovalasit et al..... 47

3.5 Intensity of Light Transmitted for a Generic Arrangement of a Plane Polariscope..... 51

3.6 Phase Shifting Techniques Based on Plane Polariscope..... 52

3.6.1 Algorithm by Ramesh and Mangal..... 52

3.6.2 Algorithm by Brown and Sullivan 55

3.6.3 Algorithm by Chen and Lin..... 57

3.6.4 Algorithm by Dupre et al..... 63

3.6.5 Algorithm by Sarma et al..... 64

3.6.6 Algorithm by Kihara..... 66

3.6.7 Comparison of Results Obtained by Circular and Plane Polariscope Algorithms..... 68

3.7 Closure.....77

4. CONCLUSION AND SUGGESTION FOR FUTURE WORK

4.1. Conclusion.....78

4.2. Suggestion for Future Work 79

References 80

LIST OF FIGURES

2.1. Generic arrangement of a circular polariscope to employ phase shifting methodology 5

2.2. Sequence of six images recorded of a disk under diametral compression (dia 60.10 mm, thickness 6.28 mm and load 773.0 N) for the optical position listed in Table 2.1 8

2.3. Whole field representation of fractional retardation, δ_c in the form of phase map of a disk under diametral compression obtained using Eq.(2.7) with θ_c being calculated by various means: **a** θ_c by Eq. (2.4) and δ_c by Eq. (2.7) **b** θ_c by theory corresponding to the σ_1 direction and δ_c by Eq. (2.7) **c** phase map Fig. 2.3a improved by interactive approach **d** θ_c by Eq. (2.4) then unwrapped by Eqs. (2.8) & (2.9) according to quadrant and δ_c by Eq. (2.7) 9

2.4. Sequence of six images generated theoretically for a disk under diametral compression (dia 60.10 mm, thickness 6.28 mm and load 773.0 N) for the optical position listed in Table 2.1 11

2.5. Sequence of six images generated theoretically for a ring under diametral compression (dia 80 mm, thickness 5.05 mm and load 503.0 N) for the optical position listed in Table 2.1 12

2.6. Relative positions of four quadrants 13

2.7. Phase maps generated by using circularity of tan function **a** for experimentally recorded images of disk under diametral compression **b** for theoretically generated images of disk under diametral compression **c** for theoretically generated images of ring under diametral compression 14

2.8. comparison of fractional fringe order variation for method of using circularity of tan function (method 1) **a** along diametral line **b** along $r/2$ line **c** along $3r/4$ line 15

2.9. Phase maps generated by using absolute of intensity difference **a** for experimentally recorded images of disk under diametral compression **b** for theoretically generated images of disk under diametral compression

	c for theoretically generated images of ring under diametral compression	16
2.10.	Comparison of fractional fringe order variation for method of using absolute value of intensity difference (method 2) **a** along diametral line **b** along *r*/2 line **c** along 3*r*/**4** line	17
2.11.	Phase maps generated by using positive value of twotheta **a** for experimentally recorded images of disk under diametral compression **b** for theoretically generated images of disk under diametral compression **c** for theoretically generated images of ring under diametral compression	18
2.12.	Comparison of fractional fringe order variation for method of using positive value of twotheta (method 3) **a** along diametral line **b** along *r*/2 line **c** along 3*r*/**4** line	19
2.13.	**a** load at vertical diameter **b** load at horizontal diameter	21
2.14. a	sequence of six images recorded experimentally for a stress-frozen disk with loading direction kept vertically	22
2.14. b	sequence of six images recorded experimentally for a stress-frozen disk with loading direction kept horizontally	23
2.15.	Phase maps obtained for the experimentally recorded images of stress-frozen disk **a** For vertical loading direction **b** for horizontal loading direction. **c** swapping the images (I_3 , I_5) &(I_4 , I_6) for vertical loading	24
2.16.	Phase maps obtained for theoretically generated images of disk under diametral compression. **a** without swapping the images **b** by swapping the images (I_3 , I_5) &(I_4 , I_6) **c** phase map corrected by taking the not of pixel value in fig 2.16 a	25
2.17.	Phase maps for experimentally recorded images of disk shown in Fig 2.2 **a** phase map as per the image sequence given in Table 2.1 **b** improved phase map by taking NOT of pixel value	26
3.1.	Theoretical intensity plot for line at y/R = 0.0 **a** for I_1, I_2 **b** for I_3, I_5 **c** for I_4, I_6	29
3.2.	Theoretical intensity plot for line at y/R = 0.0 **a** for (I_1–I_2) **b** for (I_5–I_3) **c** for (I_4–I_6)	30
3.3.	Theoretical intensity plot for line at y/R = 0.0 **a** for Ia, I_b **b** for (I_5–I_3)/ Ia **c** for (I_4–I_6)/ Ia	31

3.4. Theoretical intensity plot for line at y/R = 0.75 **a** for I_1, I_2 **b** for I_3, I_5 **c** for I_4, I_6 32

3.5. Theoretical intensity plot for line at y/R = 0.75 **a** for (I_1–I_2) **b** for (I_5–I_3) **c** for (I_4–I_6) 33

3.6. Theoretical intensity plot for line at y/R = 0.75 **a** for Ia, I_b **b** for (I_5–I_3)/ Ia **c** for (I_4–I_6)/ Ia 34

3.7. Experimental intensity plot for line at y/R = 0.0 **a** for I_1, I_2 **b** for I_3, I_5 **c** for I_4, I_6 36

3.8. Experimental intensity plot for line at y/R = 0.0 **a** for (I_1–I_2) **b** for (I_5–I_3) **c** for (I_4–I_6) 37

3.9. Experimental intensity plot for line at y/R = 0.0 **a** for Ia, I_b **b** for (I_5–I_3)/ Ia **c** for (I_4–I_6)/ Ia 38

3.10. Experimental intensity plot for line at y/R = 0.75 **a** for I_1, I_2 **b** for I_3, I_5 **c** for I_4, I_6 39

3.11. Experimental intensity plot for line at y/R = 0.75 **a** for (I_1–I_2) **b** for (I_5–I_3) **c** for (I_4–I_6) 40

3.12. Experimental intensity plot for line at y/R = 0.75 **a** for Ia, I_b **b** for (I_5–I_3)/ Ia **c** for (I_4–I_6)/ Ia 41

3.13. Sequence of six images generated theoretically as per the sequence in Table 2.1for the disk under diametral compression (load 773 N, dia. 60 mm, thickness 6.28 mm, F_σ = 11.9973 N/mm/fringe) 44

3.14. Phase map obtained by quadrant approach for the theoretically generated images given in Fig. 3.13 45

3.15 Isoclinic plots for the theoretically generated images of disk under diametral compression **a** by method of Patterson & Wang (Eq. 3.13) **b** by new approach (Eq. 3.12) 45

3.16 Plot of theoretical theta by Patterson & Wang, theoretical theta by modified expression, theta by theory. 46

3.17 Sequence of six images recorded experimentally for the method by Patterson & Wang, as per the sequence given in Table 3.1 for the ring under diametral compression (load 503 N, dia. 80 mm, thickness 5.05 mm, F_σ = 11.2329 N/mm/fringe) 48

3.18 Sequence of six images recorded experimentally for the method by

Ajovalasit et al. as per the sequence given in Table 3.2 for the ring under diametral compression (load 503 N, dia. 80 mm, thickness 5.05 mm, F_σ = 11.2329 N/mm/fringe) 49

3.19 Isoclinic plots for the experimentally recorded images of ring under diametral compression **a** by the method of Patterson & Wang **b** by the method of Ajovalasit et al. 50

3.20 Isoclinic plots for the experimentally recorded images of disk under diametral compression for a low load (load 84 N, Dia. 60 mm, thickness 5.05 mm, F_σ= 11.2329 N/mm/fringe) **a** by the method of Patterson & Wang **b** by the method of Ajovalasit et al. 50

3.21 Generic arrangement of a plane polariscope to employ phase shifting methodology 51

3.22 Sequence of six images recorded experimentally for the method by Ramesh & Mangal, as per the sequence given in Table 3.3 for the ring under diametral compression (load 503 N, Dia. 80 mm, thickness 5.05 mm, F_σ = 11.2329 N/mm/fringe) 54

3.23 Sequence of four images recorded experimentally for the method by Brown & Sullivan, as per the sequence given in Table 3.4 for the ring under diametral compression (load 503 N, Dia. 80 mm, thickness 5.05 mm, F_σ = 11.2329 N/mm/fringe) 56

3.24 Six images recorded experimentally for the method by Chen & Lin, as per the sequence given in Table 3.5 for the ring under diametral compression (load 503 N, Dia. 80 mm, thickness 5.05 mm, F_σ = 11.2329 N/mm/fringe) 58

3.25 Normalized dark field images generated by Eq. (3.20) using theoretically generated images as per the sequence given in Table 3.5. **a** for 0 deg. **b** for 22.5 deg **c** for 45 deg 60

3.26. Normalized dark field images generated without adjustment by Eq. (3.20) using experimentally recorded images as per the sequence given in Table 3.5. **a** for 0 deg. **b** for 22.5 deg **c** for 45 deg 61

3.27 Normalized dark field images generated with adjustment (Eq.3.20, k = 0.60) using experimentally recorded images as per the sequence given in Table 3.5. **a** for 0 deg. **b** for 22.5 deg **c** for 45 deg 62

3.28 Sequence of Four images recorded experimentally for the method by

Dupre et al. as given in Table 3.6 for the ring under diametral compression (load 503 N, dia. 80 mm, thickness 5.05 mm, F_σ = 11.2329 N/mm/fringe) 64

3.29 Sequence of Four images recorded experimentally for the method by Sarma et al. as given in Table 3.6 for the ring under diametral compression (load 503 N, dia. 80 mm, thickness 5.05 mm, F_σ = 11.2329 N/mm/fringe) 65

3.30 Sequence of first six images recorded experimentally for the method by Kihara, as given in Table 3.8 for the ring under diametral compression (load 503 N, dia. 80 mm, thickness 5.05 mm, F_σ = 11.2329 N/mm/fringe) 67

3.30 Sequence of last two images recorded experimentally for the method by Kihara, as given in Table 3.8 for the ring under diametral compression (load 503 N, dia. 80 mm, thickness 5.05 mm, F_σ = 11.2329 N/mm/fringe) 68

3.31 Isoclinic plots obtained for the theoretically generated images of ring under diametral compression. **a** by Patterson & Wang **b** by Ajovalasit et al. **c** by Ramesh & Mangal **d** by Brown & Sullivan **e** by Chen & Lin **f** by Dupre et al. 69

3.32 Isoclinic plots obtained for the theoretically generated images of ring under diametral compression. **a** by Sarma et al. **b** by Kihara 70

3.33 Isoclinic plots obtained for the experimentally recorded images of ring under diametral compression. **a** by Patterson & Wang **b** by Ajovalasit et al. **c** by Ramesh & Mangal **d** by Brown & Sullivan **e** by Chen & Lin (without adjustment) **f** by Chen & Lin (with adjustment) 71

3.34 Isoclinic plots obtained for the experimentally recorded images of ring under diametral compression. **a** by Dupre et al. **b** by Sarma et al. **c** by Kihara 72

3.35 Comparison of experimenatal theta with theoretical theta for line at *y/R* =0.50 **a** Ramesh & Mangal, Patterson & Wang, Ajovalasit et. al., & theory **b** Brown & Sullivan, Dupre et. al., Kihara, theory. 73

3.35 **c** Comparison of Experimenatal theta with theoretical theta for line at *y/R* =0.50 for Chen & Lin, Sarma et. al. Theory 74

3.36 Comparison of experimenatal theta with theoretical theta for line at y/R =0.25 **a** Ramesh & Mangal, Patterson & Wang, Ajovalasit et. al., & theory **b** Brown & Sullivan, Dupre et. al., Kihara, & theory. 75

3.36 **c** Comparison of Experimenatal theta with theoretical theta for line at y/R =0.50 for Chen & Lin, Sarma et. al. & Theory 76

LIST OF TABLES

2.1. Polariscope arrangement and intensity equations for six-step phase shifting method 6

2.2. Polariscope arrangement and intensity equations for six-step phase shifting method with reference to θ at fast axis 20

3.1. Optical arrangement for Patterson and Wang 46

3.2. Optical arrangement for Ajovalasit et al. 47

3.3. Table showing the intensity equations for different orientation of the polarizer and analyzer 53

3.4 Polariscope arrangements and intensity equations for polarization steppimg schemes for Brown & Sullivan 55

3.5 Polariscope arrangements and intensity equations for polarization steppimg schemes for Chen & Lin 57

3.6 Optical arrangement for Dupre et al. 63

3.7 Optical arrangement for Sarma et al. 64

3.8 Optical arrangement for Kihara. 66

CHAPTER 1

INTRODUCTION

1.1 Introduction

Photoelasticity deals with the determination of stress fields by use the of the polarized light. This method is based on the temporary birefringence effect. Certain transparent, non-crystalline materials like Plexiglass, celluloid, homolite, epoxy etc., are optically isotropic when not loaded but become optically anisotropic and display characteristics similar to crystals when they are stressed. The birefringence in the material is retained only during the application of the loads and disappears when they are removed. Measurements of this birefringence provide data adequate for quantitative determination of the corresponding state of stress. The measurements are made with the help of an optical instrument called polariscope. A polariscope could be used to find out viz. the maximum shear stress i.e., the difference in the principle stresses and the orientation of principle stresses. The corresponding contours called isochromatic and isoclinic fringes. The experimentation in photoelasticity involves acquisition of these images and their interpretation. The main merit of photoelasticity is its simplicity in experimentation as well as in the evaluation of the stress field.

Photoelasticity directly provides the information of principal stress difference and the orientation of the principal stress direction at the point of interest. Using these, one can find the normal stress difference and in-plane shear stress by invoking equations in mechanics of solids or Mohr's circle.

1.2 Present Work

In photoelasticity, the phase information is affected by both the difference in principal stresses and the orientation of the principle stress direction. This is referred to as isochromatic-isoclinic interaction and this affects the evaluation of isochromatics and isoclinics differently. Hence in digital photoelasticity the whole field evaluation of isoclinic parameter poses certain problems. Use of six-step phase shifting technique, which uses the intensity data in spatial domain, in general provides the estimation of fringe order with a reasonable accuracy. However, the isoclinic parameter is not quite accurate.

Due to isoclinic-isochromatic interaction on isochromatics, the phase map has ambiguity in the sign of fractional retardation in some zones. The present work discusses different methods of improving the phase map at least for particular cases. A new approach to process image in quadrants is presented here. An effective use of taking logical NOT of a pixel value for the improvement of phase map is presented. The effect of slow and fast model axis in the calculation of isochromatic parameter is verified experimentally.

The intensity patterns obtained from six-step phase shifting method are studied for the problem of disk under diametral compression. The various difficulties related to the evaluation of isoclinic parameter are presented systematically. A new approach to unwrap isoclinic parameter by using isochromatic parameter is discussed. Various methods for obtaining the isoclinic parameter in plane and circular polariscopes are implemented. A quantitative comparative study has been conducted on the performance of these methods on the isoclinic for the problem of ring under diametral compression.

1.3 Thesis Layout

In chapter 2, first six-step phase shifting method is discussed in detail. After that new approaches based on processing the images in quadrants to overcome the limitations in six-step phase shifting method has been discussed. Chapter 2 also discusses in details on, how the orientation of model slow and fast axis influences the isoclinic parameter. A new approach of logical NOT to improve the phase map is also discussed.

Chapter 3 focuses on the extraction of experimental isoclinic data from various methods in plane and circular polariscopes. First a study of intensity patterns is done in six-step phase shifting technique. The study has been done to understand the reasons of numerical inaccuracies involved in the calculation of isoclinic parameters. A different way of arriving at isoclinic parameter from the isochromatic parameter is studied.

A quantitative comparative study of various phase shifting methods and polarization stepping methods for the calculation of isoclinic parameter in plane and circular polariscopes has been done for the problem of ring under diametral compression.

Chapter 4 presents the conclusion and suggestion for the future work.

CHAPTER 2

RETARDATION CALCULATION IN DIGITAL PHOTOELASTICITY

2.1 Introduction

One of the early approaches for retardation calculation over the complete model domain was the method of phase shifting. In this, intensity data recorded for a few optical arrangements are judiciously used to solve for the isochromatic and isoclinic fringe order. Following the lines of phase shifting [1], several variants of these appeared such as polarization stepping [2] and load stepping [3]. In polarization stepping the polarizer and analyzer are kept crossed for recording intensity data. Load stepping essentially adopts one of the existing phase shifting techniques for the intensity recording. Instead of recording intensity data for one load, the data is recorded for small steps of loads on either side of the load of interest. The methodologies such as phase shifting, polarization stepping or load stepping have their own advantages and inherent limitations. In this chapter, the limitations of phase shifting are initially highlighted. New approaches to overcome these limitations, based upon the processing the image in quadrants have been proposed. These approaches are validated for the problem of a disk under diametral compression.

2.2 Intensity of Light Transmitted for a Generic Arrangement of a Circular Polariscope

Consider the optical arrangement shown in Fig. 2.1 in which the second quarter-wave plate and the analyzer are kept at arbitrary positions. The first quarter-wave plate is kept at $\xi = 135$-deg.

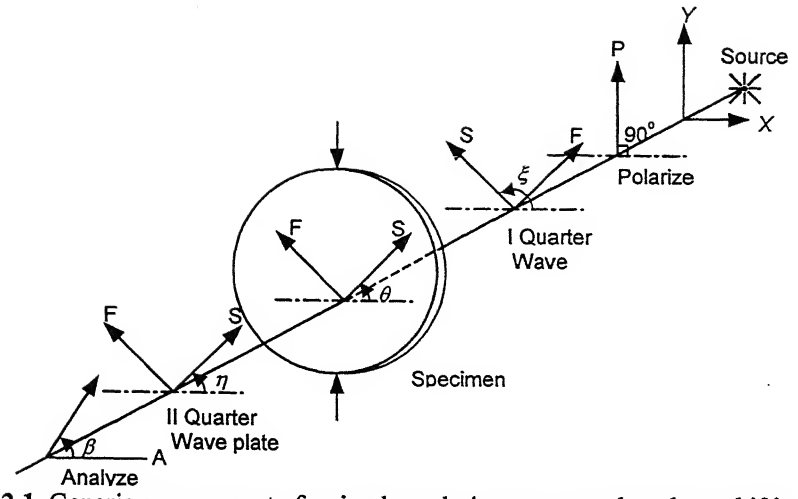

Fig. 2.1. Generic arrangement of a circular polariscope to employ phase shifting methodology

Using Jones calculus, the components of light vector along the analyzer axis and perpendicular to the analyzer axis (for $\xi = 135$-deg) are obtained as

$$\begin{Bmatrix} E_\beta \\ E_{\beta+\pi/2} \end{Bmatrix} = \frac{1}{2}\begin{bmatrix} \cos\beta & \sin\beta \\ -\sin\beta & \cos\beta \end{bmatrix}\begin{bmatrix} 1-\mathrm{i}\cos 2\eta & -\mathrm{i}\sin 2\eta \\ -\mathrm{i}\sin 2\eta & 1+\mathrm{i}\cos 2\eta \end{bmatrix} \times \begin{bmatrix} \cos\frac{\delta}{2}-\mathrm{i}\sin\frac{\delta}{2}\cos 2\theta & -\mathrm{i}\sin\frac{\delta}{2}\sin 2\theta \\ -\mathrm{i}\sin\frac{\delta}{2}\sin 2\theta & \cos\frac{\delta}{2}+\mathrm{i}\sin\frac{\delta}{2}\cos 2\theta \end{bmatrix}\begin{bmatrix} 1 & \mathrm{i} \\ \mathrm{i} & 1 \end{bmatrix}\begin{Bmatrix} 0 \\ 1 \end{Bmatrix} k e^{\mathrm{i}\omega t} \tag{2.1}$$

The combination of the quarter-wave plate at $\xi = 135$-deg and the polarizer produces a left circularly polarised light. Denoting the intensity of light transmitted as I_ℓ, the intensity expression is obtained as

$$I_\ell = \frac{I_a}{2} + \frac{I_a}{2}[\sin 2(\beta-\eta)\cos\delta - \sin 2(\theta-\eta)\cos 2(\beta-\eta)\sin\delta] \tag{2.2}$$

where I_a accounts for the amplitude of light vector and proportionality constant. The intensity equation developed show that when the extinction conditions are satisfied, the intensity of light transmitted should be zero. However, this never happens in an experiment. In order to account for this behaviour, a term I_b is added to account for the stray light/background illumination.

In subsequent discussions, the intensity of light transmitted will be denoted as I_i for the i^{th} optical arrangement. The orientation of the optical element that needs to be

rotated will also appear with a subscript *i*. Thus, in Eq. (2.2) by adding the term I_b to account for background illumination/stray light reduce to

$$I_i = I_b + \frac{I_a}{2} + \frac{I_a}{2}[\sin 2(\beta_i - \eta_i)\cos\delta - \sin 2(\theta - \eta_i)\cos 2(\beta_i - \eta_i)\sin\delta] \quad (2.3)$$

2.3 Six-step Phase Shifting Algorithm

One of the most successful and time-tested approach of phase shifting to evaluate isoclinic and isochromatic parameter involves the use of six different optical arrangements [1]. The various positions and the respective intensity equations are summarized in Table 2.1. The arrangement shown also accounts for the mismatch of quarter wave plate error.

Using the intensity equation listed in Table 2.1, the isoclinic parameter θ is obtained as

$$\theta_c = \frac{1}{2}\tan^{-1}\left(\frac{I_5 - I_3}{I_4 - I_6}\right) \quad (2.4)$$

Table 2.1. Polariscope arrangement and intensity equations for six-step phase shifting method.

ξ	η	β	Intensity equation
$3\pi/4$	$\pi/4$	$\pi/2$	$I_1 = I_b + \frac{I_a}{2}(1+\cos\delta)$
$3\pi/4$	$\pi/4$	0	$I_2 = I_b + \frac{I_a}{2}(1-\cos\delta)$
$3\pi/4$	0	0	$I_3 = I_b + \frac{I_a}{2}(1-\sin 2\theta\sin\delta)$
$3\pi/4$	$\pi/4$	$\pi/4$	$I_4 = I_b + \frac{I_a}{2}(1+\cos 2\theta\sin\delta)$
$\pi/4$	0	0	$I_5 = I_b + \frac{I_a}{2}(1+\sin 2\theta\sin\delta)$
$\pi/4$	$3\pi/4$	$\pi/4$	$I_6 = I_b + \frac{I_a}{2}(1-\cos 2\theta\sin\delta)$

From the equations shown in Table 2.1, the fractional retardation δ is obtained as

$$\delta_c = \tan^{-1}\left(\frac{(I_4 - I_6)}{(I_1 - I_2)\cos 2\theta_c}\right) = \frac{1}{2}\tan^{-1}\left(\frac{I_a \cos 2\theta_c \sin \delta_c}{I_a \cos 2\theta_c \cos \delta_c}\right) \quad (2.5)$$

$$\delta_c = \tan^{-1}\left(\frac{(I_5 - I_3)}{(I_1 - I_2)\sin 2\theta_c}\right) = \frac{1}{2}\tan^{-1}\left(\frac{I_a \sin 2\theta_c \sin \delta_c}{I_a \sin 2\theta_c \cos \delta_c}\right) \quad (2.6)$$

In Eqs. (2.4) to (2.6) the subscript c for the θ or δ indicates that the principal values of the inverse trigonometric function is referred. In subsequent discussion too the same symbolism will be used

2.4 Advantages and Limitations of the Six-step Phase Shifting Method

The exact calculation of isoclinic angle and fractional retardation is not trivial from Eqs. (2.4) – (2.6). Equation (2.4) shows that the isoclinic value is indeterminate at those points where $\delta_c = 0, \pi, 2\pi, 3\pi \ldots$. The implication is that the isoclinic contour will not be continuous over the domain. When δ_c is not exactly equal to 0 or π or 2π etc. but very close to these values, θ_c does not become indeterminate but the value of θ_c determined will be unreliable and appears as noise in isoclinic fringe when plotted. This is known as isochromatic-isoclinic interaction in the calculation of the isoclinic parameter.

Considering that θ_c is calculated correctly by Eq. (2.4), the calculation of δ_c by Eqs. (2.5) or (2.6) should result in the same value of δ_c if continuous variables are used in the arctangent calculations. In practical applications, this is not the case due to intensity digitisation and quantization and only discrete values are used in the arctangent calculations. This can lead to error in the calculations. Further, in Eqs. (2.5) & (2.6), δ_c has low-modulation regions when $\cos 2\theta_c$ or $\sin 2\theta_c$ are small. In these regions, the intensity differences $(I_4 - I_6)$ or $(I_5 - I_3)$ will also be small. The evaluation of δ_c will involve the ratio of two small discrete numbers and will be in considerable error in such regions. This is termed as isoclinic-isochromatic interaction in the calculation of the fractional retardation. Apart from this, the principal value of θ_c evaluated by Eq. (2.4) lies in the range $-\pi/4$ to $\pi/4$ and an ambiguity exists on whether θ_c corresponds to σ_1 or σ_2 direction over the domain [1].

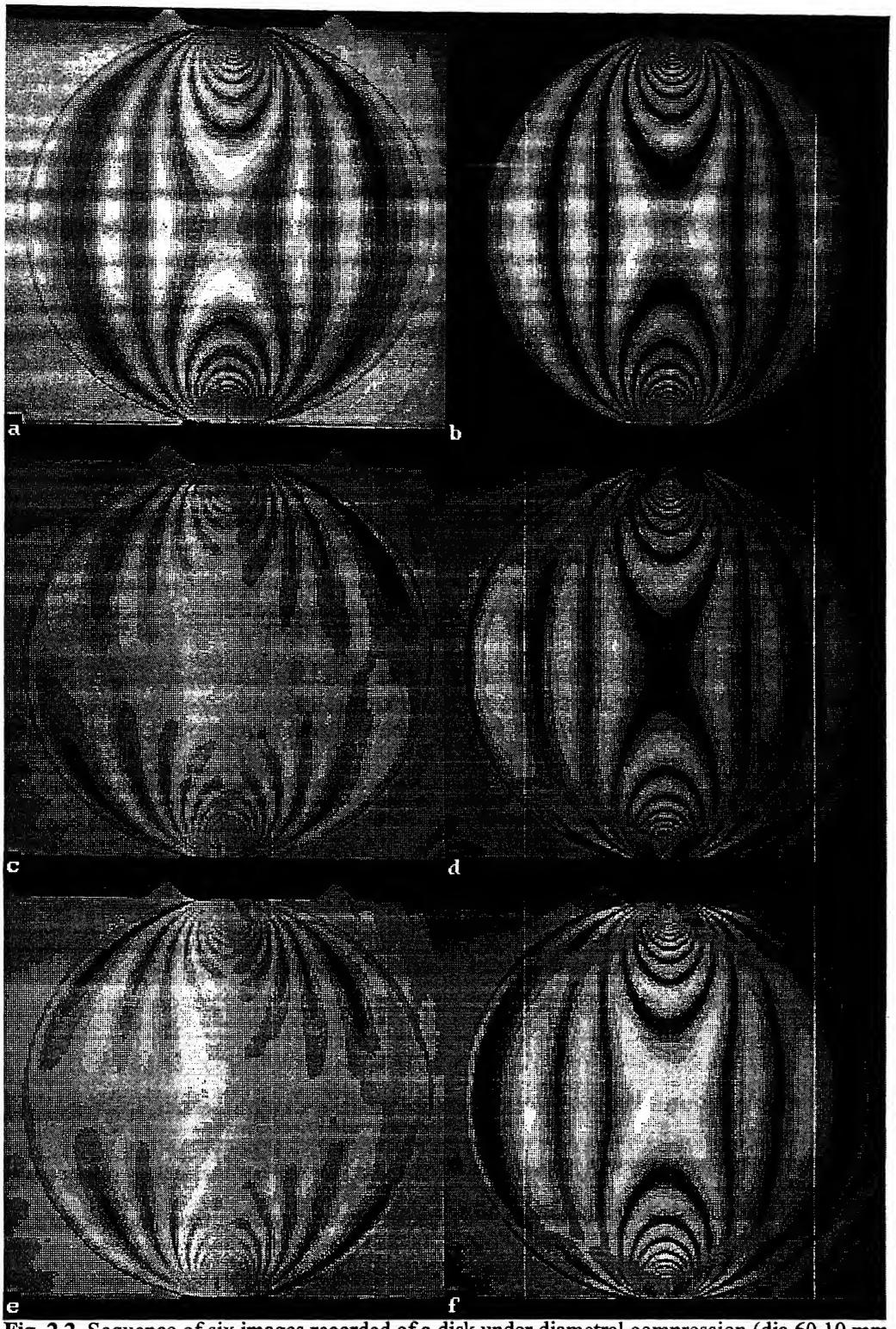

Fig. 2.2. Sequence of six images recorded of a disk under diametral compression (dia 60.10 mm, thickness 6.28 mm and load 773.0 N) for the optical position listed in Table 2.1

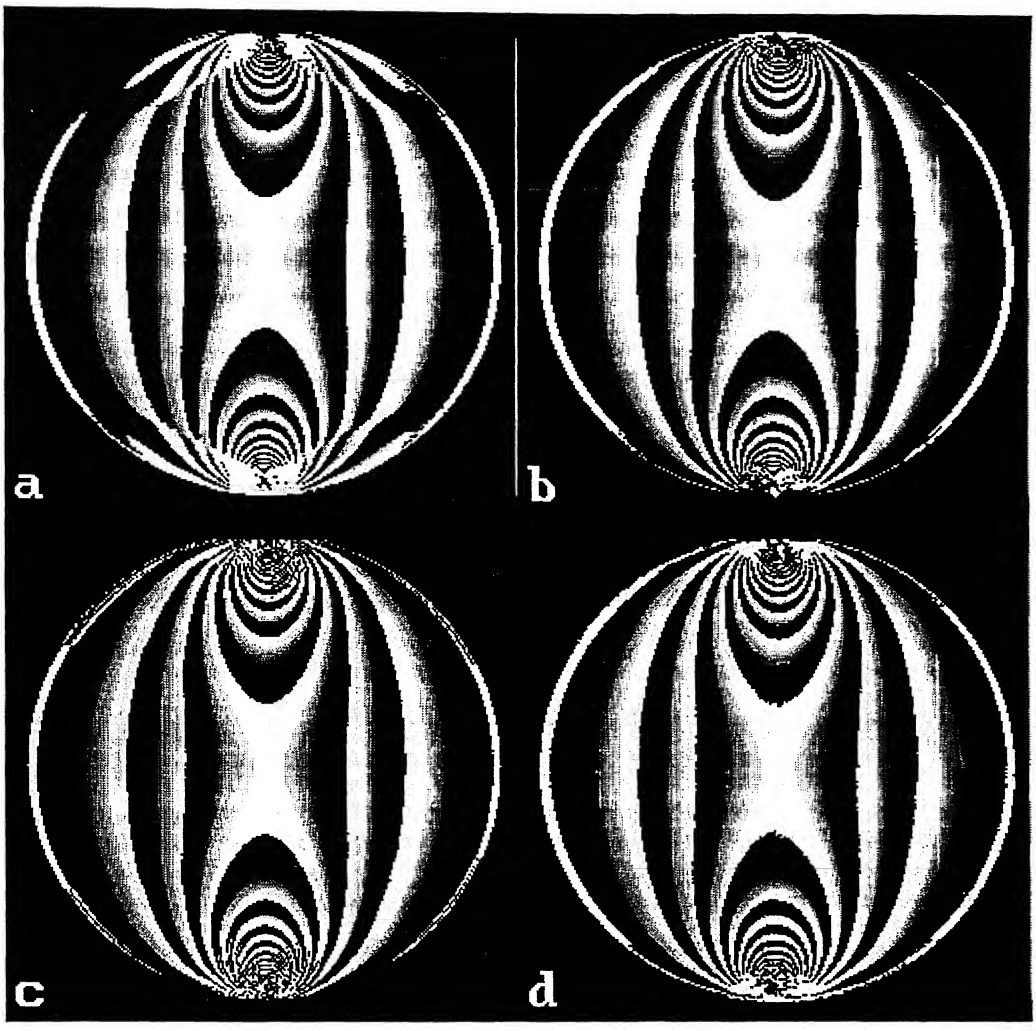

Fig. 2.3. Whole field representation of fractional retardation, δ_c in the form of phase map of a disk under diametral compression obtained using Eq.(2.7) with θ_c being calculated by various means: **a** θ_c by Eq. (2.4) and δ_c by Eq. (2.7) **b** θ_c by theory corresponding to the σ_1 direction and δ_c by Eq. (2.7) **c** phase map Fig. 2.3a improved by interactive approach **d** θ_c by Eq. (2.4) then unwrapped by Eqs. (2.8) & (2.9) according to quadrant and δ_c by Eq. (2.7)

It is instructive to note that regions of low values of $\cos 2\theta_c$ coincide with high values of $\sin 2\theta_c$ and vice versa. Therefore for every point in the region of interest one has two estimates of δ_c with different degrees of error depending on the region. Thus, the results must be combined appropriately to get the best possible values of δ_c. For the whole domain it is obtained as [4]

$$\delta_c = \tan^{-1}\left(\frac{(I_5 - I_3)\sin 2\theta_c + (I_4 - I_6)\cos 2\theta_c}{(I_1 - I_2)}\right) = \tan^{-1}\left(\frac{I_a \sin \delta_c}{I_a \cos \delta_c}\right) \qquad (2.7)$$

Unlike Eqs. (2.5) or (2.6), Eq. (2.7) always guarantees a high modulation over the field.

Figure 2.2 shows the sequence of six images recorded for a disk under diametral compression (dia 60.10 mm, thickness 6.28 mm and load 773.0 N). The material stress fringe value is calculated by a digital technique and is found to be 11.9973 N/mm/fr. Figure 2.3a shows the phase map obtained by Eq. (2.7). on scrutiny one can see that near the load application points the phase map is not good. This is not just due to high stress gradient but is due to the interaction of isoclinic on the isochromatic evaluation. The principal values of θ_c of Eq. (2.4) lies in the region $-\pi/4 \leq \theta_c \leq \pi/4$ whereas, physically, principal stress direction lies in the range $-\pi/2 \leq \theta \leq \pi/2$ and this introduces an ambiguity on δ evaluation. Figure 2.3b shows the phase map obtained from experimental images using the theoretically calculated θ indicating the σ_1 direction throughout the domain. The phase map is uniformly good over the domain.

Though, phase shifting can provide δ over the whole domain, certain level of human interaction is needed to correctly identify its sign for unwrapping. This is one of the serious limitation of the technique and could be resolved only when isoclinic is unwrapped correctly over the domain corresponding to either σ_1 or σ_2 direction uniformly over the domain [1,5]. This problem is a current area of research and automatic solution is still elusive. Figure 2.3c shows the phase map of 2.3a improved by the interactive approach developed by Ramesh and Mangal [1]. The approach is a general one and is applicable for any problem and one requires the information of fringe gradient in the bad zone for the phase map improvement.

The basic advantage of phase shifting is that inverse tangent functions are used for δ calculation. The unwrapping of δ becomes a lot more simpler and straight forward.

2.5 New Approaches for Plotting the Phase Map

The phase maps are influenced by the value of isoclinic parameter, particularly by it's sign. The idea is to study the effect of various methods of evaluation of the isoclinic parameter value on the resultant phase map. Different ways of obtaining the isoclinics such as, based upon the circularity of trigonometric functions, use of absolute value of intensity difference, use of only positive values of twotheta are discussed here. The purpose is to explore various possibilities in plotting the phase map, which may work satisfactorily at least for particular cases. Even when the method works on the theoretically generated images, it may have problems while processing experimentally recorded images.

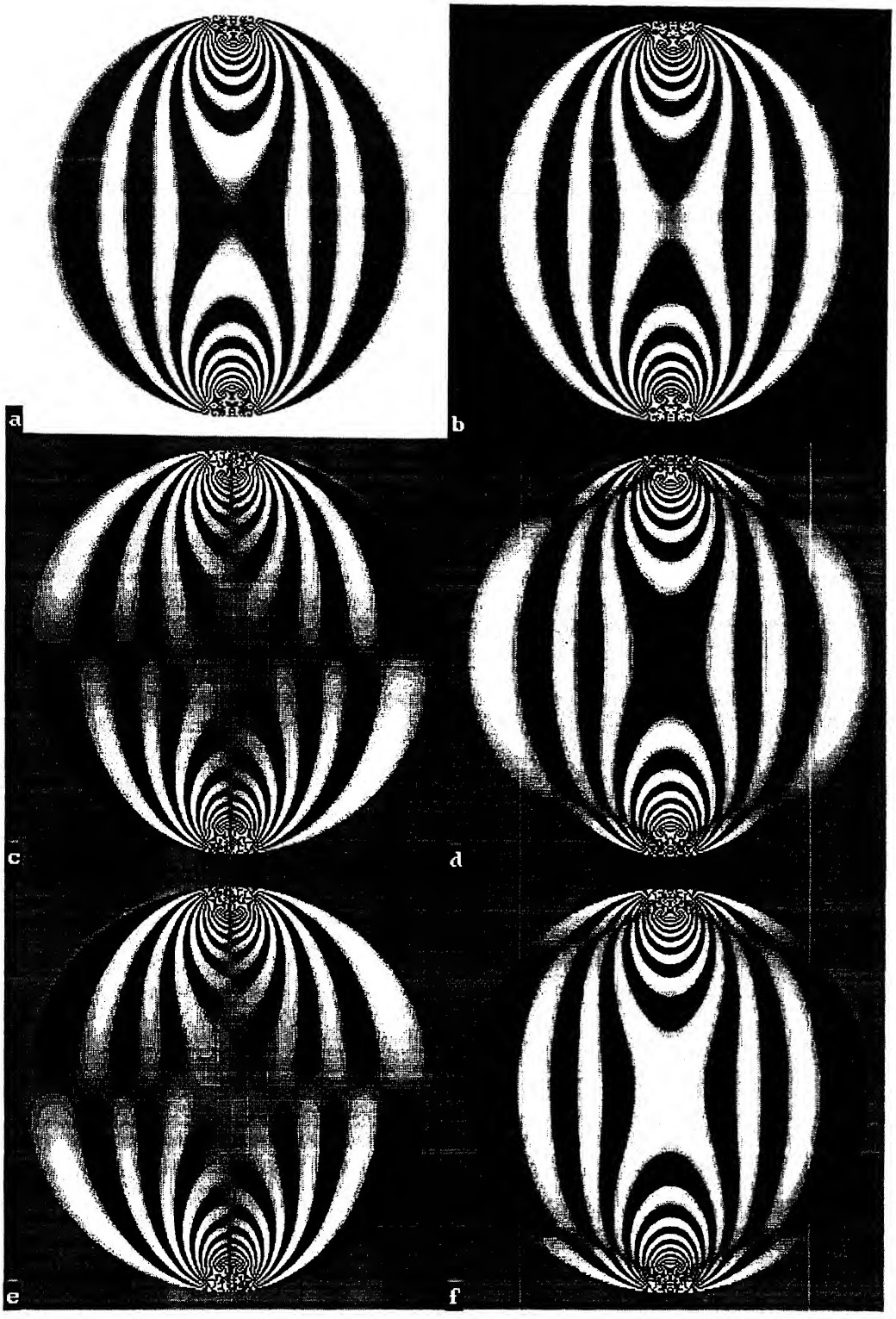

Fig. 2.4. Sequence of six images generated theoretically for a disk under diametral compression (dia 60.10 mm, thickness 6.28 mm and load 773.0 N) for the optical position listed in Table 2.1

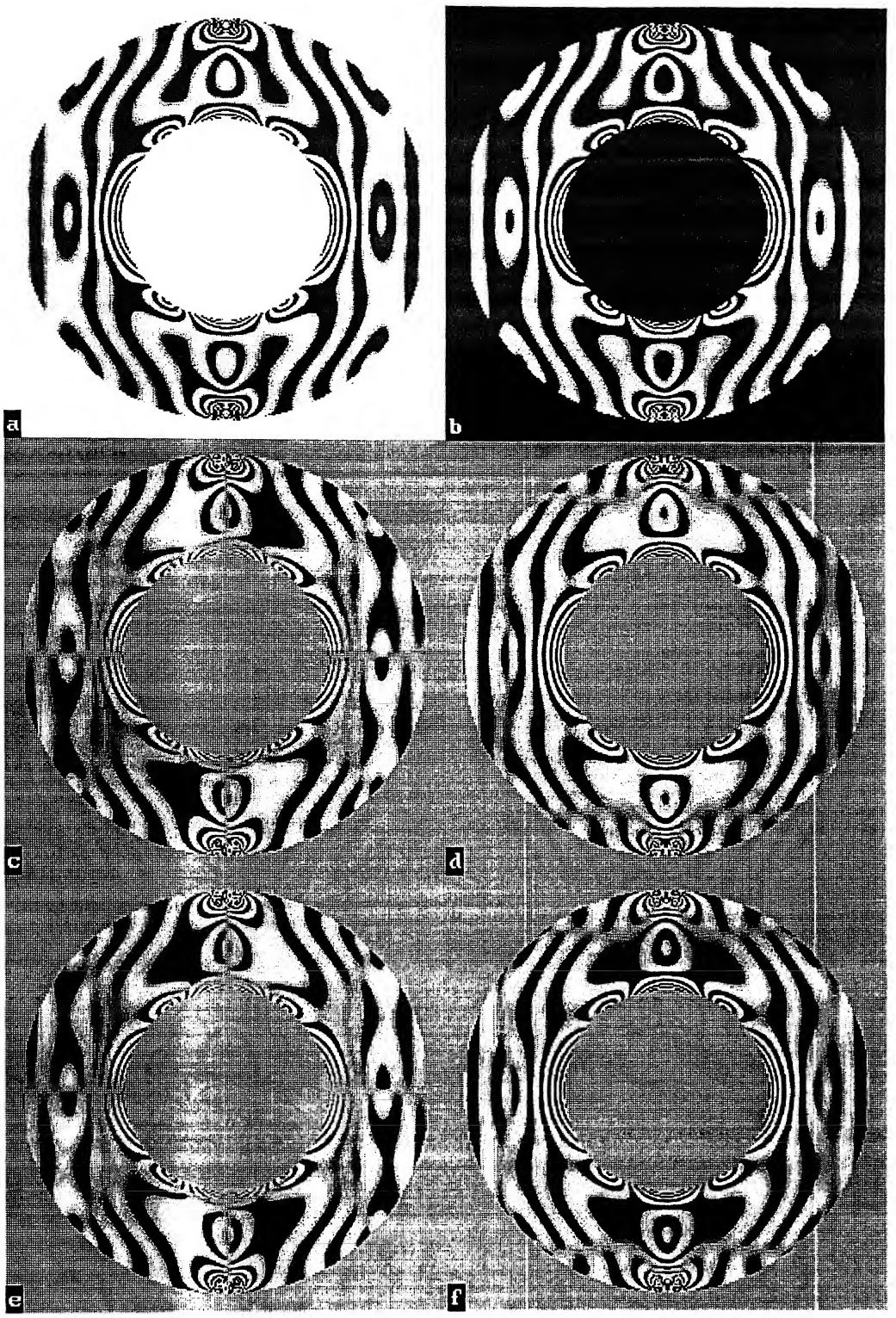

Fig. 2.5. Sequence of six images generated theoretically for a ring under diametral compression (dia 80 mm, thickness 5.05 mm and load 503.0 N) for the optical position listed in Table 2.1

The example problem chosen are disk under diametral compression (both theoretical and experimental) and ring under diametral compression (theoretical). Figure 2.4 shows the theoretically generated image for disk under diametral compression and Figure 2.5 shows for the ring under diametral compression

2.5.1 Quadrant Approach

In this the phase map is plotted by dividing the image into four quadrants All these approaches are based upon Eq. (2.7).

2.5.1.1 Using the circularity of tan function

In this method the image is divided into four quadrants as shown in Fig. 2.6.

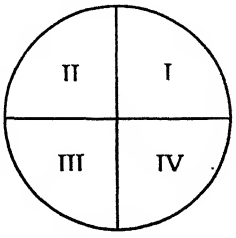

Fig. 2.6. Relative positions of four quadrants

In the first and third quadrant after calculating the theta, the following conditions are applied.

$$\theta = \begin{cases} \theta_c & \text{if}(\theta \geq 0) \\ \theta_c + \pi/2 & \text{if}(\theta < 0) \end{cases} \tag{2.8}$$

In the second and fourth quadrant the condition applied is

$$\theta = \begin{cases} \theta_c & \text{if}(\theta \leq 0) \\ \theta_c - \pi/2 & \text{if}(\theta > 0) \end{cases} \tag{2.9}$$

Changing the value of theta by $\pi/2$ will change the values of $\sin 2\theta$, $\cos 2\theta$ from positive to negative. Figure 2.7a shows the phase map obtained by employing the above approach for the disk under diametral compression recorded experimentally as in Fig. 2.2. Figure 2.7b shows the phase map calculated based on theoretically generated images as in Fig. 2.4. The phase map is good for the theoretically generated images. For the experimentally recorded images the phase map is not good at points very close to

the vertical and horizontal diameter. This is because of non-symmetric intensity patterns. Also the loading direction is not perfectly vertical in the experiment. The fractional fringe order for the experimentally recorded images of disk are shown in the Fig. 2.8. For the problem of ring under diametral compression, the phase map obtained by using theoretically generated images is shown in Fig. 2.7c. This shows that though the method works for the disk under diametral compression, it fails for the problem of ring under diametral compression.

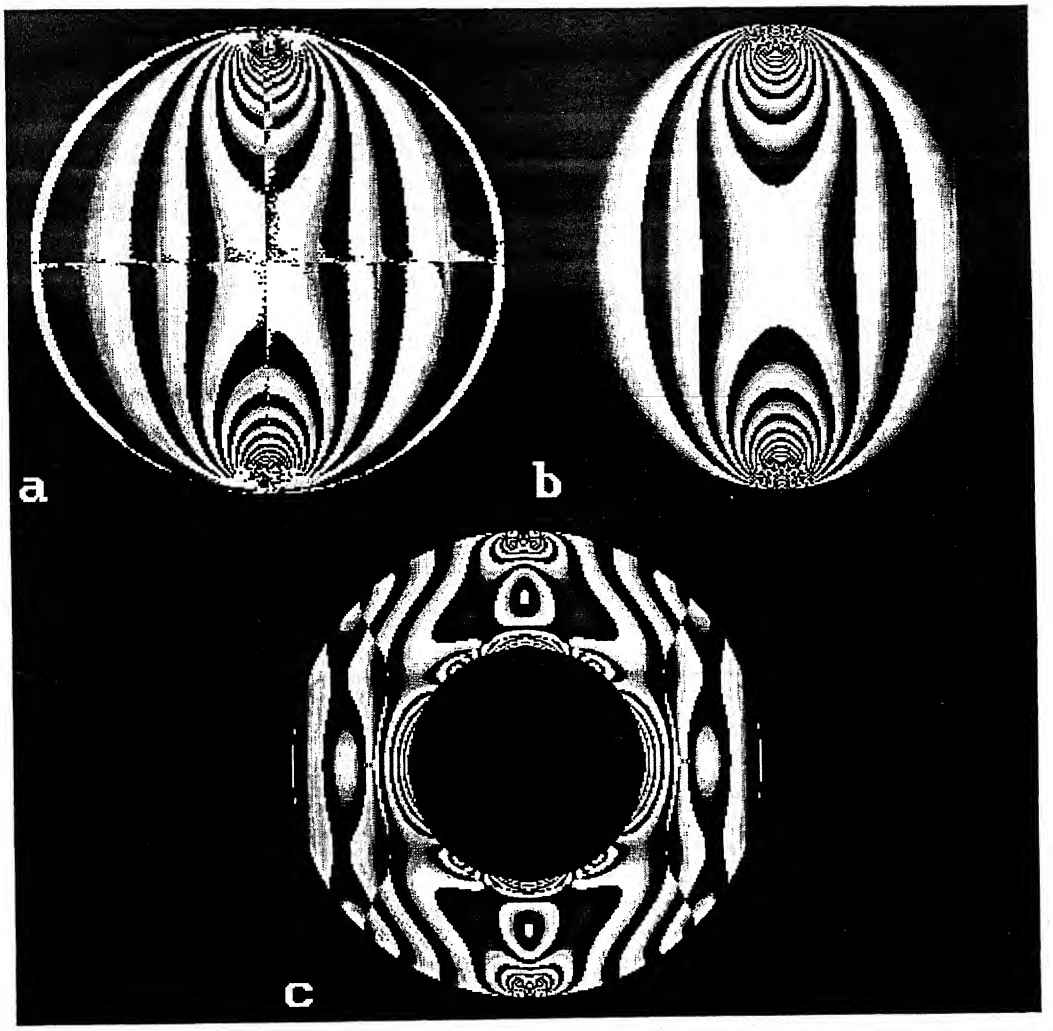

Fig 2.7 Phase maps generated by using circularity of tan function **a** for experimentally recorded images of disk under diametral compression **b** for theoretically generated images of disk under diametral compression **c** for theoretically generated images of ring under diametral compression

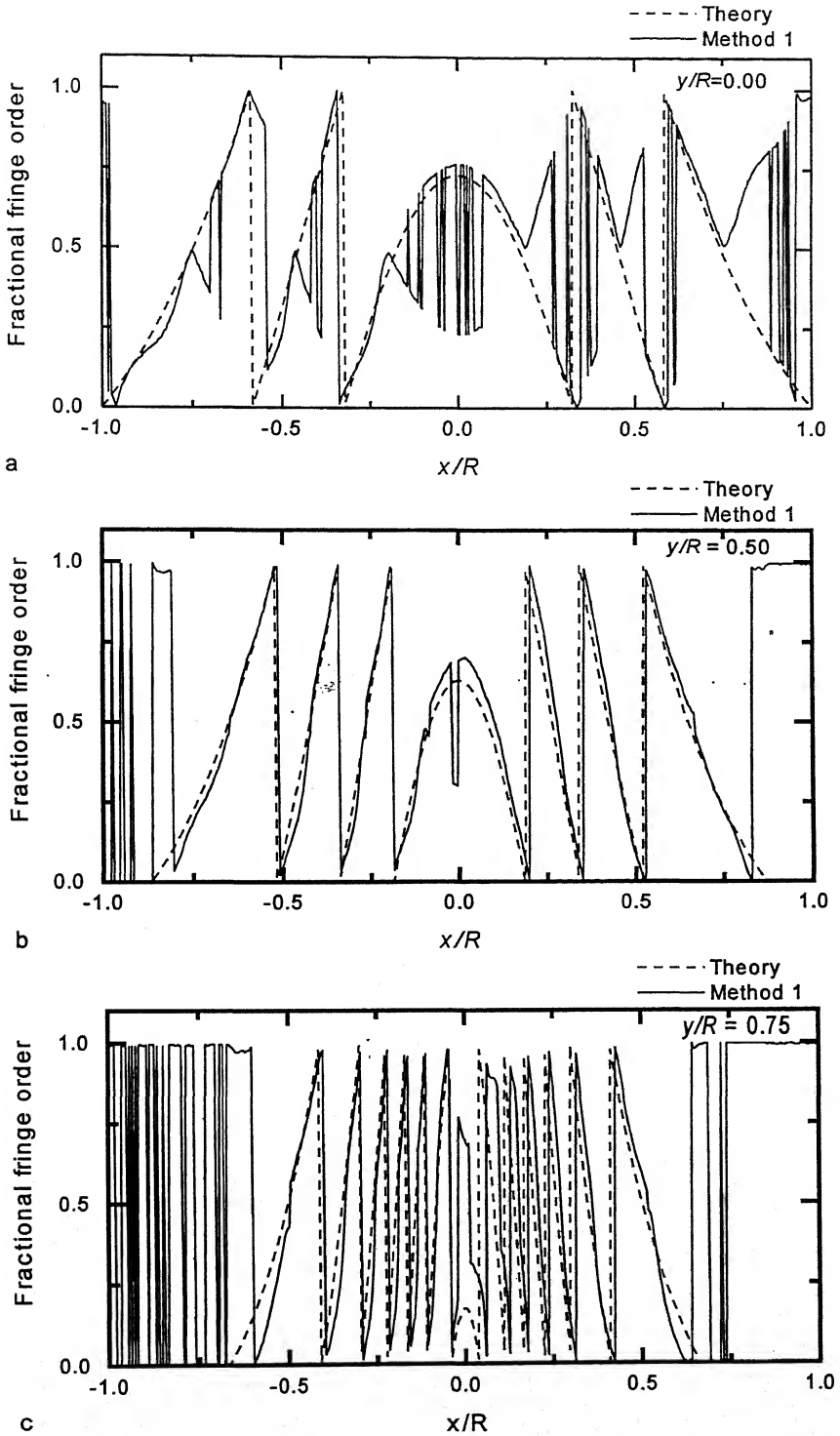

Fig. 2.8. comparison of fractional fringe order variation for method of using circularity of tan function (method 1) **a** along diametral line **b** along $r/2$ line **c** along $3r/4$ line

2.5.1.2 Using the absolute values of intensity difference.

In this method, the absolute values of $(I_4 - I_6)$ and $(I_5 - I_3)$ are used in Eq. (2.4) to calculate θ. Since both the values involved are positive, the resulting value of θ will be positive only. This positive value of theta is plotted in the first quadrant. In the second quadrant same value with negative sign (i.e. with $-\theta$) is plotted. The results for the disk under diametral compression for the experimentally recorded images is shown in Fig. 2.9a and for the theoretically generated images in Fig 2.9b. In this case, there are some noise points in the theoretically calculated phase map. Also areas which are very close to the loading point are bad for both experimental and theoretical images. The fractional fringe order for the theoretical and experimental images of disk are shown in Fig. 2.10. For the ring under diametral compression, the theoretical image is shown in Fig. 2.9c This shows that though the method works for the disk under diametral compression, it fails for the problem of ring under diametral compression.

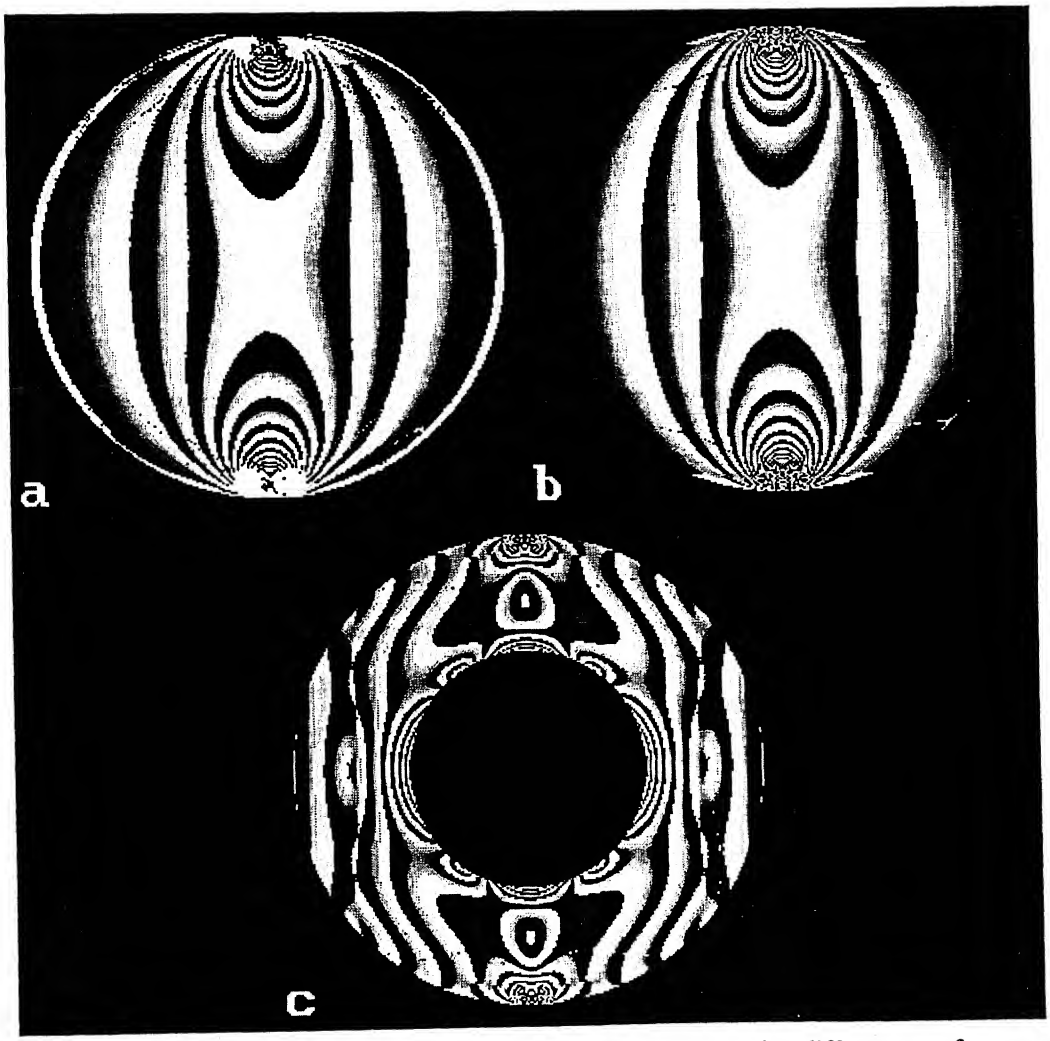

Fig 2.9 Phase maps generated by using absolute value of intensity difference **a** for experimentally recorded images of disk under diametral compression **b** for theoretically generated images of disk under diametral compression **c** for theoretically generated images of ring under diametral compression

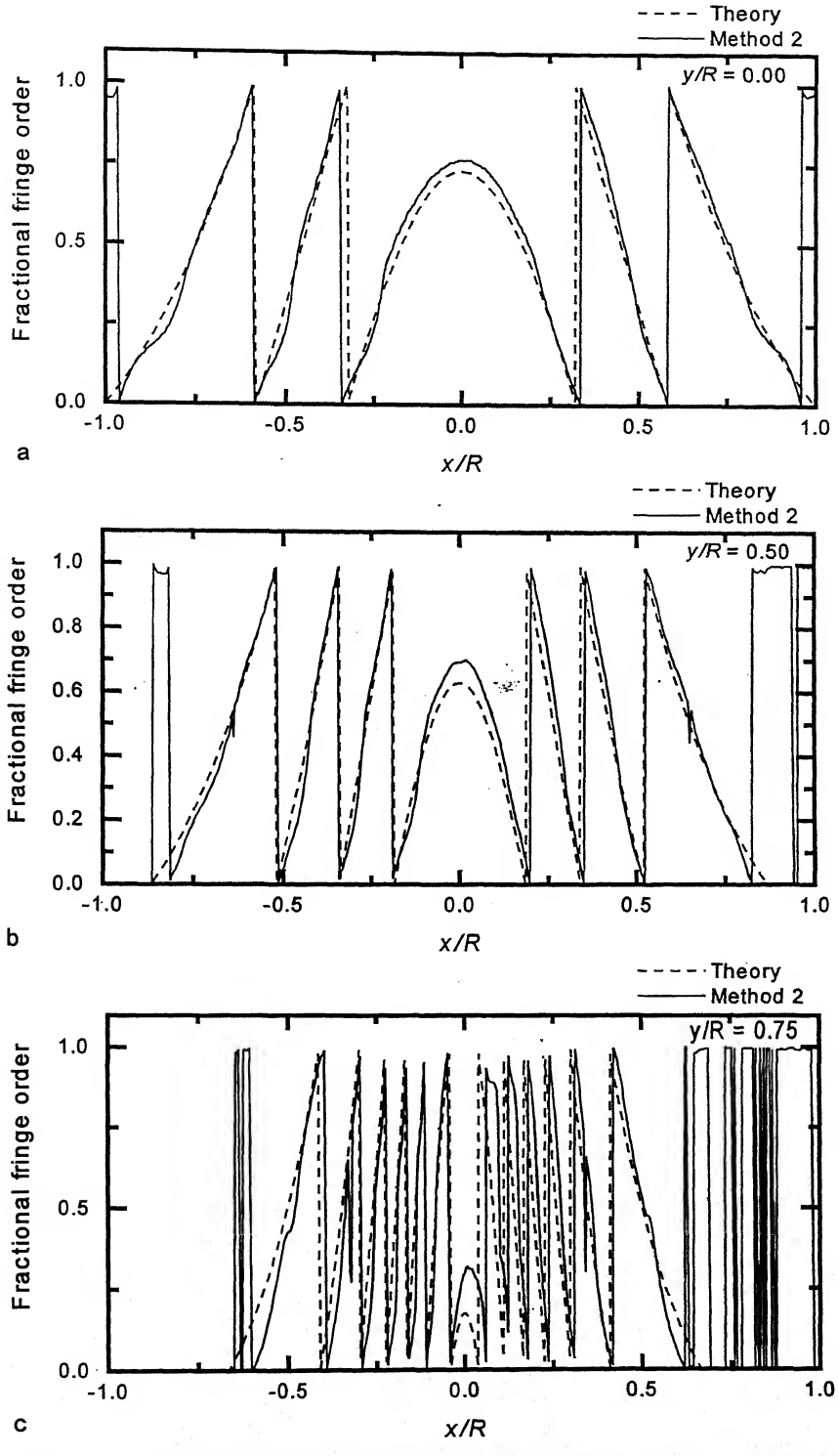

Fig. 2.10. Comparison of fractional fringe order variation for the method of using absolute value of intensity difference (method 2) **a** along diametral line **b** along *r*/2 line **c** along 3*r*/4 line

2.5.2 Using Only Positive Value of Twotheta

In this approach only positive value of 2θ is used in Eq. (2.7). The condition applied is, if 2θ is less than zero then π is added. The result is shown in Fig. 2.11a for the experimentally recorded images and in Fig 2.11b for the theoretically recorded images. The phase map is good for the disk in first and third quadrant while it is bad in second and fourth quadrant for theoretically and experimentally generated images. The phase map calculated based on experimentally recorded images is bad in the regions close to vertical and horizontal diameter. This happens because of non-symmetric intensity patterns. Also the loading direction is not perfectly vertical in the experiment. The fractional fringe order plot for the experimentally recorded disk is shown in Fig. 2.12. Fig 2.11c shows the result for theoretically generated images of ring under diametral compression. This shows that technique applied to the ring does not give the expected results.

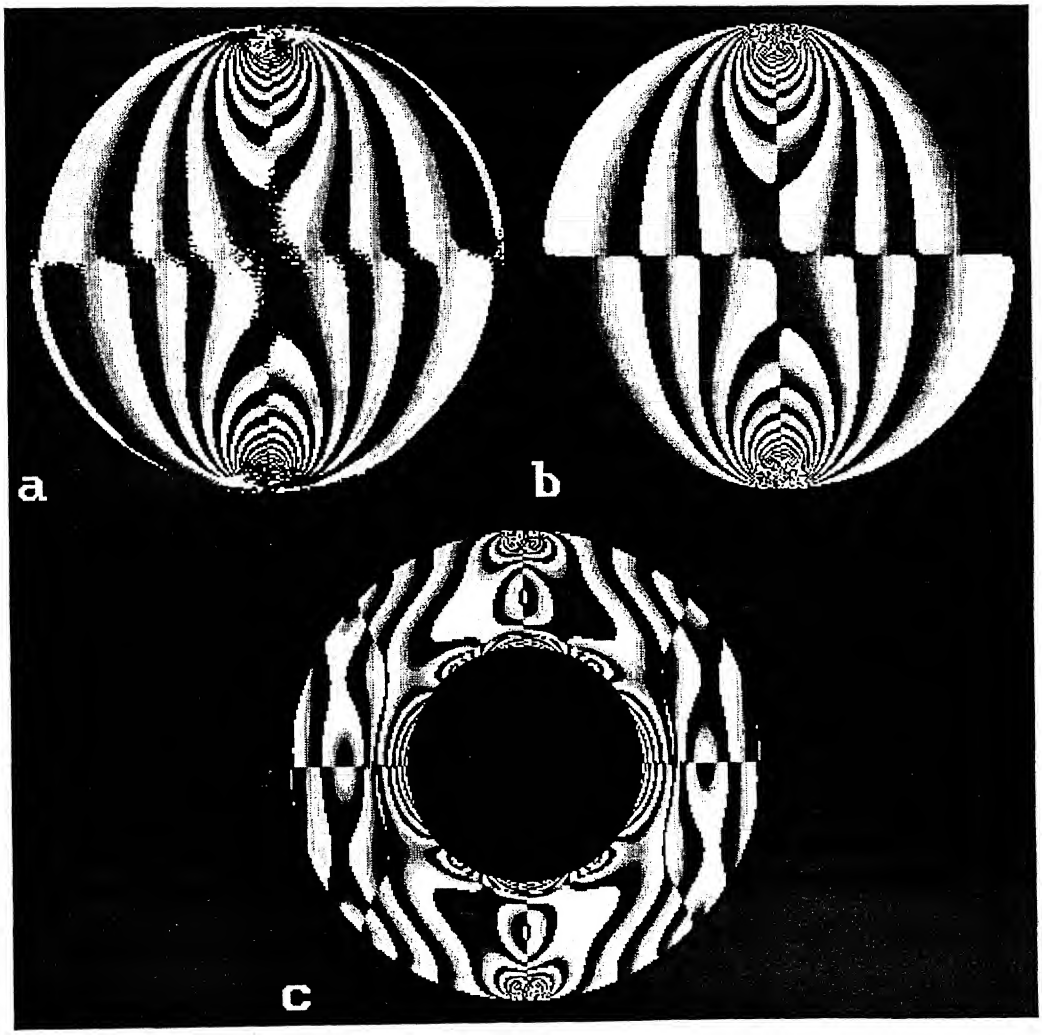

Fig 2.11 Phase maps generated by using positive value of twotheta **a** for experimentally recorded images of disk under diametral compression **b** for theoretically generated images of disk under diametral compression **c** for theoretically generated images of ring under diametral compression

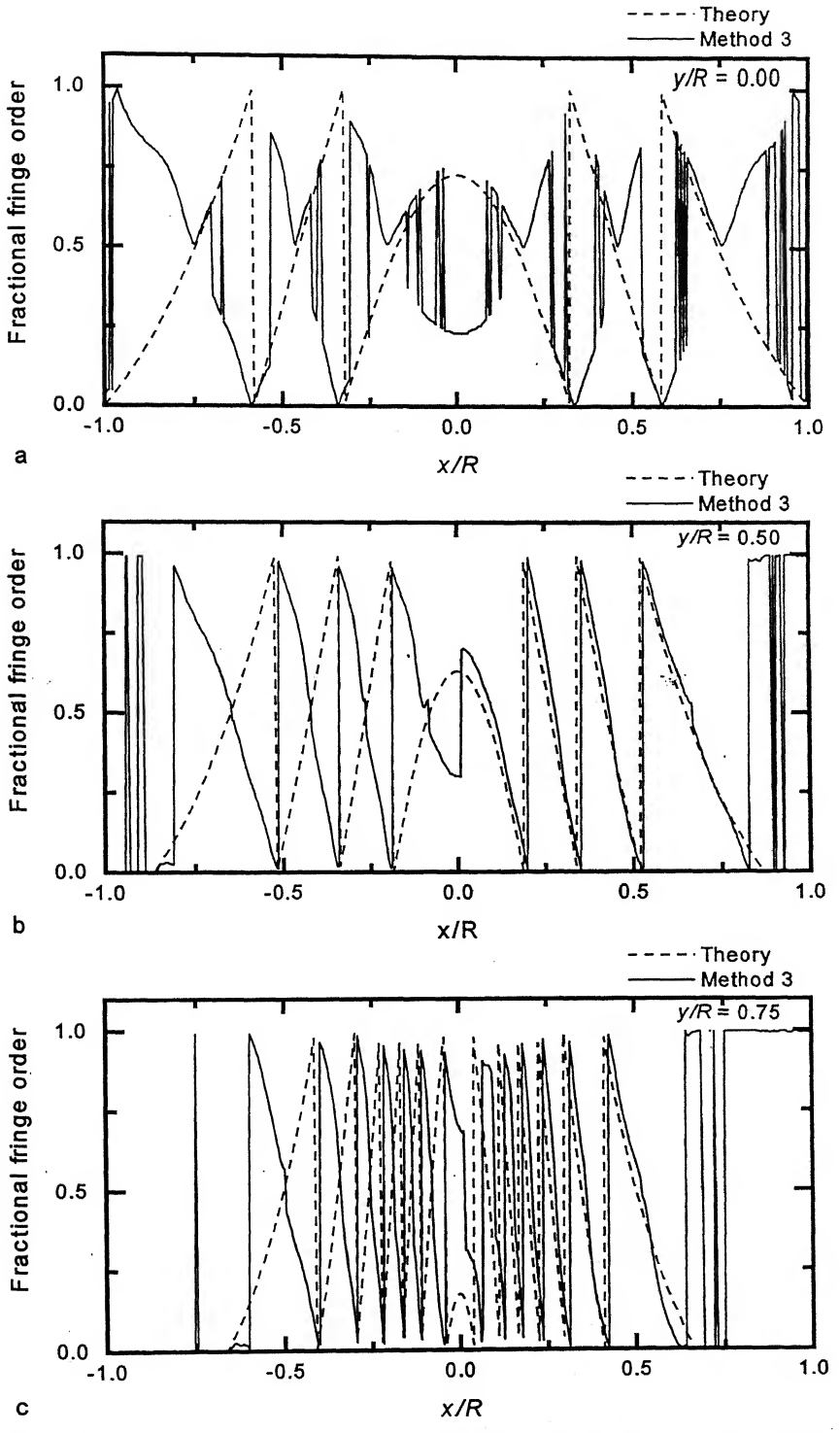

Fig. 2.12. Comparison of fractional fringe order variation for method of using positive values of twotheta (method 3) **a** along diametral line **b** along *r*/2 line **c** along 3*r*/4 line

2.6 Effect of Swapping Images on Phase Map

This study is mainly based on the Eq. (2.7). This study is conducted on theoretical and experimental images of disk under diametral compression (load 773N, dia 60.10 mm, F_σ =11.9973 N/mm/fr). The equations given for six different arrangements in six-step phase shifting algorithm are given in table 2.1. These equations are derived by considering θ for the slow axis. Same exercise can be repeated by considering θ for fast axis. The results are given in Table 2.2. It can be seen that I_1 and I_2 are insensitive to slow or fast axis but for remaining equations, the signs of $\sin 2\theta \sin\delta$ and $\cos 2\theta \sin\delta$ are changed.

Table 2.2. Polariscope arrangement and intensity equations for six-step phase shifting method with reference to θ at fast axis

ξ	η	β	Intensity equation
$3\pi/4$	$\pi/4$	$\pi/2$	$I_1 = I_b + \frac{I_a}{2}(1+\cos\delta)$
$3\pi/4$	$\pi/4$	0	$I_2 = I_b + \frac{I_a}{2}(1-\cos\delta)$
$3\pi/4$	0	0	$I_3 = I_b + \frac{I_a}{2}(1+\sin 2\theta \sin\delta)$
$3\pi/4$	$\pi/4$	$\pi/4$	$I_4 = I_b + \frac{I_a}{2}(1-\cos 2\theta \sin\delta)$
$\pi/4$	0	0	$I_5 = I_b + \frac{I_a}{2}(1-\sin 2\theta \sin\delta)$
$\pi/4$	$3\pi/4$	$\pi/4$	$I_6 = I_b + \frac{I_a}{2}(1+\cos 2\theta \sin\delta)$

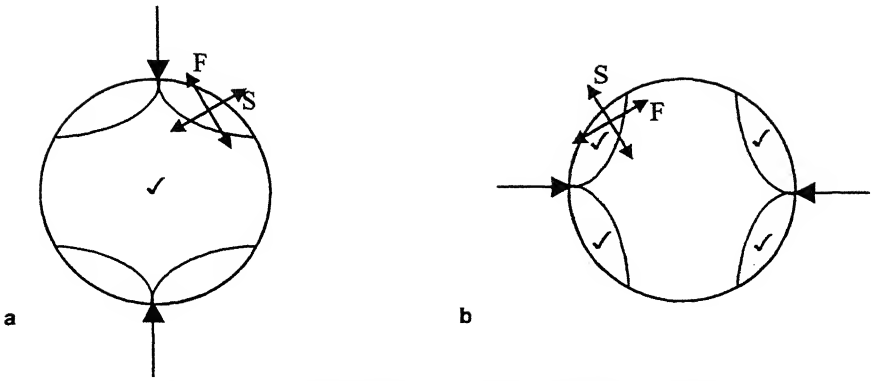

Fig. 2.13. a Load at vertical diameter **b** Load at horizontal diameter

Let us first study the effect of the loading direction on the intensity patterns. The effect of loading direction can be explained by a schematic shown in Figs 2.13a & b. Figure 2.13a shows a disc is vertically loaded while Fig 2.13b shows disc loaded on horizontal diameter. The orientation of slow (S) and fast (F) axis is shown in both the cases. It can be seen that as the loading direction is changed (model along with loading is rotated ccw by 90°) the orientation of the slow and fast axis is also changed spatially. When loading direction is changed by 90° the fast and slow axis are also rotated by 90° spatially. Note that the relative direction with respect to the loading direction is constant. But with respect to the light source the positions of both the axis are swapped. The tick marked portions shown in two figures will have similar gradient in the phase map. A stress frozen disk is used to record images with the loading axis kept vertical and loading axis kept horizontal. Fig 2.14a & b show the set of images of the stress frozen disk kept vertically and horizontally.The Fig 2.15a & b shows the experimental phase map obtained with vertical and horizontal loading directions . Referring to Table 2.2 and Fig. 2.11 one can see that change of loading direction can be equated to the swapping the images (I_4 , I_6) and (I_5 , I_3). The phase map obtained by swapping the images in vertical loading is shown in Fig. 2.15c

Fig 2.14 a Sequence of six images recorded experimentally for a stress-frozen disk with loading direction kept vertically

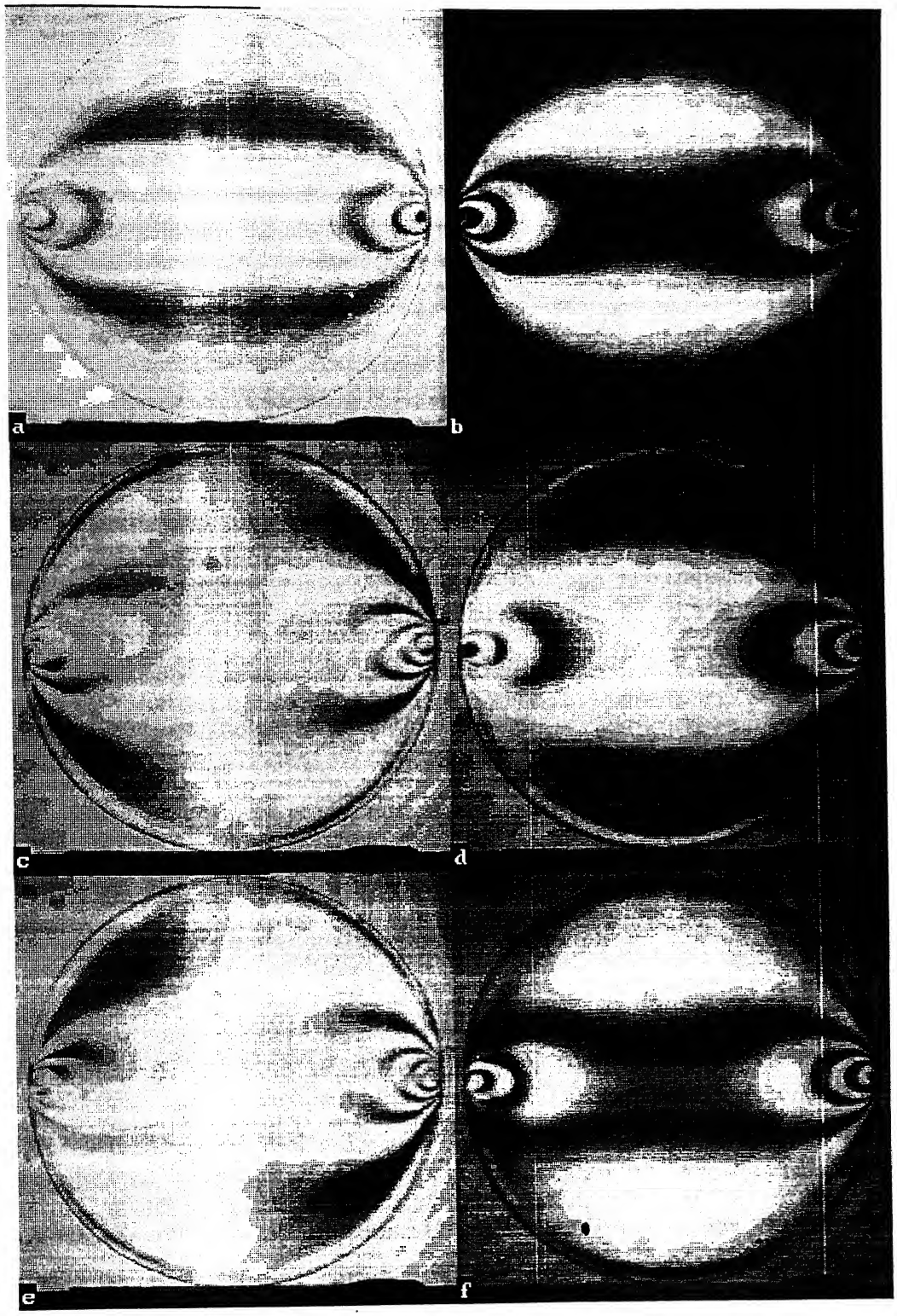

Fig 2.14 b Sequence of six images recorded experimentally for a stress-frozen disk with loading direction kept horizonally

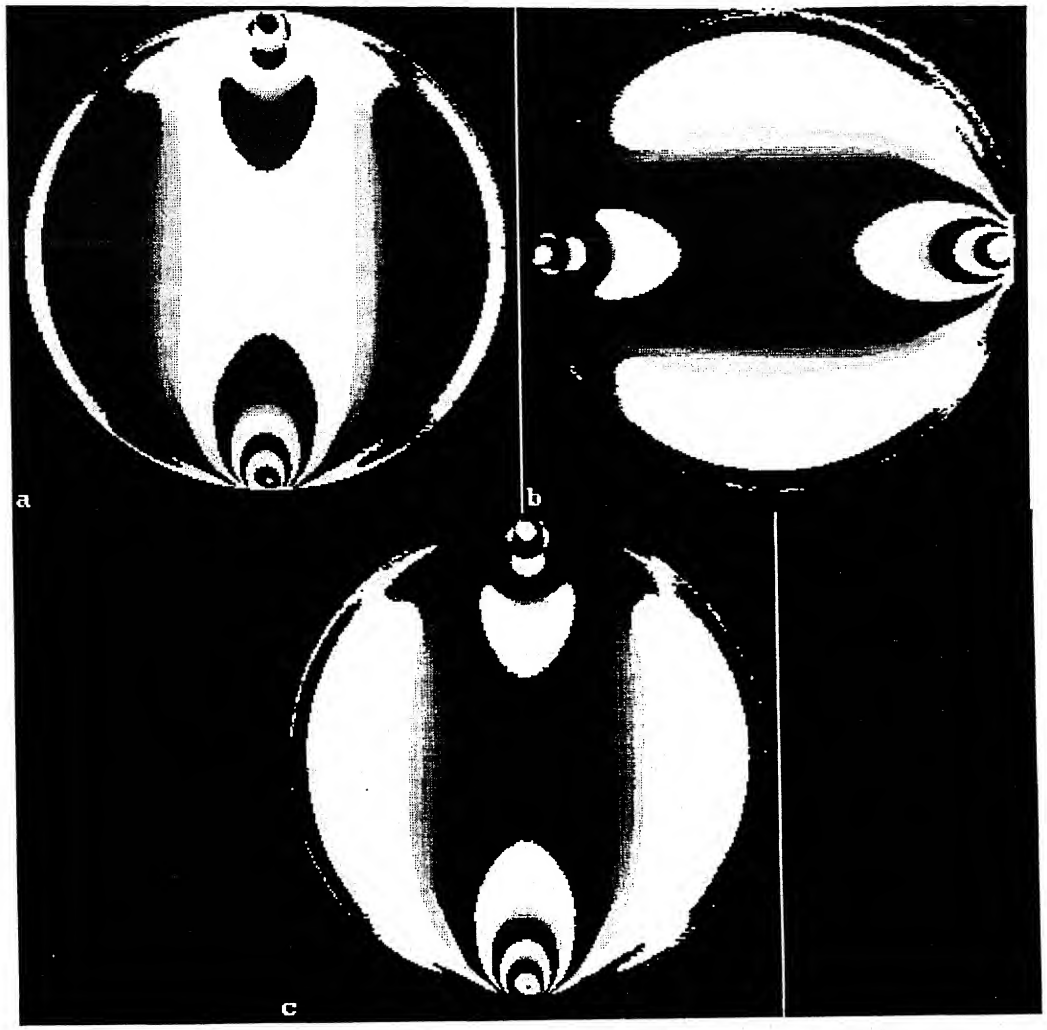

Fig 2.15 Phase maps obtained for the experimentally recorded images of stress-frozen disk **a** For vertical loading direction **b** for horizontal loading direction. **c** swapping the images (I_3 , I_5) &(I_4 , I_6) for vertical loading

2.7 Obtaining Phase Map by Using logical NOT

The Phase map obtained by Eq. (2.7) for theoretically generated images is shown in Fig 2.16a. The images are processed in the sequence given in Table 2.1. This phase map is swapped beyond 45° isoclinic. Fig 2.16b shows a phase map obtained by swapping the images (I_4 , I_6) and (I_5 , I_3). This phase map is correct beyond 45° isoclinic. Theoretically it is possible to patch the regions beyond 45° isoclinic to obtain a correct phase map. This can be done by correctly identifying the areas beyond 45° isoclinic then reading it from Fig 2.16b and putting it in the respective position in the Fig. 2.16a. The other way of doing it is that after identifying the swapped areas in Fig 2.16a replace the pixel by it's logical NOT. The result is shown in Fig 2.16c. This is done by using a standard

software "Matrox Inspector". It has a provision to select an arbitrary region of interest in the given image and process that part only. The result for the experimental images is shown in Fig 2.17a & b. (load 773N, dia 60.10 mm, F_σ =11.9973 N/mm/fr). Thus it is possible to correct the phase maps by using the logical NOT.

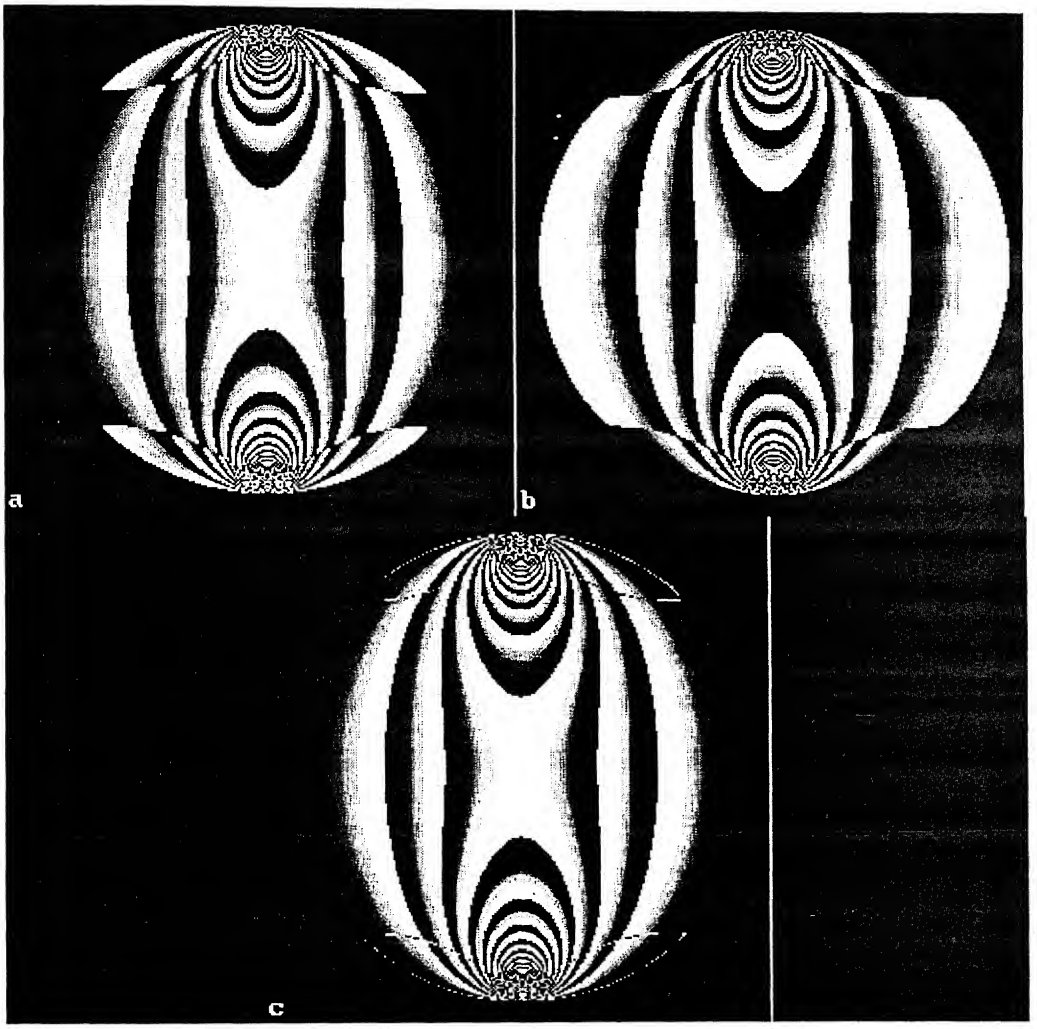

Fig 2.16 Phase maps obtained for theoretically generated images of disk under diametral compression. **a** without swapping the images **b** by swapping the images (I_3 , I_5) &(I_4 , I_6) **c** phase map corrected by taking the NOT of pixel value in Fig 2.16 a

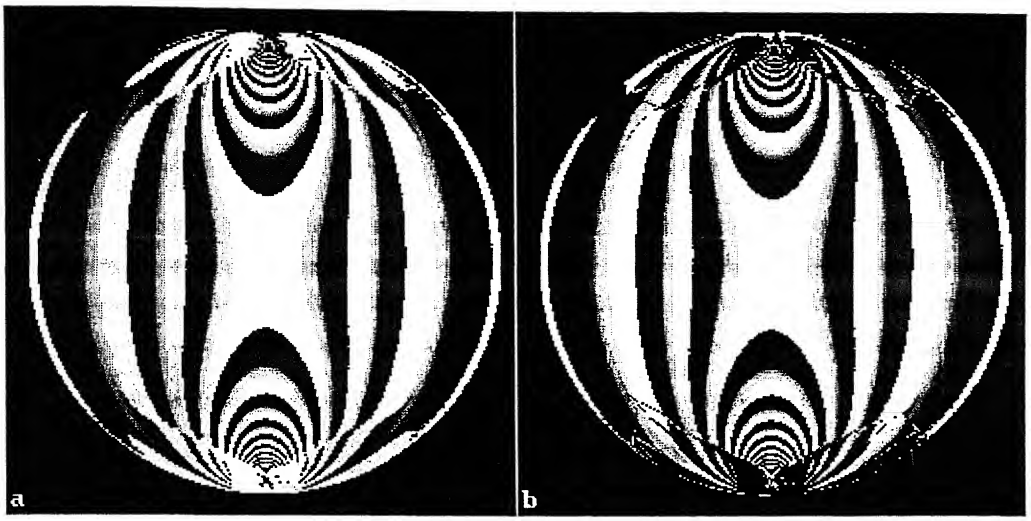

Fig 2.17 Phase maps for experimentally recorded images of disk shown in Fig 2.2 **a** phase map as per the image sequence given in Table 2.1 **b** improved phase map by taking NOT of pixel value

2.8 Closure

Various approaches to obtain a correct phase map in the domain are discussed with their limitations in this chapter. The role of arbitrary orientation of model fast or slow axis is discussed here. The effect of swapping the sequence of intensity maps has been discussed. The use of logical NOT for correcting the phase maps is proposed.

The main reason for not having a correct phase map all over the domain is that the isoclinic parameter obtained is unwrapped. If it is possible to unwrap the isoclinic parameter in the range $-\pi/2$ to $+\pi/2$, then a correct phase map all over the domain can be obtained. Next chapter deals with the comparison of isoclinic parameter in various PST algorithms. Also an approach to obtain isoclinic parameter by using the isochromatic parameter is discussed.

CHAPTER 3

ISOCLINIC PARAMETER CALCULATION IN DIGITAL PHOTOELASTICITY

3.1 Introduction

The evaluation of isoclinic parameter is comparatively easier while determining it manually but the automated evaluation has several problems. The problems concerning the whole field isoclinic parameter evaluation can be roughly divided into the following parts,

1. Numerical inaccuracies.
2. Ambiguity in experimentally evaluating the isoclinic parameter.

The problem of getting numerically correct value depends on the accurate recording and processing of the intensity information. In evaluating this generally arctangent functions are used in calculations. In practical applications due to intensity digitization and quantization, only discrete values are used in the calculations. Also in the regions close to the fringe skeleton, the error increases because of the ratios of small discrete values. Also there is a significant difference in the intensity maps of the images in theoretical and experimental conditions. These reasons lead to an error in the calculations. Besides this, in most of the equations the values returned by the arctangent functions are in the range of $-\pi/4$ to $+\pi/4$ only, which creates the need for unwrapping. It is to be noted that calculations involve inverse trigonometric operations and thus one has a multi-valued solutions, this poses a problem of correctly evaluating the isoclinic parameter. Besides the numerical inaccuracies, there is an ambiguity involved in evaluating the isoclinic parameter experimentally. As it has already been discussed in the previous chapter that model slow and fast axis influence the intensity patterns. In a model, *a priori* one does not know whether the fast or slow axis lies the range $-\pi/4$ to $+\pi/4$. This ambiguity leads to unsuccessful determination of δ_c. Thus the goal of isoclinic parameter evaluation

should be such that it either gives σ_1 or σ_2 direction uniformly all over the domain. This problem could be solved if theta is unwrapped in the range of $-\pi/2$ to $+\pi/2$

In this chapter we shall discuss the reasons of numerical inaccuracies based upon the study of intensity pattern. A comparative study has also been carried out on the evaluation of isoclinics by different algorithms.

3.2 Study of Intensity Pattern Over the Domain

The intensity information represents the properties of the stress field and the orientation of fast or slow axis of the model plays a role on the intensity values. The purpose of this study is to explore the possibility of identifying the orientation of fast and slow axis of the model on purely the intensity values. For the six step phase shifting algorithm, the intensity information considered includes intensities from I_a, I_b & I_1 to I_6, the intensity differences $(I_4 - I_6)$ and $(I_5 - I_3)$. Following set of equations is derived from the equations given in Table 2.1.

$$I_1 - I_2 = I_a \cos\delta \tag{3.1}$$

$$I_5 - I_3 = I_a \sin 2\theta \sin\delta \tag{3.2}$$

$$I_4 - I_6 = I_a \cos 2\theta \sin\delta \tag{3.3}$$

$$I_a = \sqrt{(I_4 - I_6)^2 + (I_5 - I_3)^2 + (I_1 - I_2)^2} \tag{3.4}$$

$$I_b = (I_1 + I_2 - I_a)/2 \tag{3.5}$$

3.2.1 Study of Intensity Variation in Theoretical Images

This study is done on theoretically generated images shown in Fig. 2.4. The plots obtained for the diametral line (y/R = 0.0) are shown in Figs 3.1, 3.2 and 3.3. Figure 3.1 shows the intensity plots for images I_1 to I_6 for the diametral line. Figure 3.2 a, b & c show the variations of intensity differences $(I_1 - I_2)$, $(I_5 - I_3)$ and $(I_4 - I_6)$. Finally Fig. 3.3 represents the plots of calculated I_a, I_b and $\sin 2\theta \sin\delta$, $\cos 2\theta \sin\delta$. Similar results are obtained for a line close to the stress concentration zone (y/R = 0.75). They are shown in Figs. 3.4, 3.5 and 3.6 respectively.

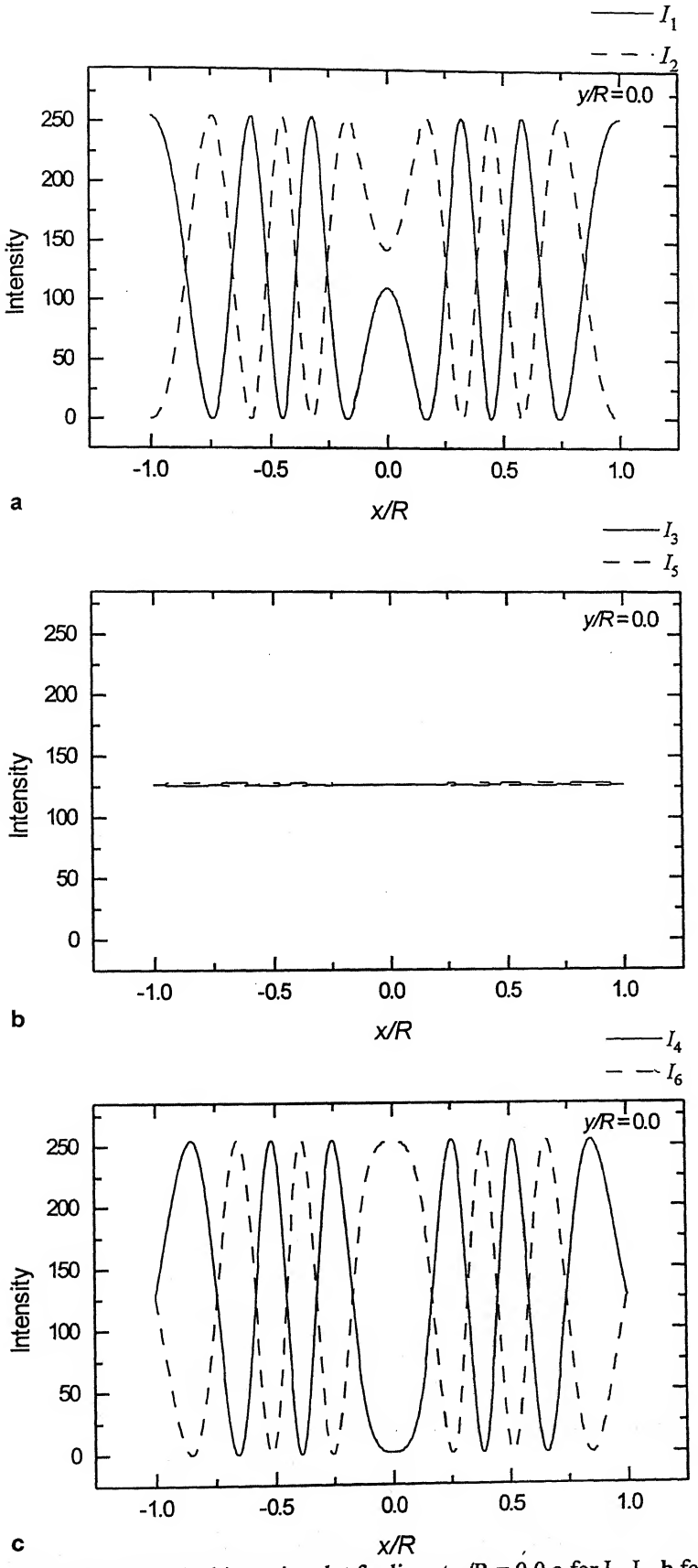

Fig. 3.1. Theoretical intensity plot for line at y/R = 0.0 a for I_1, I_2 b for I_3, I_5 c for I_4, I_6

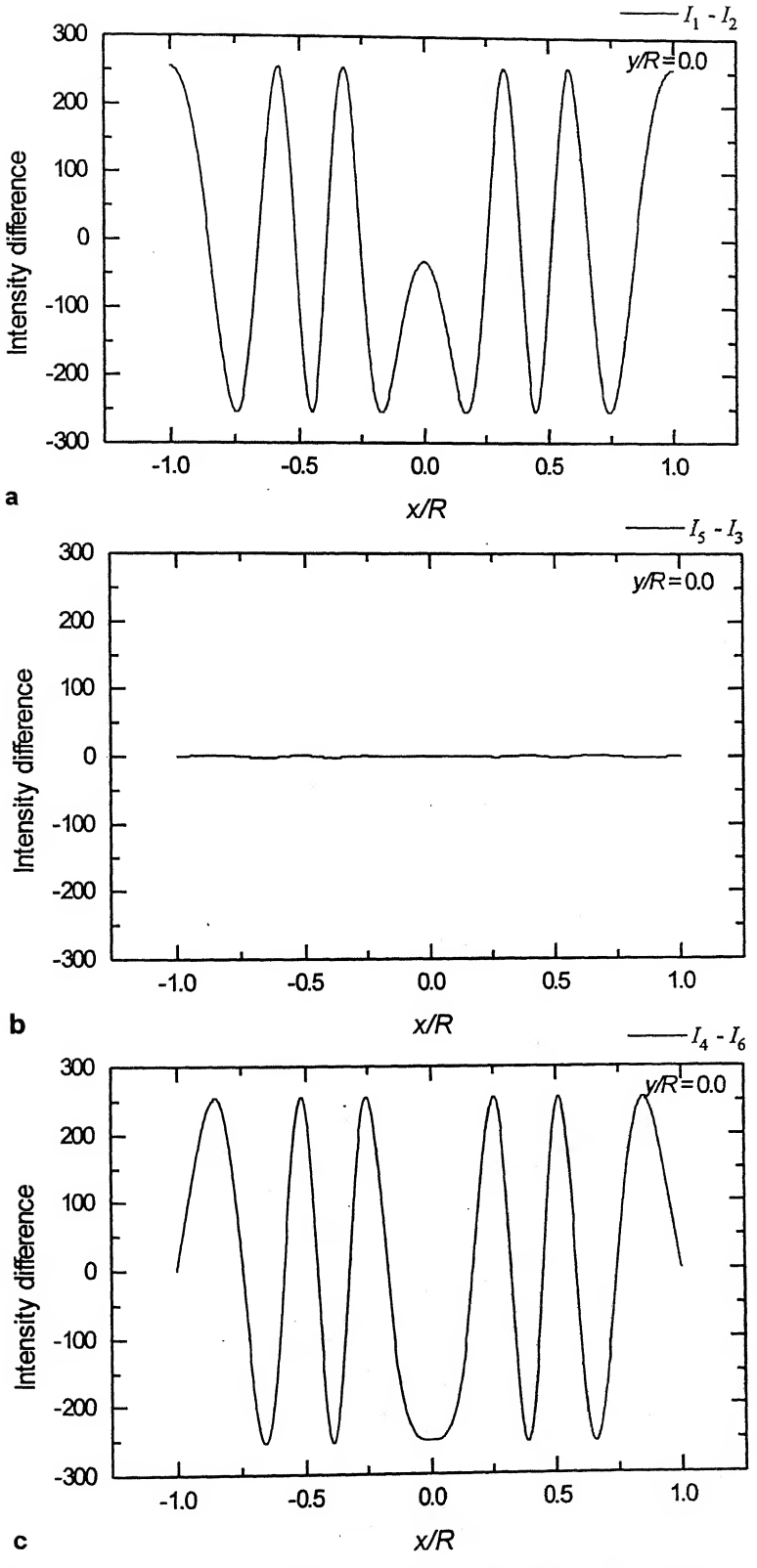

Fig. 3.2. Theoretical plot for for line at y/R = 0.0 **a** ($I_1 - I_2$) **b** for ($I_5 - I_3$) **c** for ($I_4 - I_6$)

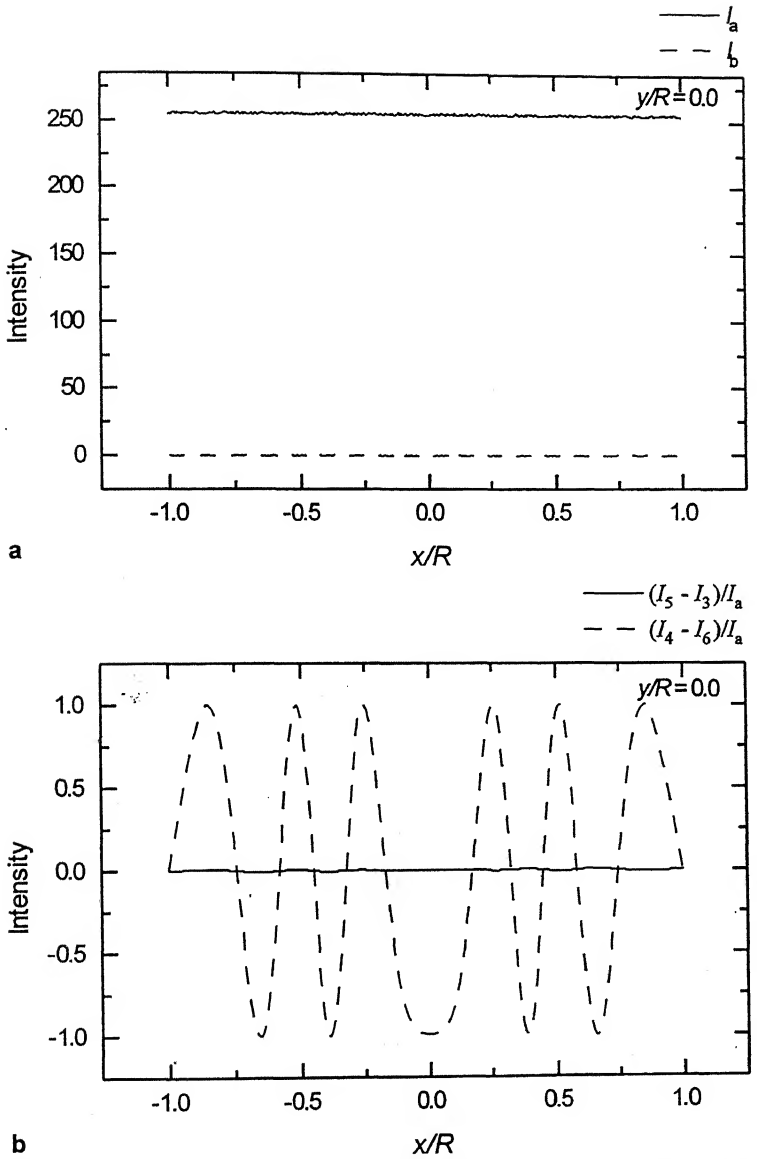

Fig. 3.3. Theoretical intensity plot for for line at y/R = 0.0 **a** I_a, I_b **b** for $(I_5 - I_3)/I_a$ **c** for $(I_4 - I_6)/I_a$

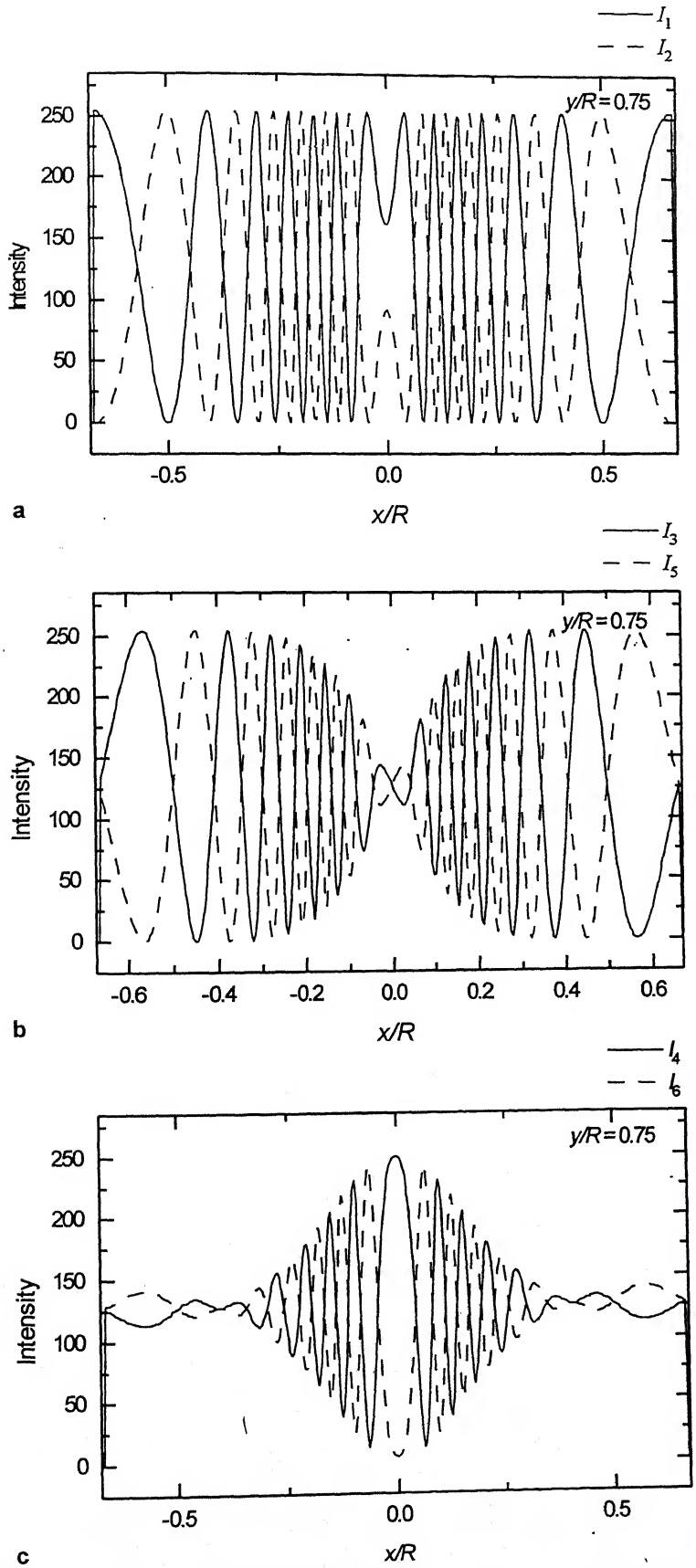

Fig. 3.4. Theoretical intensity plot for line at y/R = 0.75 **a** I_1, I_2 **b** for I_3, I_5 **c** for I_4, I_6

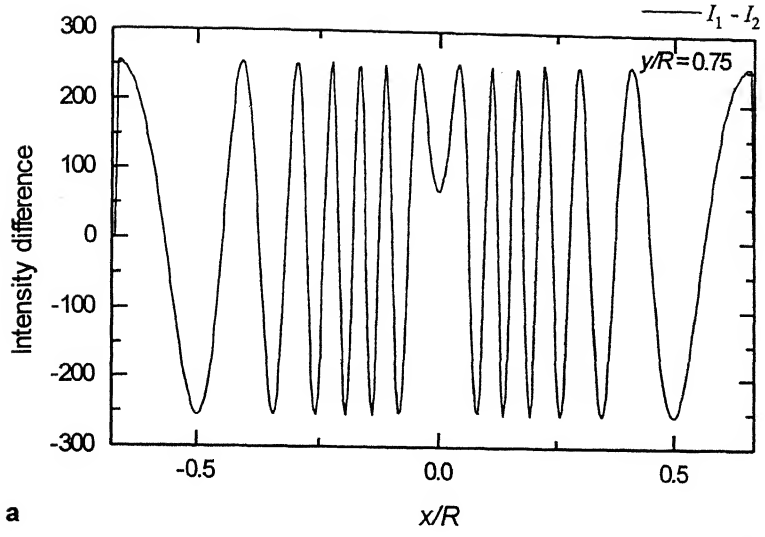

a

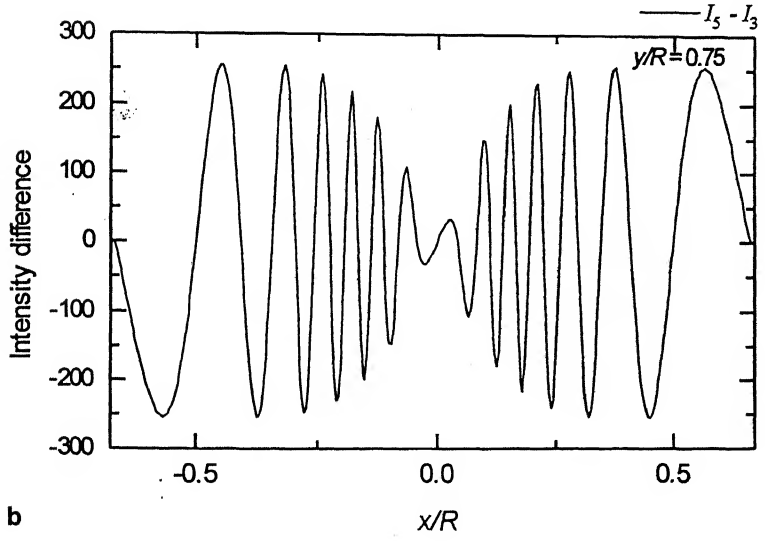

b

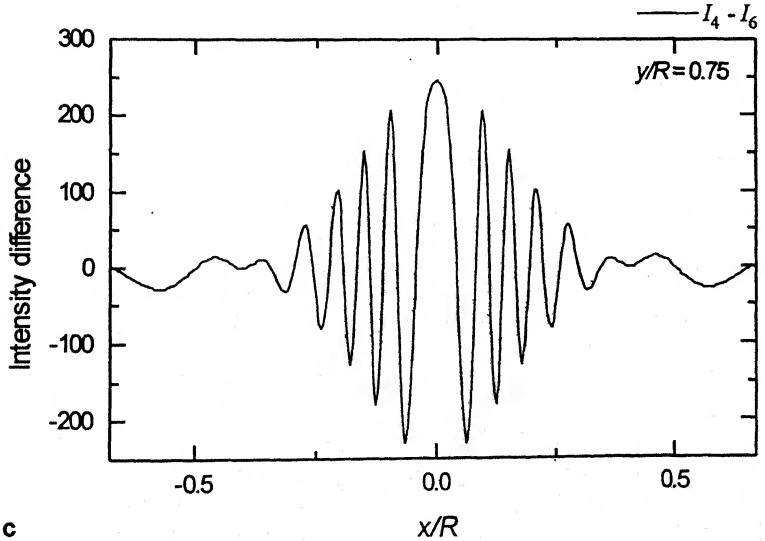

c

Fig. 3.5. Theoretical plot for line at y/R = 0.75 **a** ($I_1 - I_2$) **b** for ($I_5 - I_3$) **c** for ($I_4 - I_6$)

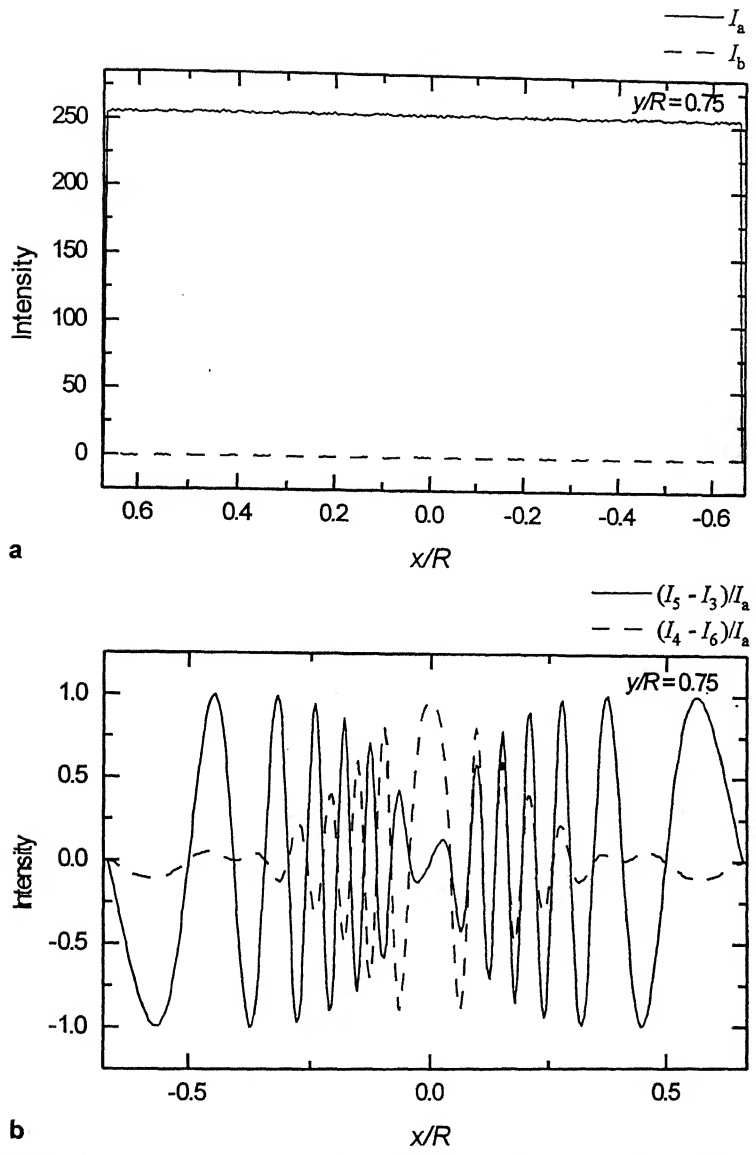

Fig. 3.6. Theoretical intensity plot for line at y/R = 0.75 **a** I_a, I_b **b** for ($I_5 - I_3$)/ I_a **c** for ($I_4 - I_6$)/ I_a

It can be observed in Fig 3.1 and Fig 3.4 that the intensity maps are symmetric about the loading axis. Also the variation is smooth and periodic. As we move towards the loading point, the frequency is increased. The amplitude is constant in case of I_1 and I_2. In case of I_3 and I_5 the amplitudes are decreasing towards the loading line and in the case of I_4 and I_6 the amplitudes are increasing towards the loading line. Same trend is reflected in case of intensity differences $(I_1 - I_2)$, $(I_5 - I_3)$ and $(I_4 - I_6)$. But the only things which remain unchanged are I_a and I_b. Theoretically the value of I_a and I_b remain constant at 255 and 0 respectively all over the domain.

3.2.2 Study of Intensity Pattern in Experimental Images

This study is done on experimentally recorded images shown in Fig. 2.2. The plots obtained for the diametral line (y/R = 0.0) are shown in Fig. 3.7, 3.8 and 3.9. Figure 3.7 shows the intensity plots for images I_1 to I_6 for the diametral line. Figure 3.8 a, b & c show the variations of intensity differences $(I_1 - I_2)$, $(I_5 - I_3)$ and $(I_4 - I_6)$. Finally Fig. 3.9 represents plots of calculated values of I_a, I_b and $\sin 2\theta \sin\delta$, $\cos 2\theta \sin\delta$. Similar results are obtained for a line close to the stress concentration zone (y/R = 0.75). They are shown in Fig. 3.10, 3.11 and 3.12 respectively. It can be observed in Fig 3.10 and Fig 3.11 that the intensity maps are non-symmetric about the loading axis. Even though the variation is smooth, it is not exactly periodic. As we move towards the loading point, the frequency is increased. The amplitude also is not constant. In case of I_3 and I_5 the amplitudes are decreasing towards the loading line and in the case of I_4 and I_6 the amplitudes are increasing towards the loading line. Same trend is reflected in case of intensity differences $(I_1 - I_2)$, $(I_5 - I_3)$ and $(I_4 - I_6)$. It can be seen in Figs. 3.9a & 3.12a that I_a and I_b are not constant on the given line of interest. Here I_a and I_b. do not remain constant all over the domain. Since I_a is a function of time, I_b also becomes a function of time. Both the parameters change with the position also. Because of this it is not possible to remove the effect of I_a and I_b completely. This is one of the reasons affecting the accuracy of the isoclinic parameter.

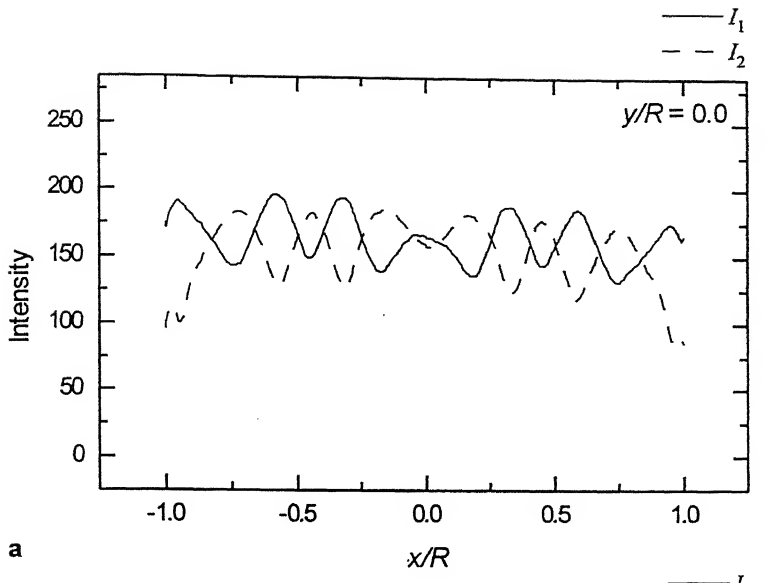

a

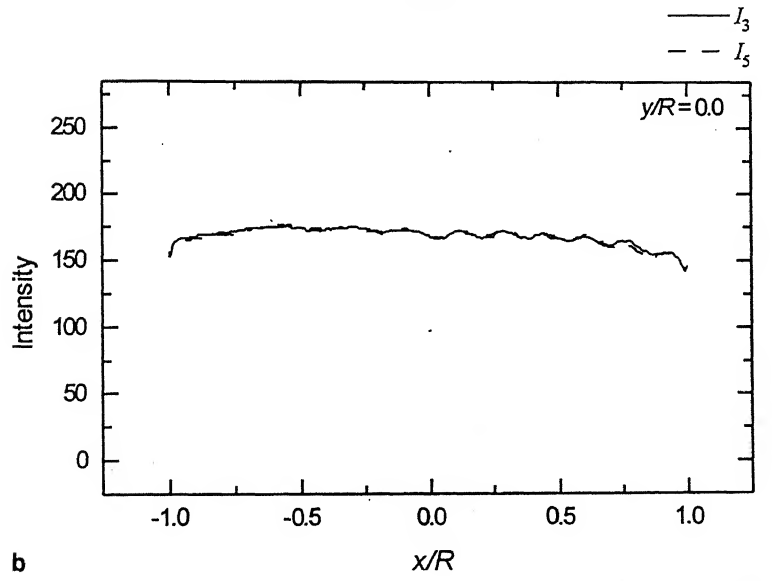

b

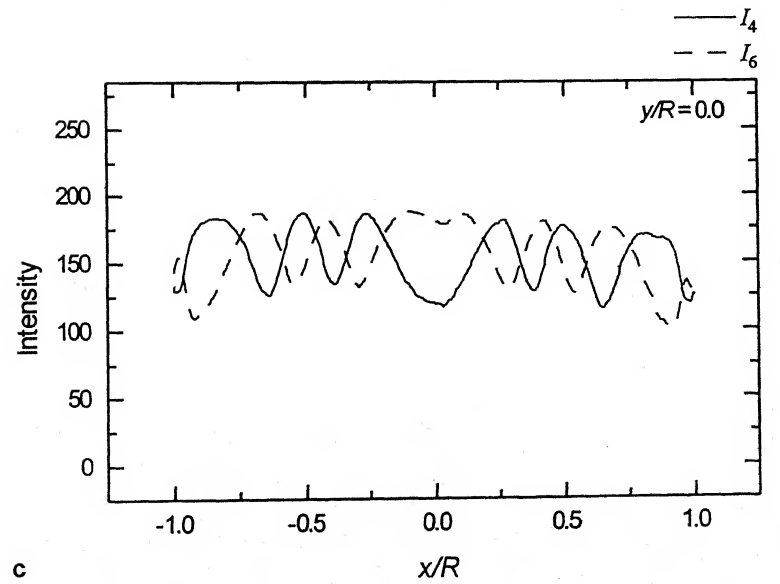

c

Fig. 3.7 Experimental intensity plot for line at y/R = 0.0 a I_1, I_2 b for I_3, I_5 c for I_4, I_6

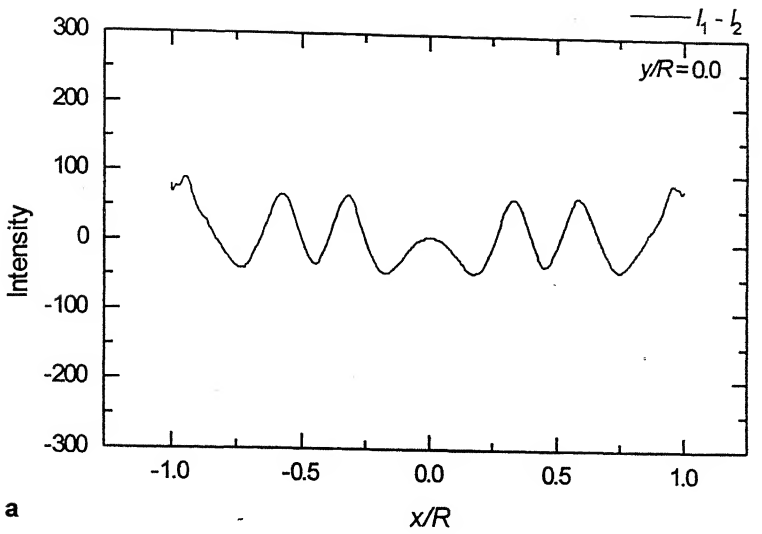

a

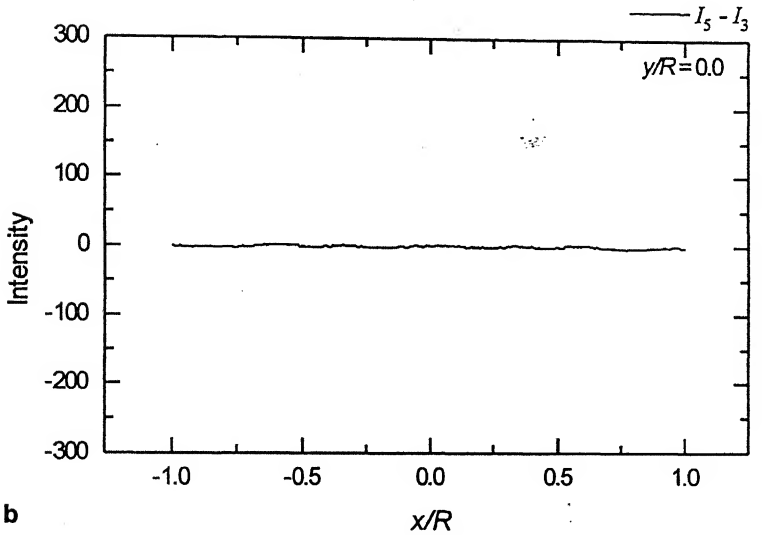

b

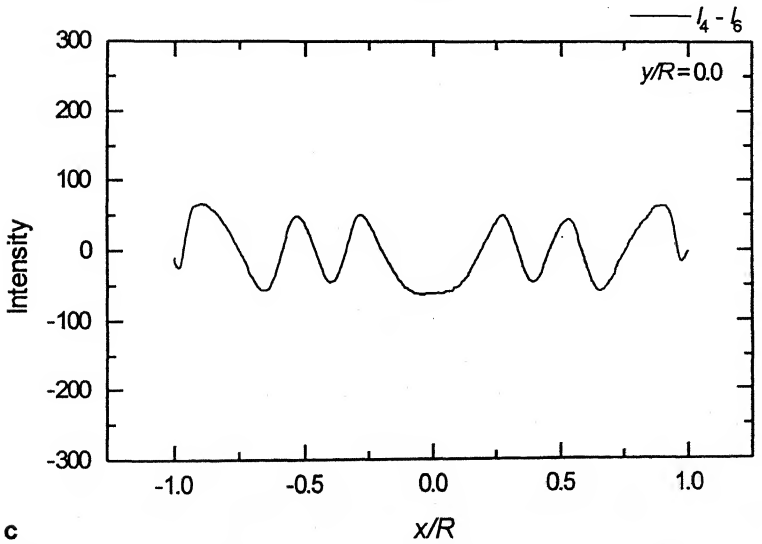

c

Fig. 3.8. Experimental plot for line at y/R = 0.0 a ($I_1 - I_2$) b for ($I_5 - I_3$) c for ($I_4 - I_6$)

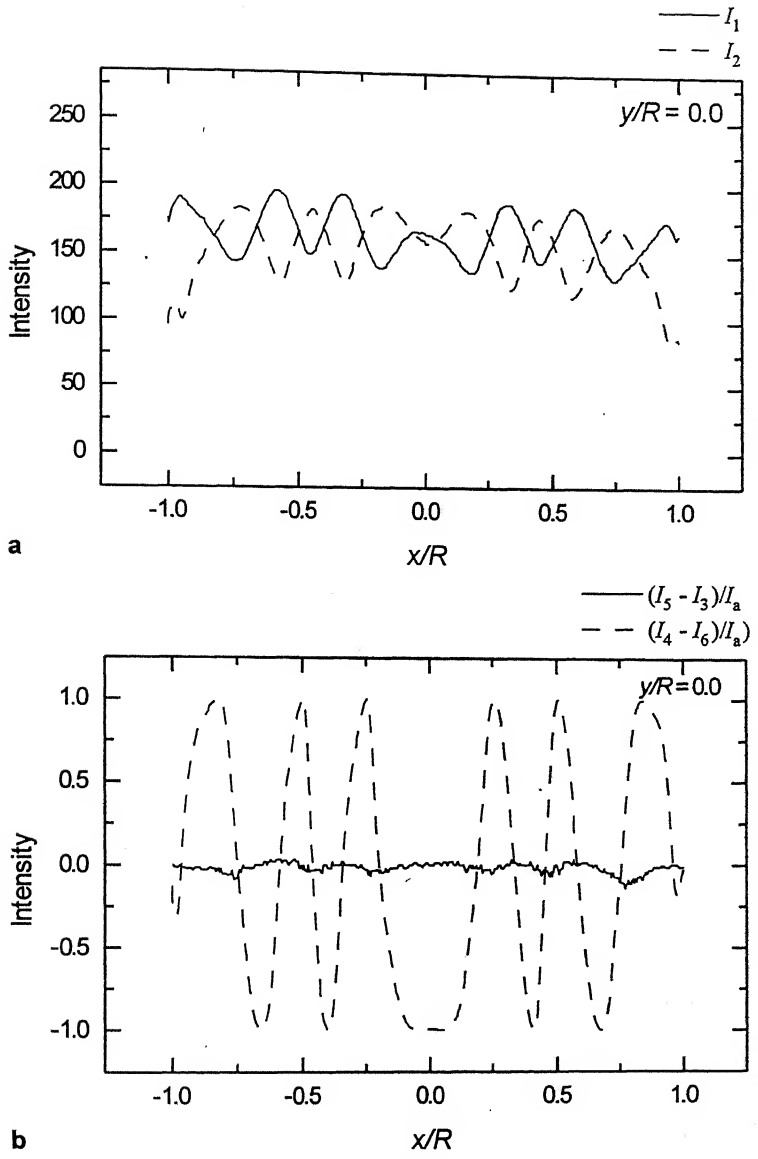

Fig. 3.9. Experimental intensity plot for line at y/R = 0.0 **a** I_a, I_b **b** for ($I_5 - I_3$)/ I_a **c** for ($I_4 - I_6$)/ I_a

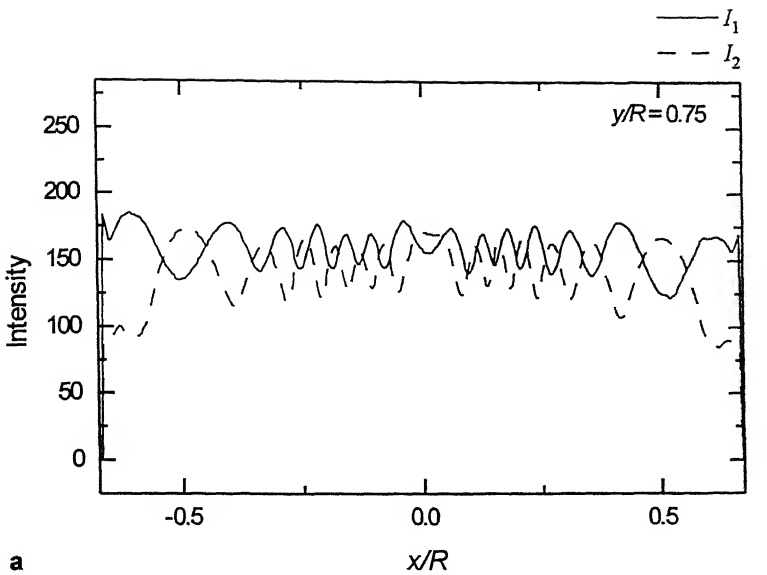

a

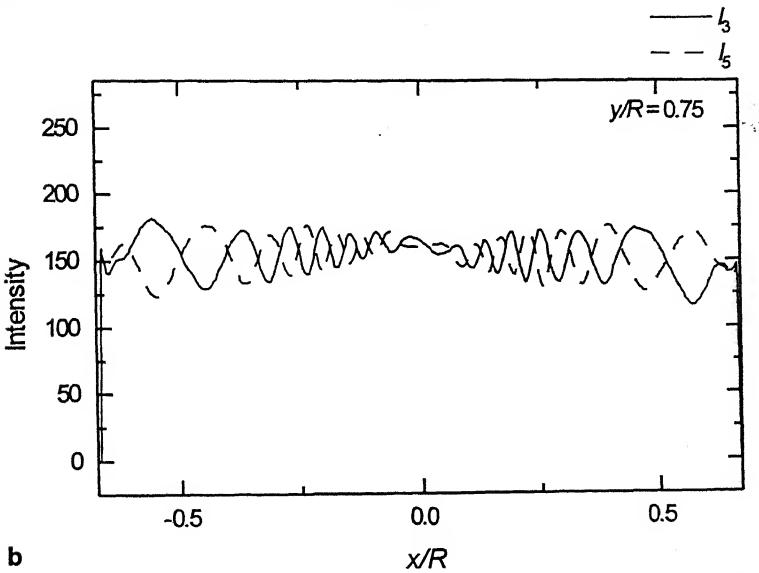

b

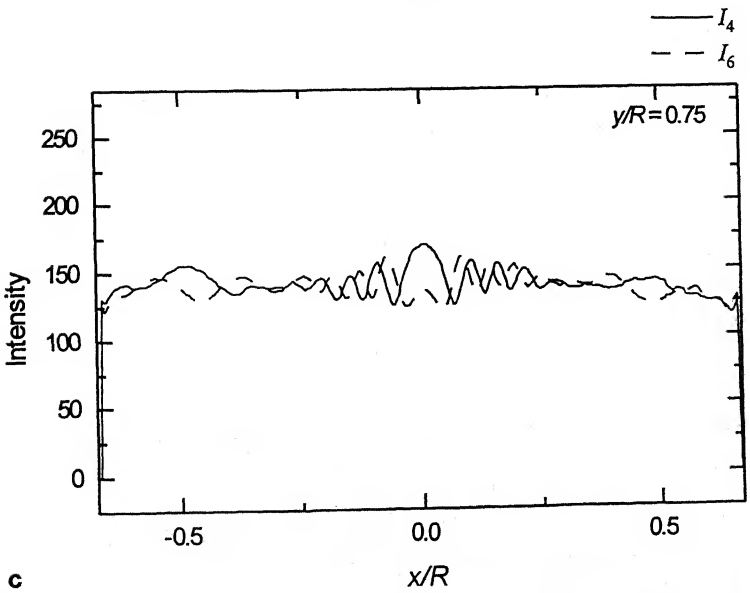

c

Fig. 3.10. Experimental intensity plot for line at y/R = 0.75 **a** I_1, I_2 **b** for I_3, I_5 **c** for I_4, I_6

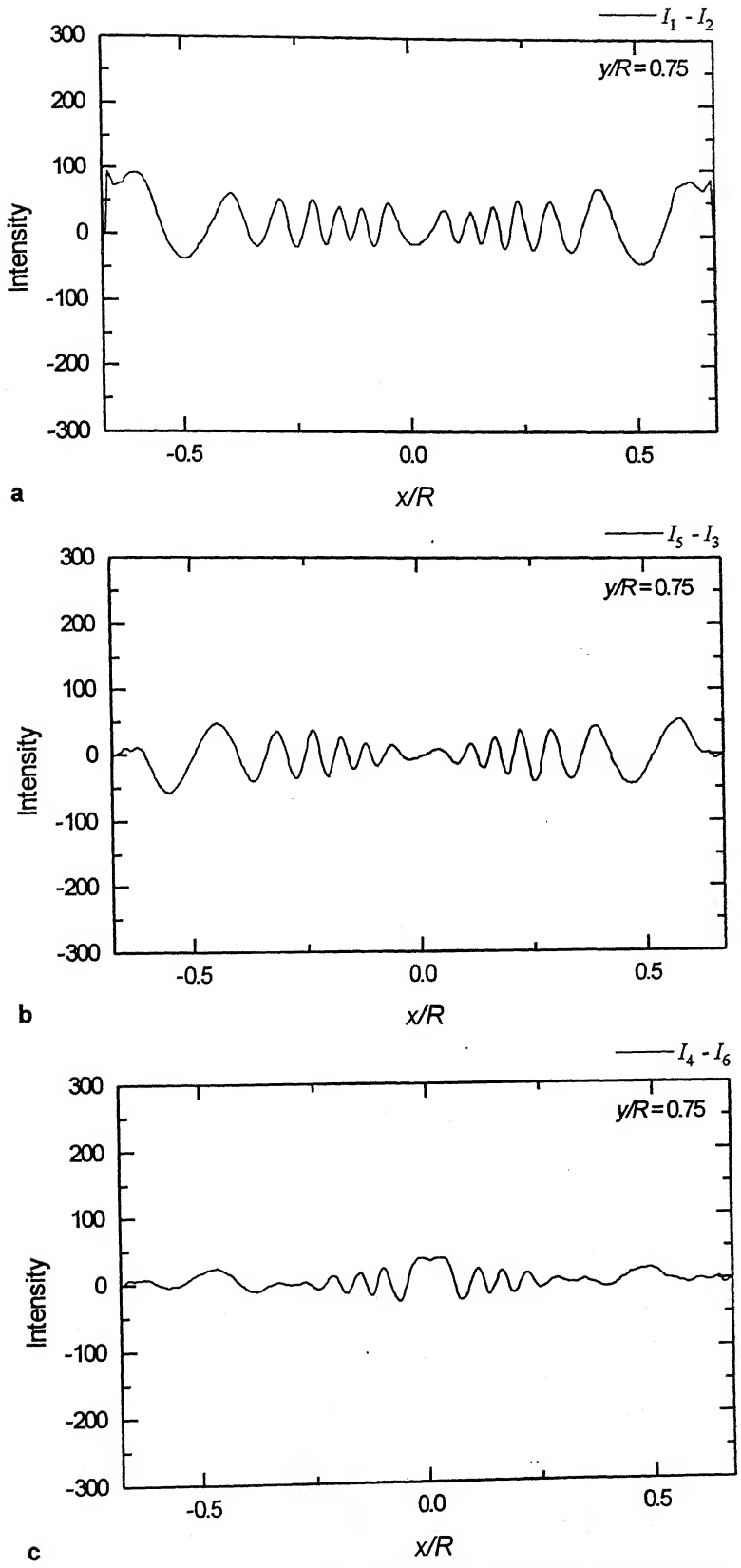

Fig. 3.11. Experimental plot for line at y/R = 0.75 **a** ($I_1 - I_2$) **b** for ($I_5 - I_3$) **c** for ($I_4 - I_6$)

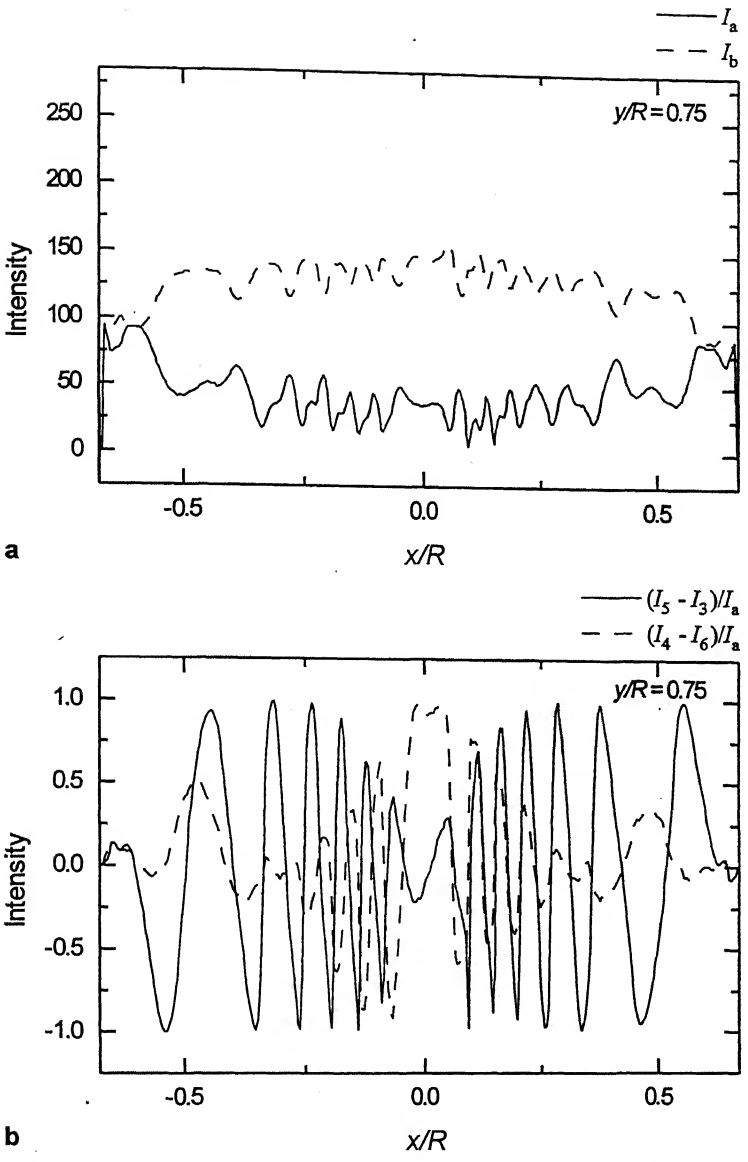

Fig. 3.12. Experimental intensity plot for line at y/R = 0.75 **a** I_a, I_b **b** for $(I_5 - I_3)/ I_a$ and $(I_4 - I_6)/ I_a$

3.3 Evaluation of Isoclinic Parameter by using Retardation Parameter

Generally isoclinic parameter is calculated first and then it is used to calculate the isochromatic parameter. Correct determination of isochromatic parameter depends on whether the isoclinic value determined represents uniformly either σ_1 or σ_2 over the domain. In the previous section an attempt was made to identify the σ_1 or σ_2 direction based on the intensity values, typically I_3. Referring to Eq. (3.2) & (3.3) the sign of R.H.S. depends on both θ and δ. Hence no general conclusion was possible. On the other hand if δ is known correctly, it is possible to evaluate θ. Recently Dhiraj [6] has proposed a method to calculate δ unambiguously over the domain. In this section the possibility of arriving at the correctly unwrapped value of θ by using δ is studied theoretically. The results are obtained on theoretically generated images. The expression derived is based on the six step phase shifting algorithm.

From Eq. (3.2)

$$\sin 2\theta = \frac{I_5 - I_3}{I_a \sin\delta} \tag{3.6}$$

$$2\sin\theta\cos\theta = \frac{I_5 - I_3}{I_a \sin\delta} \tag{3.7}$$

$$\cos 2\theta = \frac{I_4 - I_6}{I_a \sin\delta} \tag{3.8}$$

$$2\cos^2\theta - 1 = \frac{I_4 - I_6}{I_a \sin\delta} \tag{3.9}$$

$$2\cos^2\theta = \frac{I_4 - I_6}{I_a \sin\delta} + 1 \tag{3.10}$$

$$2\cos^2\theta = \frac{(I_4 - I_6) + I_a \sin\delta}{I_a \sin\delta} \tag{3.11}$$

Dividing Eq (3.7) by Eq. (3.11)

$$\tan\theta = \frac{(I_5 - I_3)}{(I_4 - I_6) + I_a \sin\delta} \tag{3.12}$$

This equation gives the value of theta in the range $-\pi/2$ to $+\pi/2$. Fig 3.13 shows the theoretically generated images for the disk. Figure 3.14 shows the phase map obtained by quadrant approach.. The isoclinic plot obtained for theta in case of theoretically generated disk by using Eq 2.4 are shown in Fig. 3.15a. While Fig 3.15b. shows isoclinic plots obtained by using Eq. 3.12. Fig 3.16 shows the results obtained on line $y/R = 0.9375$. It can be seen that the theta obtained by new formula puts the unwrapped value of theta. It very closely follows the line for theoretical theta over the line of interest. But it also contains spikes where the results by Eq. 2.4 shows the spikes. In this case the spikes are higher. This will happen where $\delta = 0, \pi, 2\pi, \ldots\ldots$. Thus theoretically it is possible to unwrapp theta by using δ. Theta obtained so is continuous. But experimentally this may not be the case, since the value of δ obtained all over the domain by load stepping may have certain noise points or some errors. These things may affect the theta calculation. Secondly experimentally obtained theta may have more discontinuities in the domain. Hence one needs to check for such problems. This demands a post-processing of obtained results from the user.

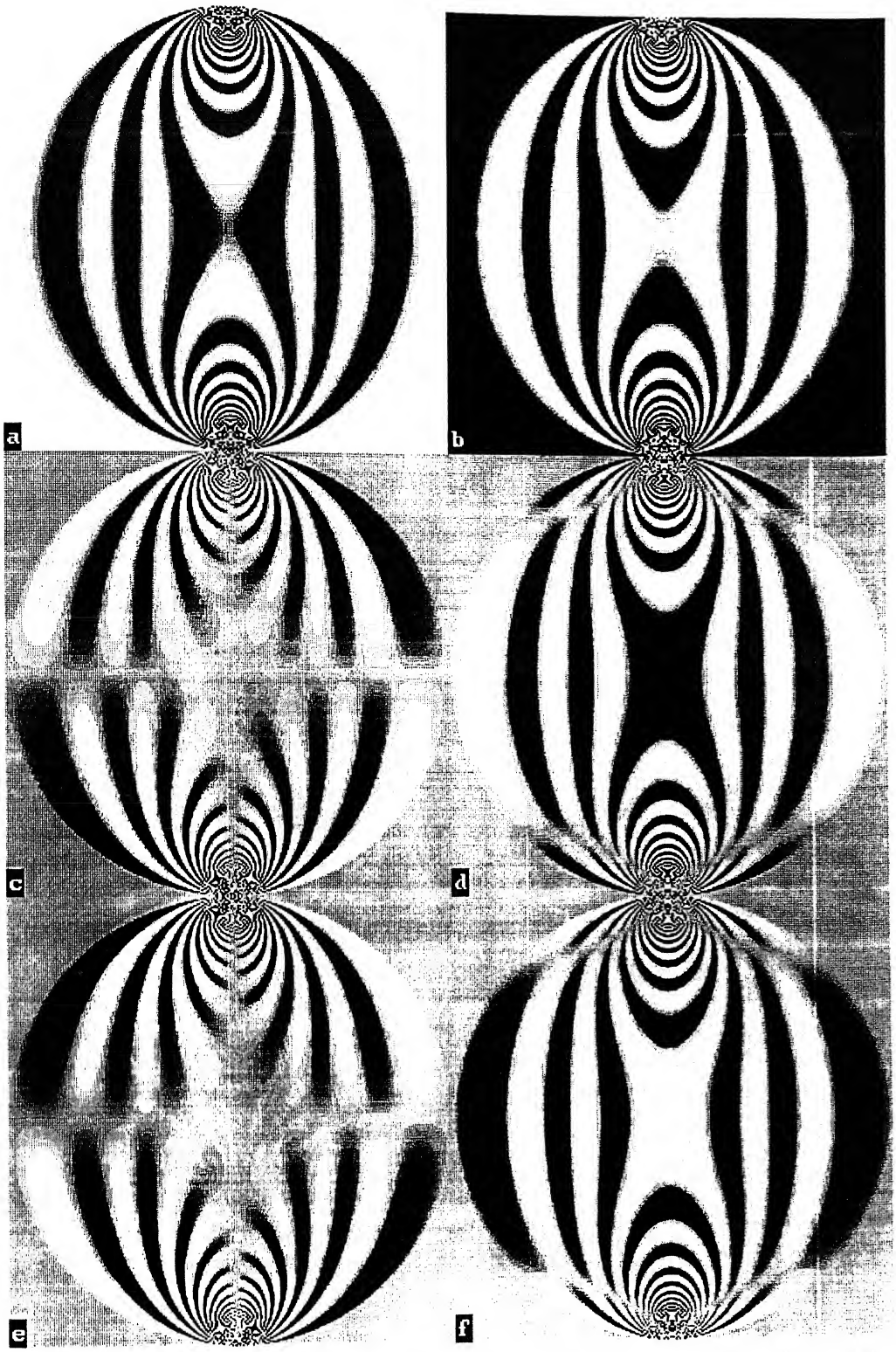

Fig 3.13 Sequence of six images generated theoretically as per the sequence in Table 2.1for the disk under diametral compression (load 773 N, dia. 60 mm, thickness 6.28 mm, F_σ = 11.9973 N/mm/fringe)

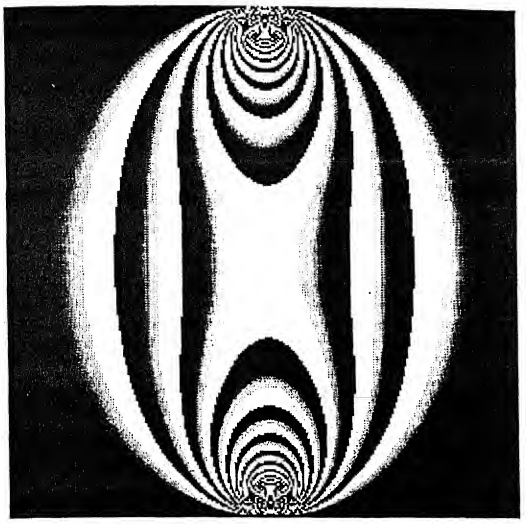

Fig 3.14 Phase map obtained by quadrant approach for the theoretically generated images given in Fig. 3.13

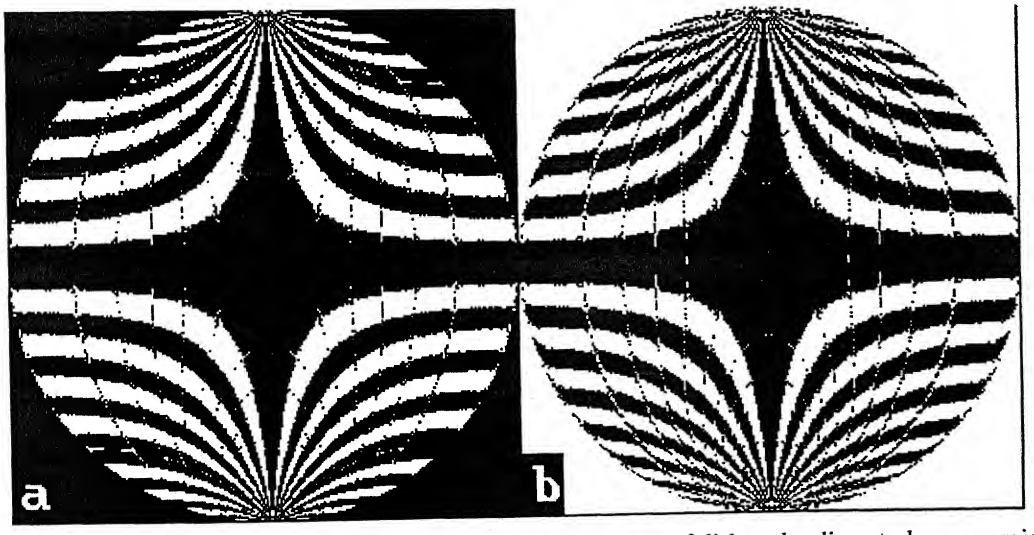

Fig 3.15 Isoclinic plots for the theoretically generated images of disk under diametral compression **a** by method of Patterson & Wang (Eq. 3.13) **b** by new approach (Eq. 3.12)

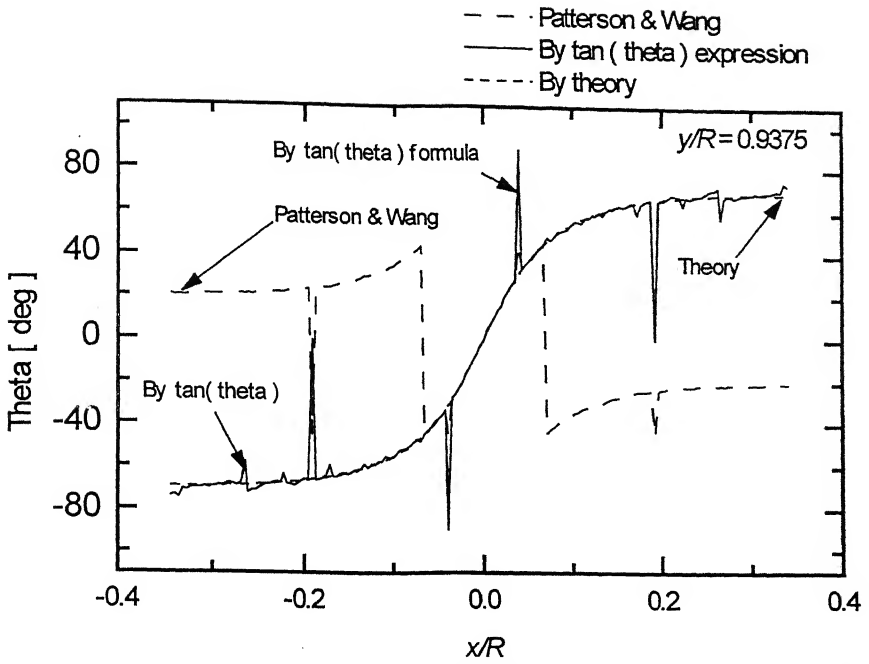

Fig. 3.16 Plot of theoretical theta by Patterson & Wang, theoretical theta by modified expression, theta by theory.

3.4 Evaluation of Isoclinic Parameter in Circular Polariscope

For the study of evaluation of isoclinic parameter in circular polariscope, six step phase shifting algorithms proposed by Patterson & Wang and Ajovalasit et. al. are considered. The study is done for the problem of ring under diametral compression and for the problem of disk under diametral compression. The study is done on two different loads.

3.4.1 Algorithm by Patterson and Wang.

Arrangements suggested by Patterson and Wang [1] are summarised in Table 3.1.

Table 3.1. Optical arrangements for Patterson and Wang.

Patterson and Wang

$3\pi/4$	0	$\pi/4$	$I_1 = I_b + \frac{I_a}{2}(1+\cos\delta)$
$3\pi/4$	0	$3\pi/4$	$I_2 = I_b + \frac{I_a}{2}(1-\cos\delta)$
$3\pi/4$	0	0	$I_3 = I_b + \frac{I_a}{2}[1-\sin 2\theta \sin\delta]$
$3\pi/4$	$\pi/4$	$\pi/4$	$I_4 = I_b + \frac{I_a}{2}[1+\cos 2\theta \sin\delta]$
$3\pi/4$	$\pi/2$	$\pi/2$	$I_5 = I_b + \frac{I_a}{2}[1+\sin 2\theta \sin\delta]$
$3\pi/4$	$3\pi/4$	$3\pi/4$	$I_6 = I_b + \frac{I_a}{2}[1-\cos 2\theta \sin\delta]$

Using the equations listed in Table 3.1, the isoclinic parameter is obtained as

$$\theta_c = \frac{1}{2}\tan^{-1}\left(\frac{I_5 - I_3}{I_4 - I_6}\right) = \frac{1}{2}\tan^{-1}\left(\frac{I_a \sin\delta \sin 2\theta}{I_a \sin\delta \cos 2\theta}\right) \quad \text{for } \sin\delta \neq 0 \tag{3.13}$$

Use of atan() function is recommended to calculate theta from the above equation. The experimentally recorded images are shown in Fig. 3.17

3.4.2 Algorithm by Ajovalasit et. al.

Ajovalasit et al [1]. proposed the use of both left and right circularly polarised light to arrive at an optical arrangement that minimises the error due to mismatch of quarter-wave plate error. The optical arrangements proposed by them and the intensity equations are shown in Table 3.2. Arrangements suggested by Ajovalasit et al. are summarised in Table 3.2.

Table 3.2. Optical arrangements for Ajovalasit et. al.

Ajovalasit et. al.

$3\pi/4$	$\pi/4$	$\pi/4$	$I_1 = I_b + \frac{I_a}{2}(1+\cos\delta)$
$3\pi/4$	$\pi/4$	0	$I_2 = I_b + \frac{I_a}{2}(1-\cos\delta)$
$3\pi/4$	0	0	$I_3 = I_b + \frac{I_a}{2}[1-\sin 2\theta \sin\delta]$
$3\pi/4$	$\pi/4$	$\pi/4$	$I_4 = I_b + \frac{I_a}{2}[1+\cos 2\theta \sin\delta]$
$\pi/4$	0	0	$I_5 = I_b + \frac{I_a}{2}[1+\sin 2\theta \sin\delta]$
$\pi/4$	$3\pi/4$	$\pi/4$	$I_6 = I_b + \frac{I_a}{2}[1-\cos 2\theta \sin\delta]$

Using the equations listed in Table 3.2, the isoclinic parameter is obtained as

$$\theta_c = \frac{1}{2}\tan^{-1}\left(\frac{I_5 - I_3}{I_4 - I_6}\right) = \frac{1}{2}\tan^{-1}\left(\frac{I_a \sin\delta \sin 2\theta}{I_a \sin\delta \cos 2\theta}\right) \quad \text{for } \sin\delta \neq 0 \tag{3.14}$$

use of atan() function is recommended for the solution of above equation.The experimentally recorded images are shown in Fig. 3.18

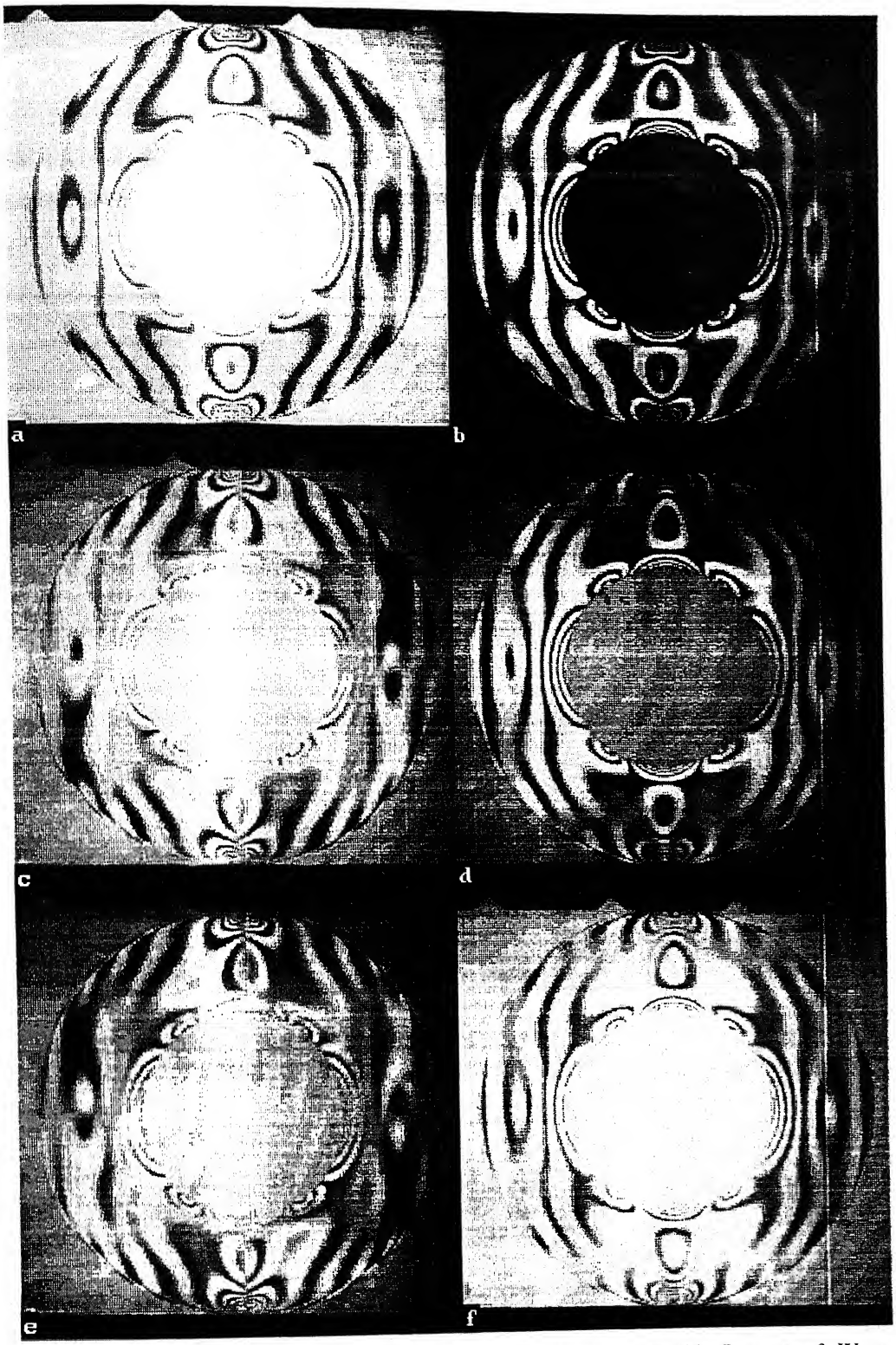

Fig 3.17 Sequence of six images recorded experimentally for the method by Patterson & Wang, as per the sequence given in Table 3.1 for the ring under diametral compression (load 503 N, dia. 80 mm, thickness 5.05 mm, F_σ = 11.2329 N/mm/fringe)

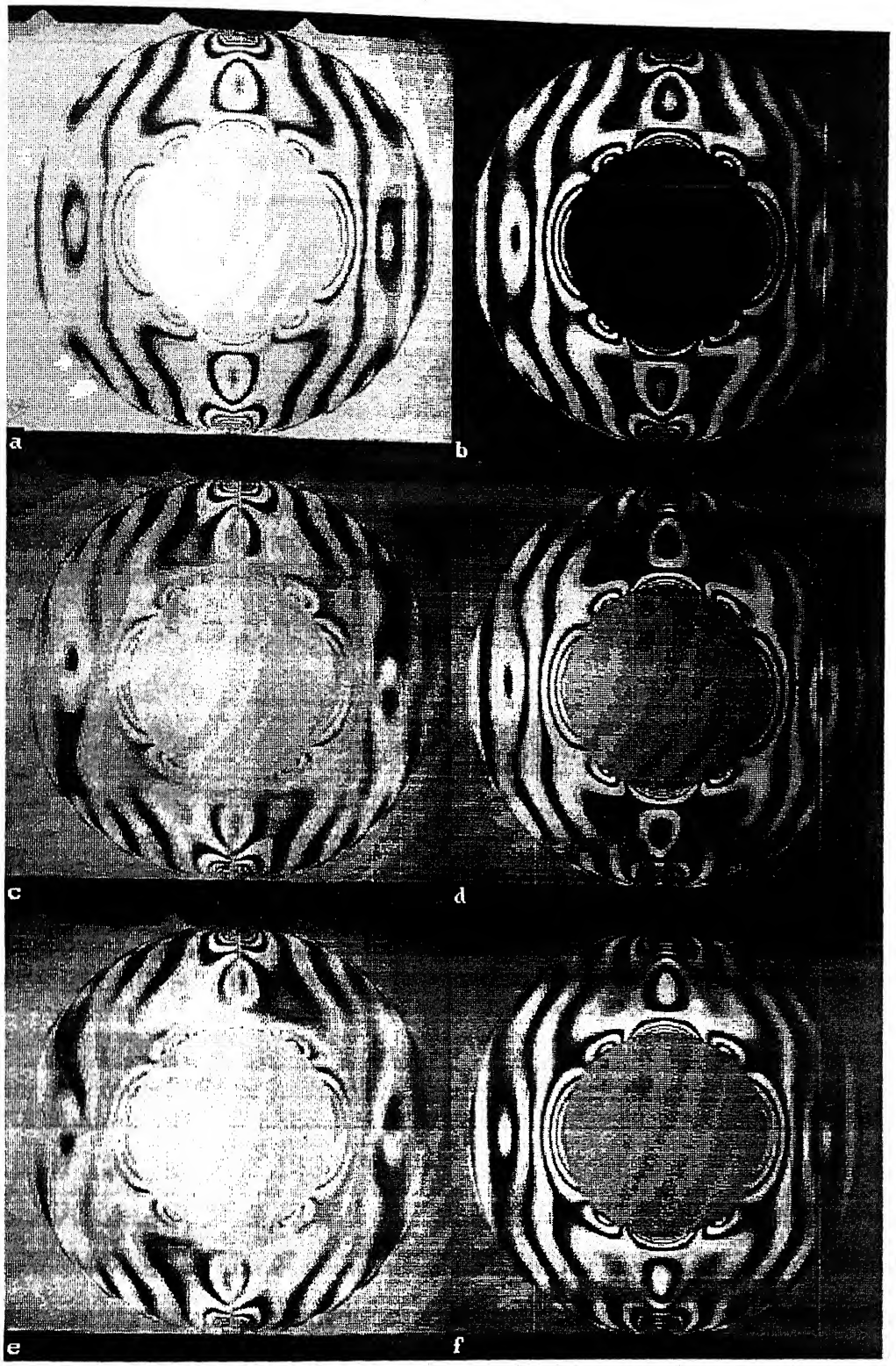

Fig 3.18 Sequence of six images recorded experimentally for the method by Ajovalasit et al. as per the sequence given in Table 3.2 for the ring under diametral compression (load 503 N, dia. 80 mm, thickness 5.05 mm, F_σ = 11.2329 N/mm/fringe)

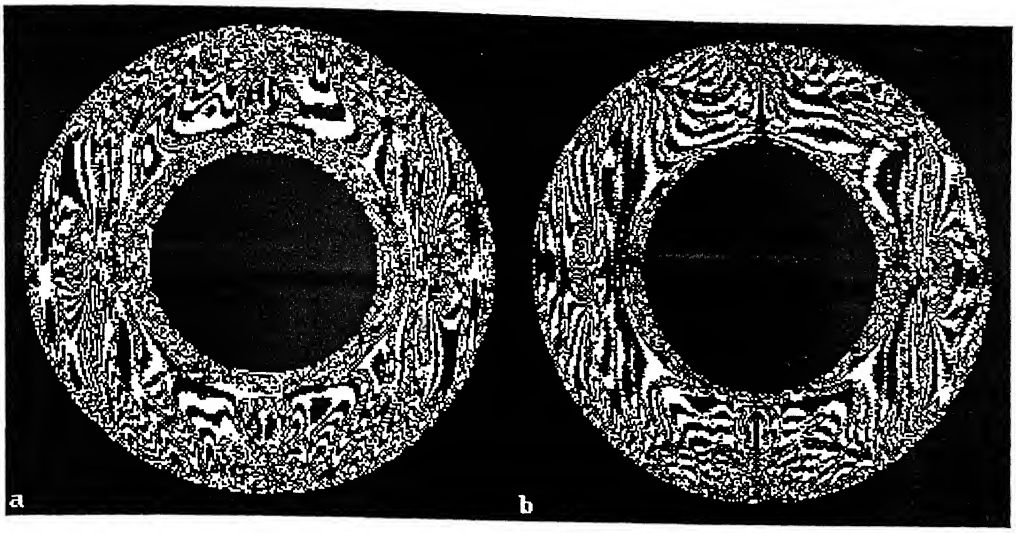

Fig 3.19 Isoclinic plots for the experimentally recorded images of ring under diametral compression **a** by the method of Patterson & Wang **b** by the method of Ajovalasit et al.

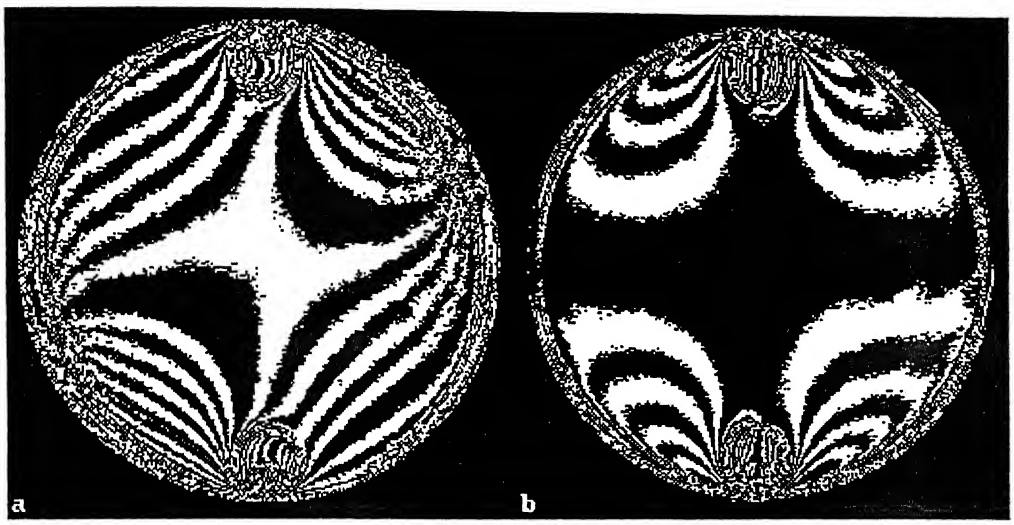

Fig 3.20 Isoclinic plots for the experimentally recorded images of disk under diametral compression for a low load (load 84 N, Dia. 60 mm, thickness 5.05 mm, F_σ= 11.2329 N/mm/fringe) **a** by the method of Patterson & Wang **b** by the method of Ajovalasit et al.

Figures 3.19 a & b show the isoclinic plot for ring from Patterson & Wang and Ajovalasit et. al. respectively. The plots show that the isoclinics are discontinuous. In some areas they are very poor. Such data is not useful for further analysis. Figure 3.20 shows the isoclinic plots obtained for a problem of disk at low load. Here the isoclinics are good as compared to the isoclinics obtained at higher loads. Thus comparatively better results can be obtained by using a lower load. But this may not possible for every problem, particularly for a slice cut from a stress frozen disk. Hence, study was carried out in plane polariscope to evaluate the isoclinics at higher loads.

3.5 Intensity of Light Transmitted for a Generic Arrangement of a Plane Polariscope

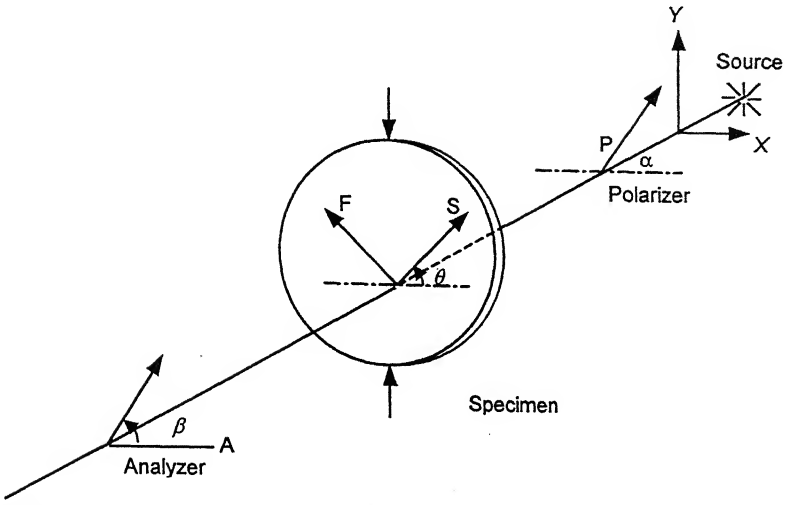

Fig. 3.21. Generic arrangement of a plane polariscope to employ phase shifting methodology

Figure 3.21 shows a photoelastic specimen kept in a plane polariscope with the polarizer and the analyser kept at arbitrary angles of α and β respectively. Using Jones calculus, the components of light vector along the analyser axis and perpendicular to the analyser axis are obtained as

$$\begin{Bmatrix} E_x \\ E_y \end{Bmatrix} = \begin{bmatrix} \cos\beta & \sin\beta \\ -\sin\beta & \cos\beta \end{bmatrix} \begin{bmatrix} \cos\frac{\delta}{2} - i\sin\frac{\delta}{2}\cos 2\theta & -i\sin\frac{\delta}{2}\sin 2\theta \\ -i\sin\frac{\delta}{2}\sin 2\theta & \cos\frac{\delta}{2} + i\sin\frac{\delta}{2}\cos 2\theta \end{bmatrix} \times \begin{Bmatrix} \cos\alpha \\ \sin\alpha \end{Bmatrix} k e^{i\omega t} \quad (3.15)$$

the intensity of light transmitted I_p (the subscript 'p' denotes that the incident light is plane polarised) is obtained as

$$I_p = I_a\left[\cos^2\frac{\delta}{2}\cos^2(\beta-\alpha) + \sin^2\frac{\delta}{2}\cos^2(\beta+\alpha-2\theta)\right] \quad (3.16)$$

where I_a accounts for the amplitude of incident light vector and the proportionality constant. It is interesting to note that Eq. (3.14) is not altered when the model slow axis orientation is changed from θ to $\theta + \pi/2$.

CENTRAL LIBRARY
I. I. T., KANPUR
A 130863

3.6 Phase Shifting Techniques Based on Plane Polariscope

Similar to the PST in circular polariscope, different algorithms are developed in plane polariscope also. Here a comparative study of some of the main algorithms in plane polariscopes is presented. The algorithms considered in plane polariscope are.

1 Ramesh and Mangal
2 Brown and Sullivan
3 Chen and Lin
4 Dupre et al.
5 Sarma et al.
6 Kihara

In the plane polariscope methods considered, the methods of Brown & sullivan and Chen & Lin are actually called as polarization stepping methods while the remaining methods are called as phase shifting methods. This study is done under similar conditions to obtain a comparative statement. This comparison is done for the evaluation of isoclinic parameter only. Initially each algorithm is introduced with respect to the optical arrangement and the equation for isoclinic parameter. Experimentally recorded images are shown for each optical arrangement in all the algorithms. Finally a comparative study of results obtained is done.

3.6.1 Algorithm by Ramesh and Mangal

In this, the polarizer and analyzer are kept at arbitrary positions. The intensity of light transmitted is given by Eq. (3.16). If the term I_b is added to account for stray light/background illumination, one gets

$$I_i = I_b + I_a\left[\cos^2\frac{\delta}{2}\cos^2(\beta_i-\alpha_i)+\sin^2\frac{\delta}{2}\cos^2(\beta_i+\alpha_i-2\theta)\right] \qquad (3.17)$$

If one takes all possible combinations of α and β in steps of $\pi/4$, then only six intensity equations turn out to be unique. The arrangement suggested by Ramesh and Mangal [1] is given in Table 3.3.

Table 3.3. Table showing the intensity equations for different orientations of the polarizer and analyzer.

α	β	Intensity equation
0	$\pi/2$	$I_1 = I_b + I_a \sin^2\frac{\delta}{2}\sin^2 2\theta$
$\pi/4$	$\pi/2$	$I_2 = I_b + \frac{I_a}{2}\left[1-\sin^2\frac{\delta}{2}\sin 4\theta\right]$
0	$\pi/4$	$I_3 = I_b + \frac{I_a}{2}\left[1+\sin^2\frac{\delta}{2}\sin 4\theta\right]$
$\pi/4$	$3\pi/4$	$I_4 = I_b + I_a \sin^2\frac{\delta}{2}\cos^2 2\theta$
$\pi/4$	$\pi/4$	$I_5 = I_b + I_a\left[\cos^2\frac{\delta}{2}+\sin^2\frac{\delta}{2}\sin^2 2\theta\right]$
0	0	$I_6 = I_b + I_a\left[\cos^2\frac{\delta}{2}+\sin^2\frac{\delta}{2}\cos^2 2\theta\right]$

From Table 3.3, using only the first four intensity equations, the isoclinic parameter is calculated as,

$$\theta_c = \frac{1}{4}\tan^{-1}\left(\frac{I_3 - I_2}{I_4 - I_1}\right) = \frac{1}{4}\tan^{-1}\left(\frac{I_a \sin^2\frac{\delta}{2}\sin 4\theta}{I_a \sin^2\frac{\delta}{2}\cos 4\theta}\right) \quad \text{for } \sin^2\frac{\delta}{2} \neq 0 \qquad (3.18)$$

Use of atan2 function is recommended for evaluating θ_c from Eq. (3.18). Figure 3.22 shows the experimentally recorded images for the ring.

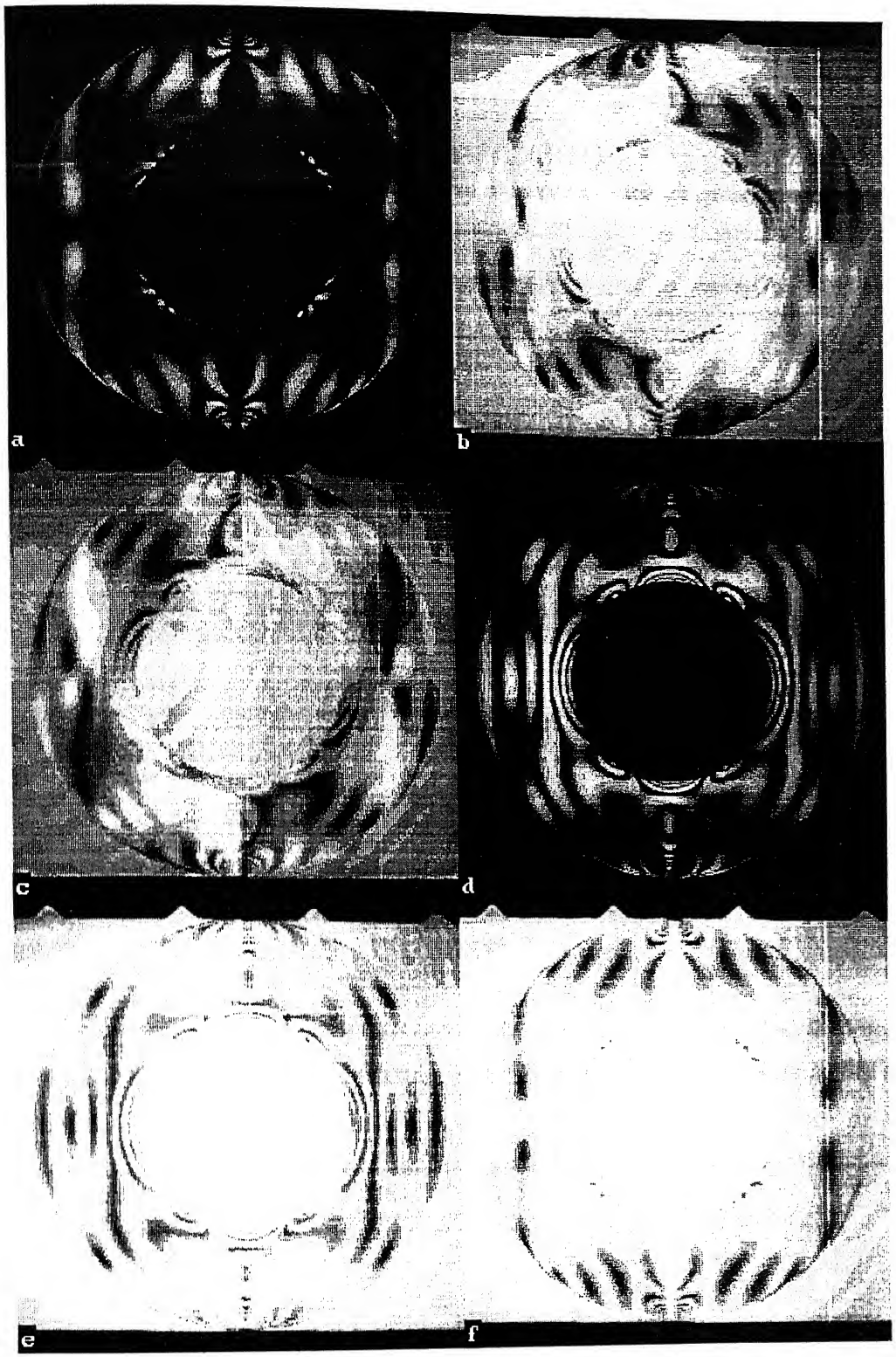

Fig 3.22 Sequence of six images recorded experimentally for the method by Ramesh & Mangal, as per the sequence given in Table 3.3 for the ring under diametral compression (load 503 N, Dia. 80 mm, thickness 5.05 mm, F_σ = 11.2329 N/mm/fringe)

3.6.2 Algorithm by Brown and Sullivan

In this polarizer and analyzer are kept crossed and four images are obtained at step of $\pi/8$ radians. The polarisation steps used by Brown and Sullivan [1] and the appropriate intensity equations are summarised in Table 3.4.

Table 3.4. Polariscope arrangements and intensity equations for polarization stepping schemes.

α	Intensity equation
Brown and Sullivan (Polarizer & Analyzer crossed; $\alpha=\beta+\pi/2$)	
0	$I_1 = I_b + I_a \sin^2\frac{\delta}{2}\sin^2 2\theta$
$\pi/8$	$I_2 = I_b + \frac{I_a}{2}\sin^2\frac{\delta}{2}(1-\sin 4\theta)$
$\pi/4$	$I_3 = I_b + I_a \sin^2\frac{\delta}{2}\cos^2 2\theta$
$3\pi/8$	$I_4 = I_b + \frac{I_a}{2}\sin^2\frac{\delta}{2}(1+\sin 4\theta)$

The isoclinic parameter is obtained as

$$\theta_c = \frac{1}{4}\tan^{-1}\left(\frac{I_4 - I_2}{I_3 - I_1}\right) = \frac{1}{4}\tan^{-1}\left(\frac{I_a \sin^2\frac{\delta}{2}\sin 4\theta}{I_a \sin^2\frac{\delta}{2}\cos 4\theta}\right) \quad \text{for } \sin^2\frac{\delta}{2} \neq 0 \qquad (3.19)$$

use of atan2() function is recommended for evaluating above equation. Figure 3.23 shows the xperimentally recorded images for the ring.

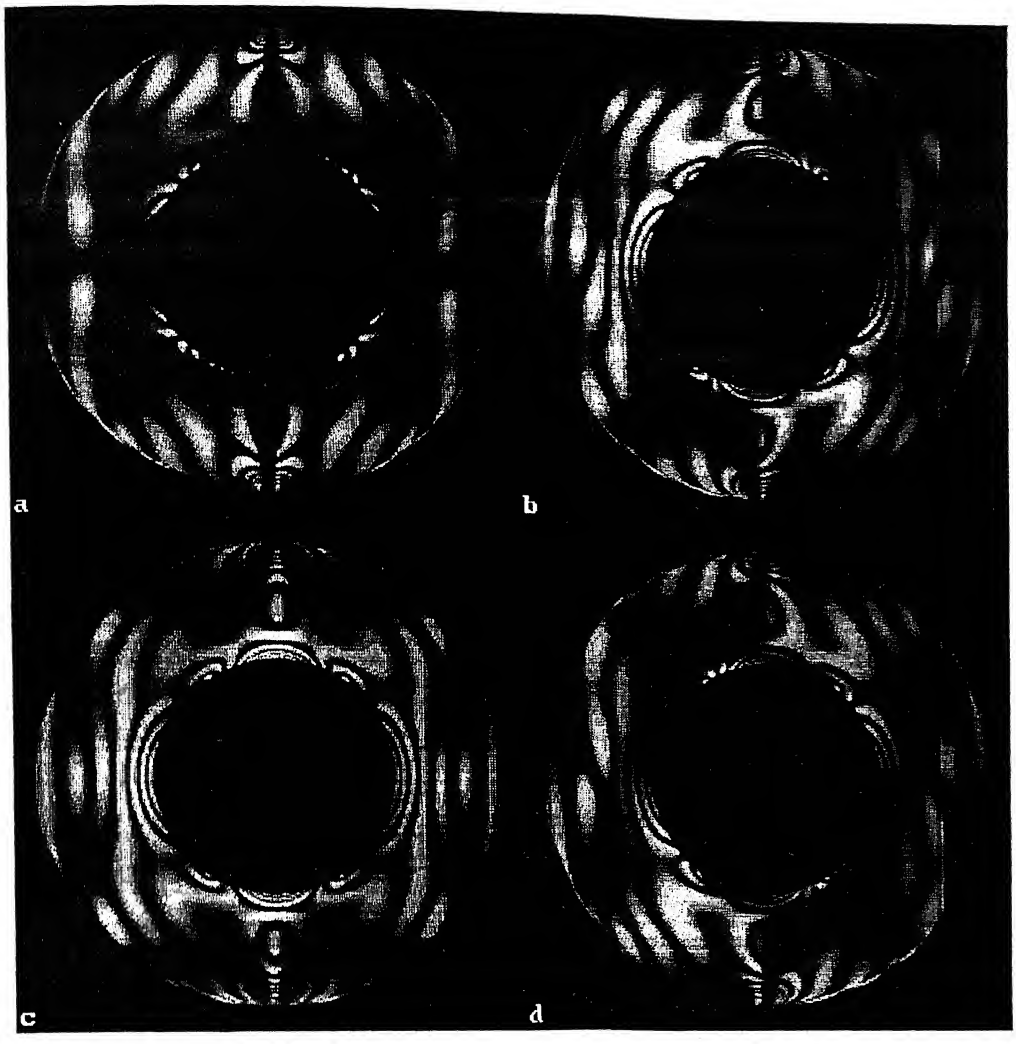

Fig 3.23 Sequence of four images recorded experimentally for the method by Brown & Sullivan, as per the sequence given in Table 3.4 for the ring under diametral compression (load 503 N, dia. 80 mm, thickness 5.05 mm, F_σ = 11.2329 N/mm/fringe)

3.6.3 Algorithm by Chen and Lin

Chen and Lin [1] proposed another polarisation-stepped scheme. In this initially three bright field images in plane polariscope arrangement were obtained. From these bright field images, dark-field images are constructed using trigonometric identity and the concept of image division. For performing image division, the intensity corresponding to unloaded images are also to be recorded. Appropriate intensity equations are summarised in Table 3.5.

Table 3.5. Polariscope arrangements and intensity equations for polarization stepping schemes.

Chen & Lin (Polarizer & Analyzer parallel; $\alpha=\beta$)	
0	$I_1 = I_a\left[1-\sin^2 2\theta \sin^2\frac{\delta}{2}\right]$
$\pi/8$	$I_2 = I_a\left[1-\frac{1}{2}(\sin 2\theta - \cos 2\theta)^2 \sin^2\frac{\delta}{2}\right]$
$\pi/4$	$I_3 = I_a\left[1-\cos^2 2\theta \sin^2\frac{\delta}{2}\right]$

The intensity equation corresponding to dark-field is obtained by

$$I_i' = 1-\frac{I_i}{I_{ui}} \tag{3.20}$$

where, I_{ui} is the intensity recorded using an unloaded model. The isoclinic parameter is then obtained as

$$\theta_c = \frac{1}{4}\tan^{-1}\left(\frac{I_1+I_3-2I_2}{I_3-I_1}\right) \tag{3.21}$$

Use of atan2() function is recommended to evaluate θ_c from the above equation. Figure 3.24 shows the experimentally recorded images for the ring for this arrangement.

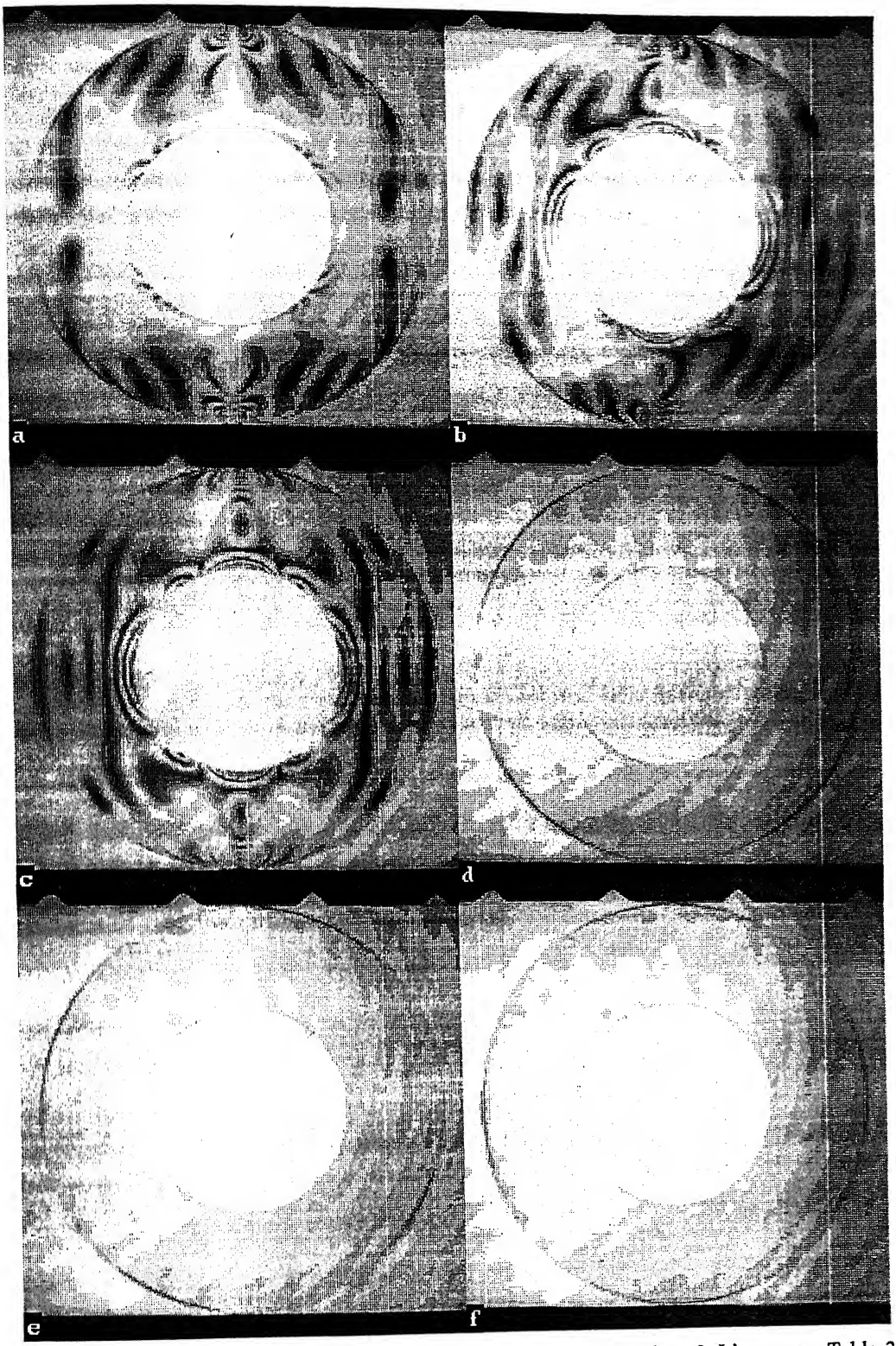

Fig 3.24 Six images recorded experimentally for the method by Chen & Lin, as per Table 3.5 for the ring under diametral compression (load 503 N, dia. 80 mm, thickness 5.05 mm, F_σ = 11.2329 N/mm/fringe)

The construction of normalized dark field images from the bright field images is an important step in this method. Theoretically I_a, is constant at 255 all over the domain, and this is always greater than or equal to the loaded bright field intensity in the domain. Hence theoretically, generation of dark field images is good. Experimentally this is not the case, at some places in the domain the unloaded model intensity becomes less than the loaded model. This happens mainly because of varying intensity of light source with time. So in the image division the ratio of loaded intensity to unloaded one becomes greater than one. Thus the value of I'_i in Eq. 3.20 becomes –ve at those points in the domain and it is not possible to get the correct normalized dark field images. This is rectified by introducing an adjustment factor k, so Eq. 3.18 is modified as

$$I'_i = 1 - k\left(\frac{I_i}{I_{ui}}\right) \tag{3.22}$$

typically the value of k for the experimental set up used lies in the range 0.5 to 0.7 but it may vary in different experimental set up. Theoretically generated normalized dark field images are shown in Fig. 3.25. Figure 3.26 shows the experimentally generated dark field images without any adjustment (k = 1) and Fig. 3.27 shows the experimentally generated dark field images with adjustment (k = 0.65) for the experimentally recorded images of ring under diametral compression.

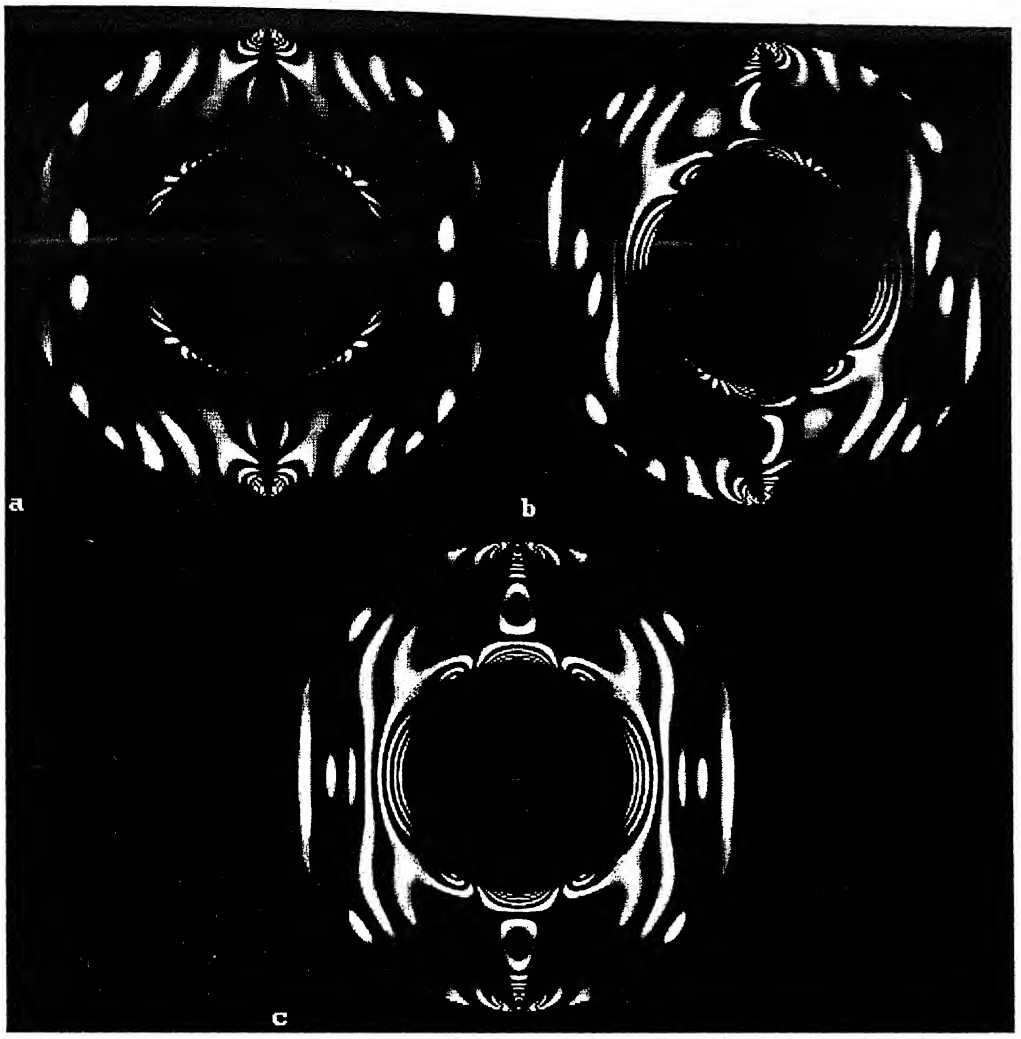

Fig 3.25 Normalized dark field images generated by Eq. (3.20) using theoretically generated images as per the sequence given in Table 3.5. **a** for 0 deg. **b** for 22.5 deg **c** for 45 deg

Fig 3.26 Normalized dark field images generated without adjustment (Eq. 3.20) using experimentally recorded images as per the sequence given in Table 3.5. **a** for 0 deg. **b** for 22.5 deg **c** for 45 deg

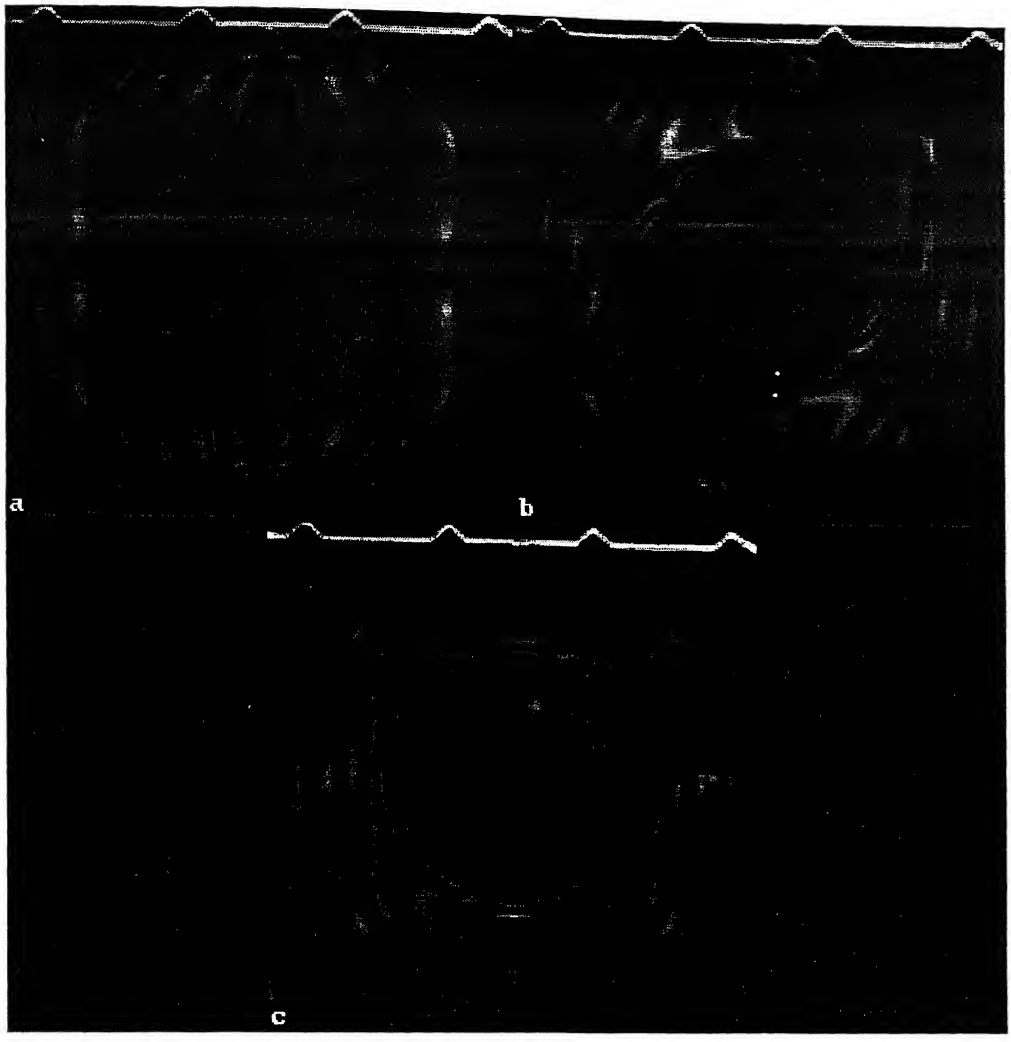

Fig 3.27 Normalized dark field images generated with adjustment (Eq. 3.22, k = 0.60) using experimentally recorded images as per the sequence given in Table 3.5. **a** for 0 deg. **b** for 22.5 deg **c** for 45 deg

3.6.4 Algorithm by Dupre et al.

Arrangements suggested by Dupre et. al.[1] are summarised in table 3.6.

Table 3.6. Optical arrangements for Dupre et al.

α	η	β	Intensity equation
0	-	0	$I_1 = I_a$
0	-	0	$I_2 = I_a\left[\cos^2\frac{\delta}{2} + \sin^2\frac{\delta}{2}\cos^2 2\theta\right]$
0	-	$\pi/4$	$I_3 = \frac{I_a}{2}\left[1 + \sin^2\frac{\delta}{2}\sin 4\theta\right]$
$\pi/4$	-	$\pi/4$	$I_4 = I_a\left[\cos^2\frac{\delta}{2} + \sin^2\frac{\delta}{2}\sin^2 2\theta\right]$
0	$3\pi/4$	0	$I_5 = \frac{I_a}{2}[1 + \sin 2\theta \sin\delta]$

The isoclinic parameter is calculated as

$$\theta_c = \frac{1}{4}\tan^{-1}\left(\frac{2I_3 - I_1}{I_2 - I_4}\right) = \frac{1}{4}\tan^{-1}\left(\frac{\sin^2\frac{\delta}{2}\sin 2\theta}{\sin^2\frac{\delta}{2}\cos 2\theta}\right) \quad \text{for } \sin^2\frac{\delta}{2} \neq 0 \qquad (3.23)$$

use of atan2() function is recommended to evaluate this equation. Figure 3.28 shows a set of experimentally recorded images.

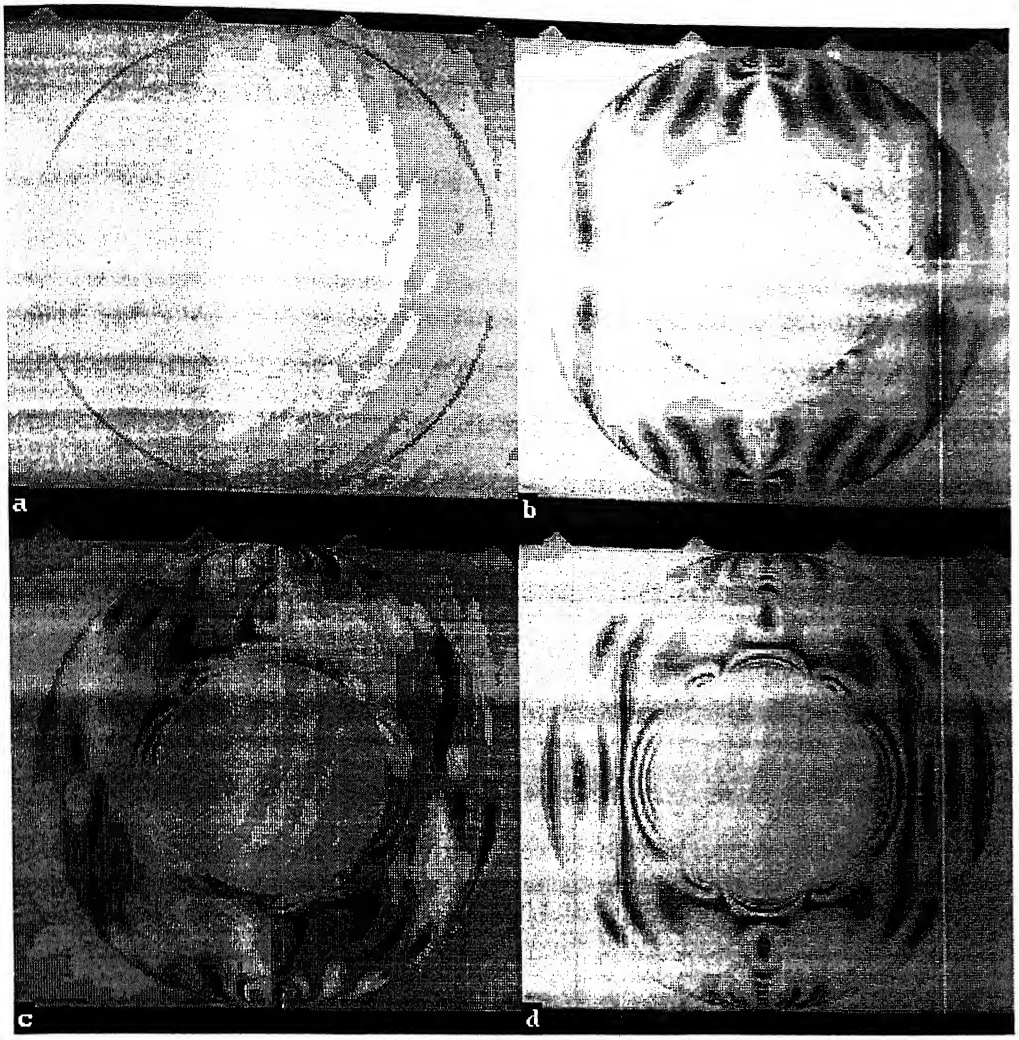

Fig 3.28 Sequence of Four images recorded experimentally for the method by Dupre et al, as given in Table 3.6 for the ring under diametral compression (load 503 N, dia. 80 mm, thickness 5.05 mm, F_σ = 11.2329 N/mm/fringe)

3.6.5 Algorithm by Sarma et al.

Arrangements suggested by Sarma et al. [1] are summarised in Table 3.7.

Table 3.7. Optical arrangements for Sarma et al.

α	η	β	Intensity equation
$\pi/2$	-	$\pi/2$	$I_1 = I_a\left[\cos^2\frac{\delta}{2} + \sin^2\frac{\delta}{2}\cos^2 2\theta\right]$
$\pi/2$	-	0	$I_2 = I_a\left[\sin^2\frac{\delta}{2}\sin^2 2\theta\right]$
$\pi/2$	-	$\pi/4$	$I_3 = \frac{I_a}{2}\left[1 - \sin^2\frac{\delta}{2}\sin 4\theta\right]$

The expression for the determination of isoclinic parameter by Sarma et al. method is

$$\theta_c = \frac{1}{2}\tan^{-1}\left(\frac{2I_2}{I_1 + I_2 - 2I_3}\right) \tag{3.24}$$

Sarma et al. have not explicitly taken into account the effect of background /stray light intensity by introducing a parameter I_b in the intensity equation. Instead, they proposed that one has to capture an image of unstressed model in the polariscope when polarizer and analyzer are kept in crossed position. The intensity values of this image are to be subtracted from all other images before any processing is done. Use of atan() function is recommended in this case. Figure 3.29 shows the set of experimentally recorded images.

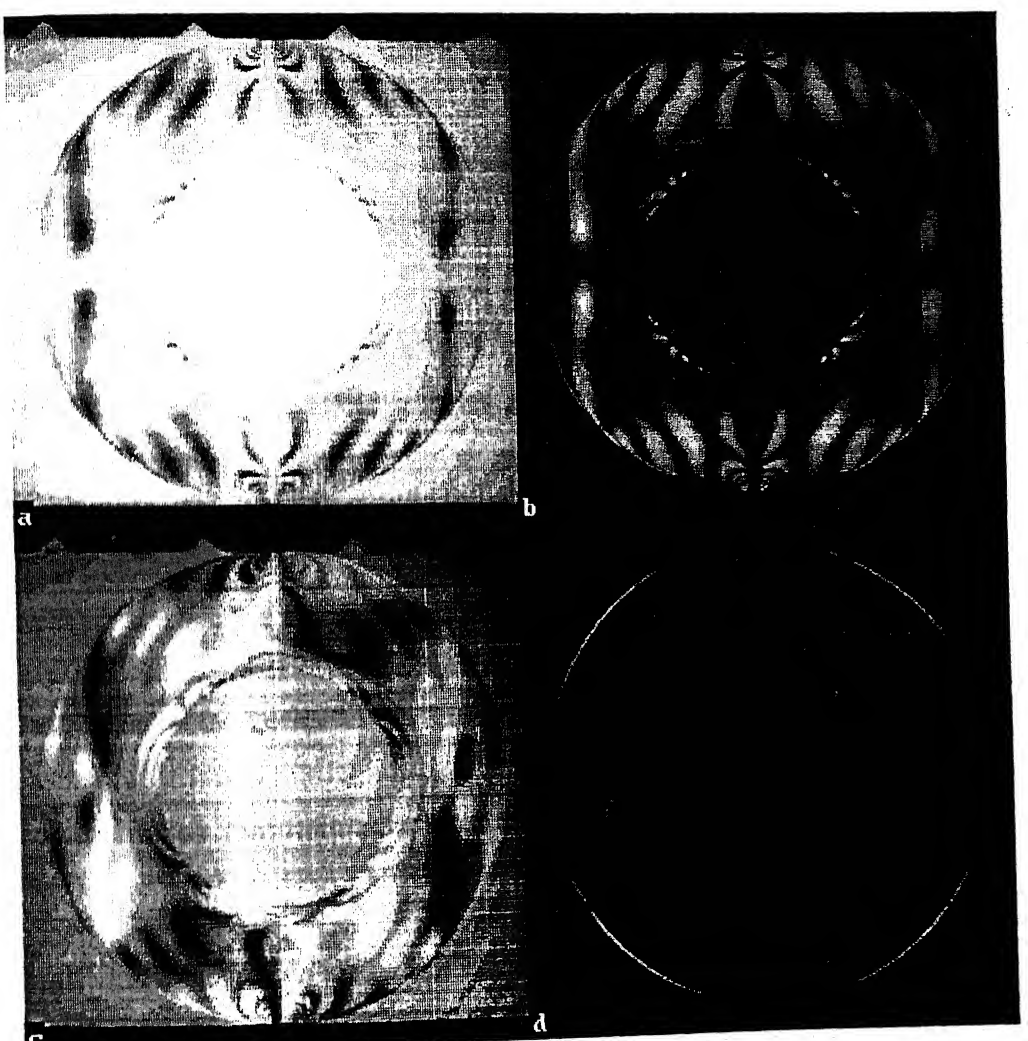

Fig 3.29 Sequence of Four images recorded experimentally for the method by Sarma et al, as given in Table 3.7 for the ring under diametral compression (load 503 N, dia. 80 mm, thickness 5.05 mm, F_σ = 11.2329 N/mm/fringe)

3.6.6 Algorithm by Kihara

Arrangements suggested by Kihara [1] are summarised in Table 3.8.

Table 3.8. Optical arrangements for Kihara.

Kihara			
0	$\pi/2$	$-\pi/4$	$I_1 = \frac{I_a}{2}[1+\sin\delta\sin 4\theta]$
0	$\pi/2$	$\pi/4$	$I_2 = \frac{I_a}{2}[1-\sin\delta\sin 2\theta]$
$-\pi/4$	$\pi/2$	$-\pi/4$	$I_3 = \frac{I_a}{2}[1+\sin\delta\cos 2\theta]$
$-\pi/4$	$\pi/2$	$\pi/4$	$I_4 = \frac{I_a}{2}[1-\sin\delta\cos 2\theta]$
0	$\pi/2$	0	$I_5 = I_a\left[\cos^2\frac{\delta}{2}+\sin^2\frac{\delta}{2}\cos^2 2\theta\right]$
0	$\pi/2$	$\pi/2$	$I_6 = I_a\left[\sin^2\frac{\delta}{2}\sin^2 2\theta\right]$
$-\pi/4$	$\pi/4$	$-\pi/4$	$I_7 = I_a\left[\cos^2\frac{\delta}{2}+\sin^2\frac{\delta}{2}\sin^2 2\theta\right]$
$-\pi/4$	$\pi/4$	$\pi/4$	$I_8 = I_a\left[\sin^2\frac{\delta}{2}\cos^2 2\theta\right]$

For the optical arrangement used by Kihara, the expressions for determining isoclinic and fractional retardation are

$$\theta_c = \frac{1}{2}\tan^{-1}\left(\frac{I_1 - I_2}{I_3 - I_4}\right) = \frac{1}{2}\tan^{-1}\left(\frac{\sin\delta\sin 2\theta}{\sin\delta\cos 2\theta}\right) \quad \text{for } \sin\delta \neq 0 \tag{3.25}$$

Use of atan() function is recommended to calculate theta from the above equation. Though the method proposed by Kihara is quite different, ultimately the method reduces to the one given by Patterson and Wang in view of the similarity in the intensity equations used for theta calculation. Figure 3.30 shows the set of experimentally recorded images.

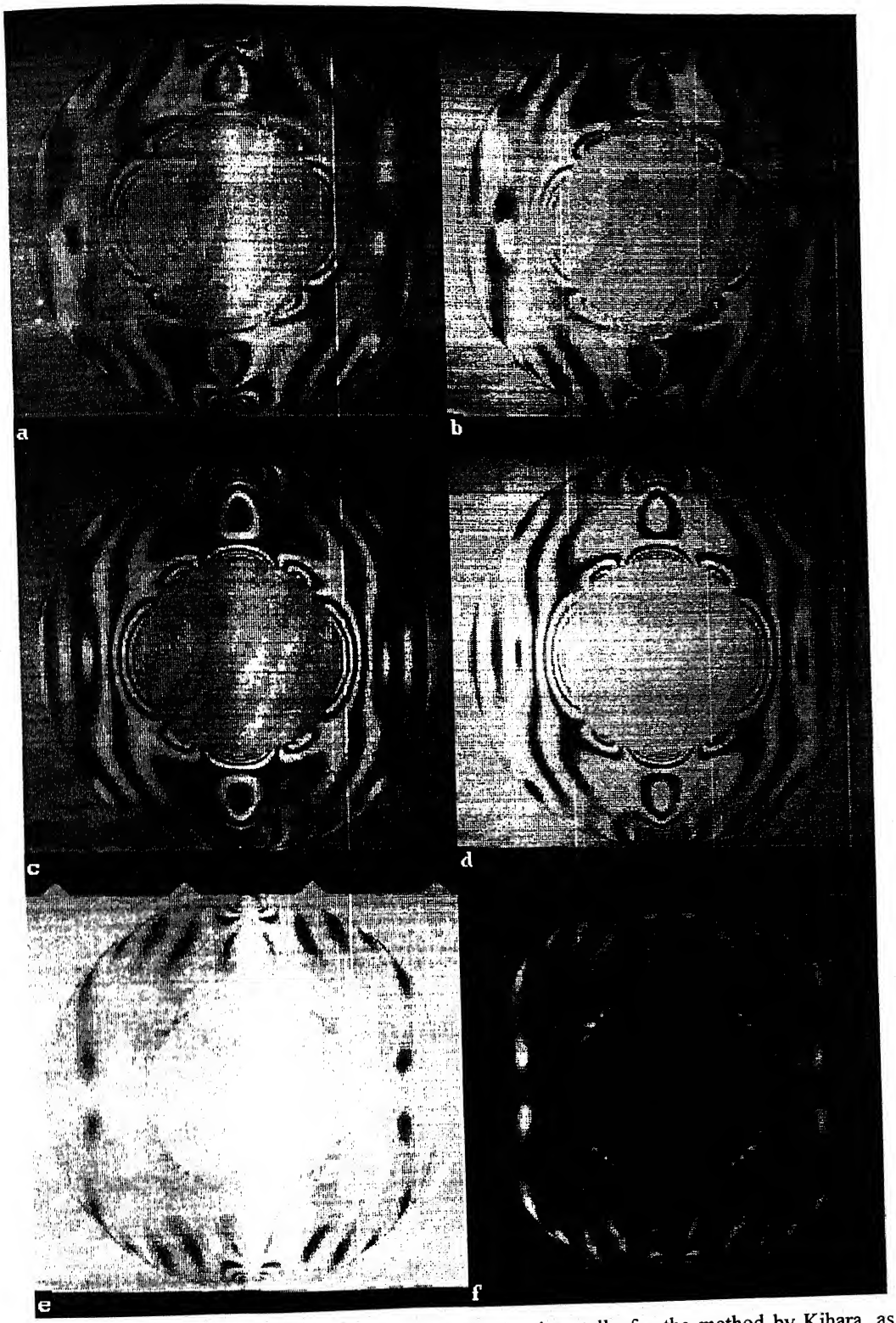

Fig 3.30 Sequence of first six images recorded experimentally for the method by Kihara, as given in Table 3.8 for the ring under diametral compression (load 503 N, dia. 80 mm, thickness 5.05 mm, F_σ = 11.2329 N/mm/fringe)

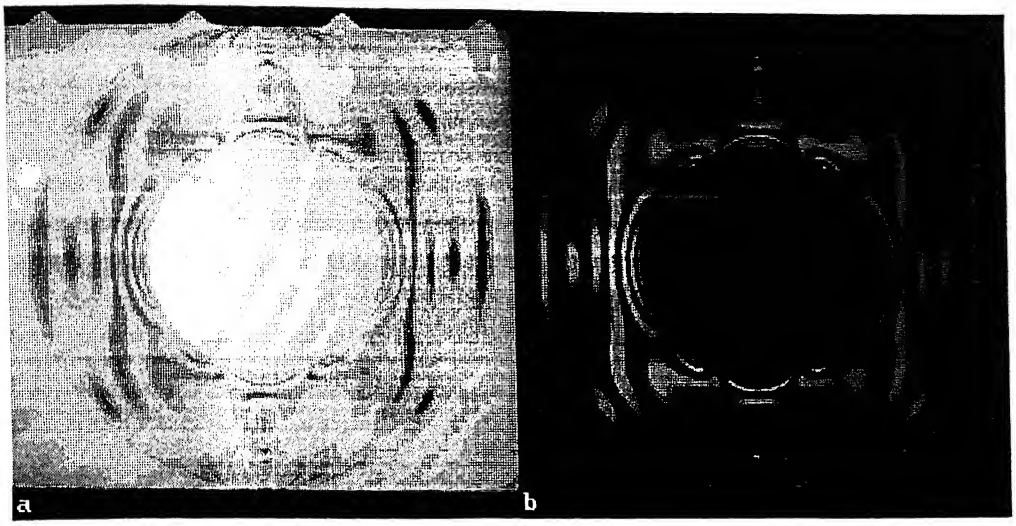

Fig 3.30 Sequence of last two images recorded experimentally for the method by Kihara, as given in Table 3.8 for the ring under diametral compression (load 503 N, dia. 80 mm, thickness 5.05 mm, F_σ = 11.2329 N/mm/fringe)

3.6.7 Comparison of Results obtained by Circular and Plane Polariscope Algorithms

Figures 3.31 & 3.32 show the isoclinics obtained by using theoretically generated images. Figure 3.31a & b shows the isoclinic plots obtained for Patterson & Wang and Ajovalasit et al. methods. Figure 3.31c & d shows the isoclinic plots obtained for Ramesh &Mangal and Brown & Sullivan. methods. Figure 3.31e & f shows the isoclinic plots obtained for Chen &Lin and Dupre et al. methods. Figure 3.32a & b shows the isoclinic plots obtained for Sarma et al. and Kihara. Methods. It is clear that all the algorithms give good results theoretically. But experimentally this is not the case. Figures 3.33 & 3.34 show the isoclinics obtained by using the experimentally recorded images. Figure 3.33a & b shows the isoclinic plots obtained for Patterson & Wang and Ajovalasit et al. methods. Figure 3.33c & d shows the isoclinic plots obtained for Ramesh &Mangal and Brown & Sullivan. methods. Figure 3.33e & f shows the isoclinic plots obtained for Chen &Lin without adjustment and Chen &Lin with adjustment. Figure 3.34a & b shows the isoclinic plots obtained for Dupre et al. and Sarma et al. methods and Fig. 3.34c shows the isoclinic plots obtained for Kihara's. method.

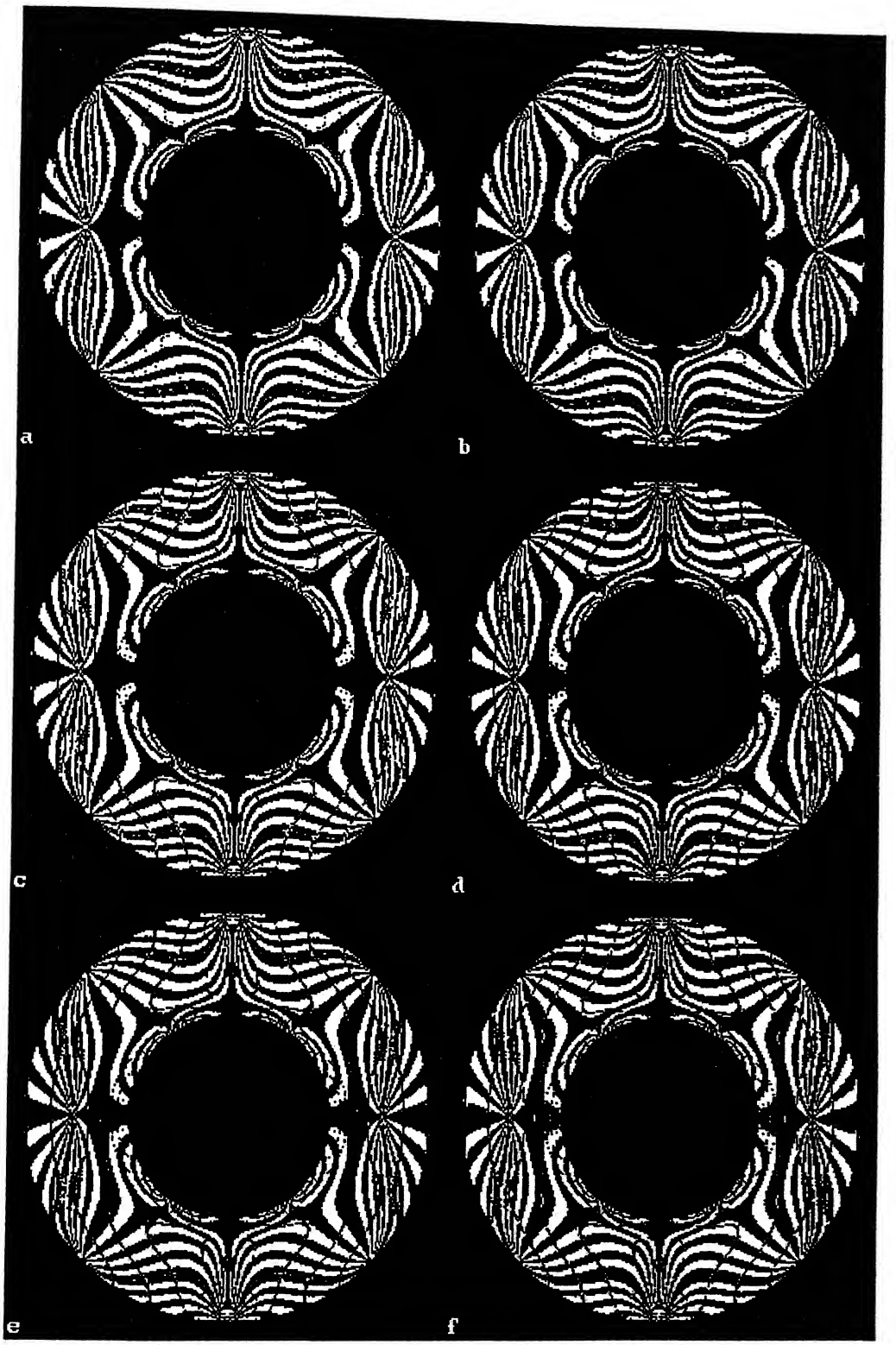

Fig 3.31 Isoclinic plots obtained for the theoretically generated images of ring under diametral compression. **a** by Patterson & Wang **b** by Ajovalasit et al. **c** by Ramesh & Mangal **d** by Brown & Sullivan **e** by Chen & Lin **f** by Dupre et al.

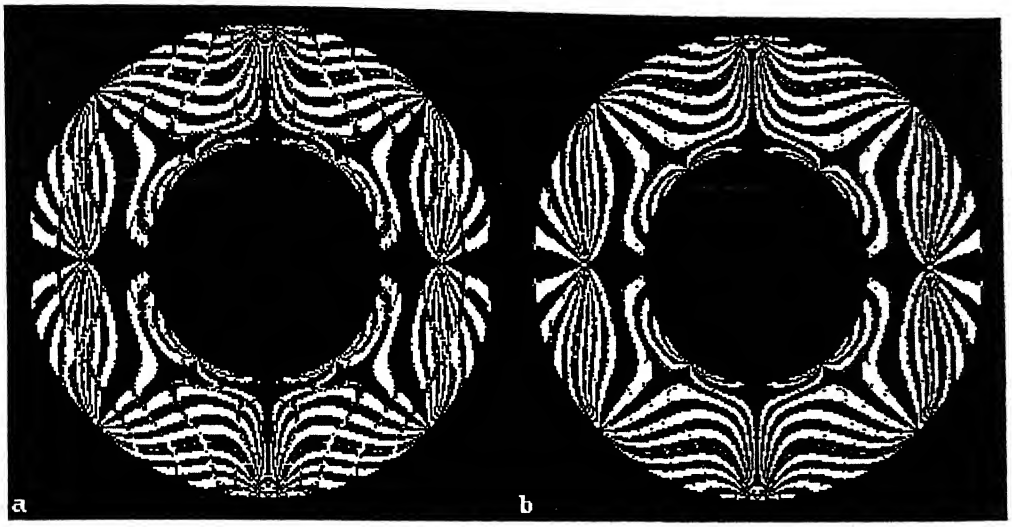

Fig 3.32 Isoclinic plots obtained for the theoretically generated images of ring under diametral compression. **a** by Sarma et al. **b** by Kihara

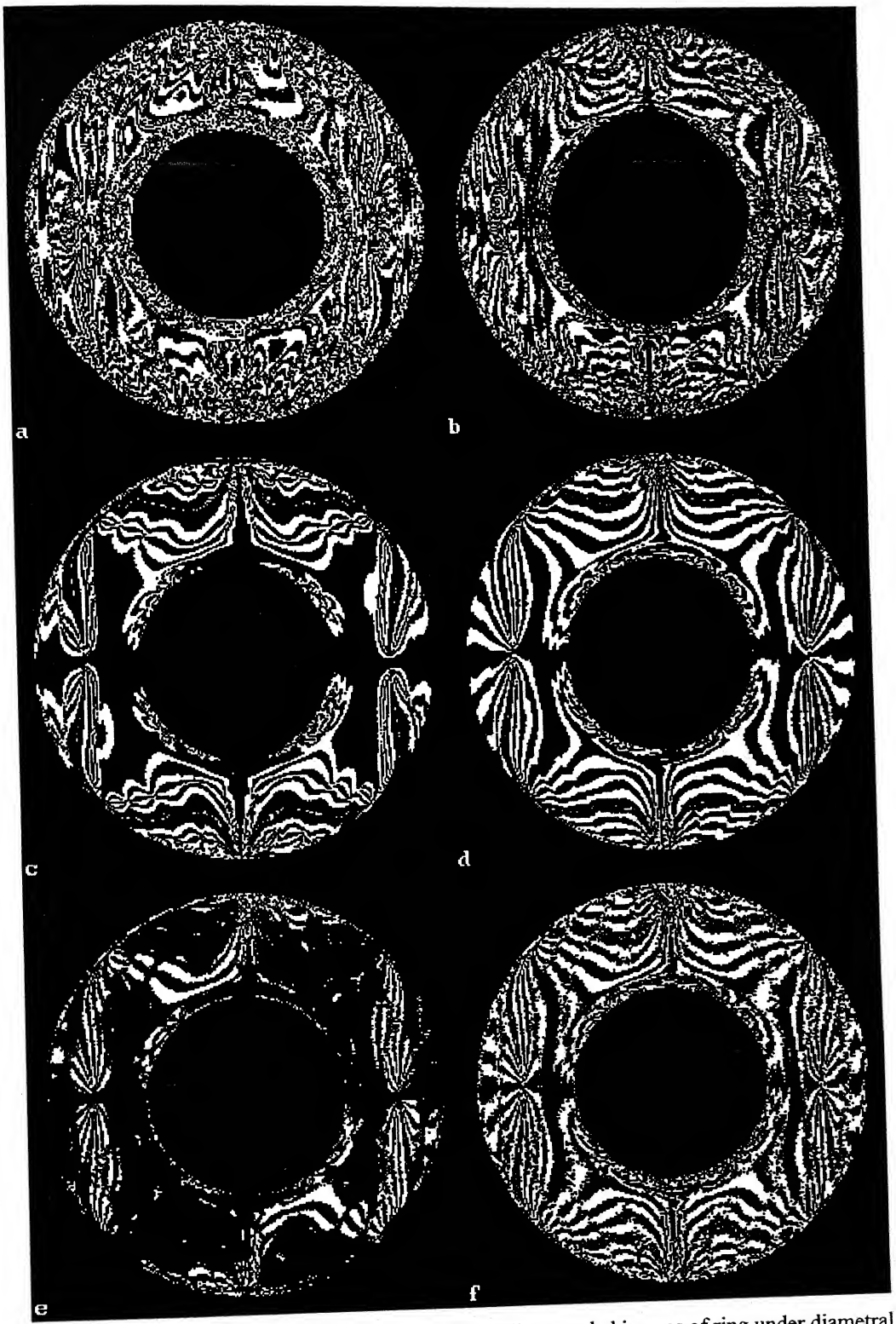

Fig 3.33 Isoclinic plots obtained for the experimentally recorded images of ring under diametral compression. **a** by Patterson & Wang **b** by Ajovalasit et al. **c** by Ramesh & Mangal **d** by Brown & Sullivan **e** by Chen & Lin (without adjustment) **f** by Chen & Lin (with adjustment)

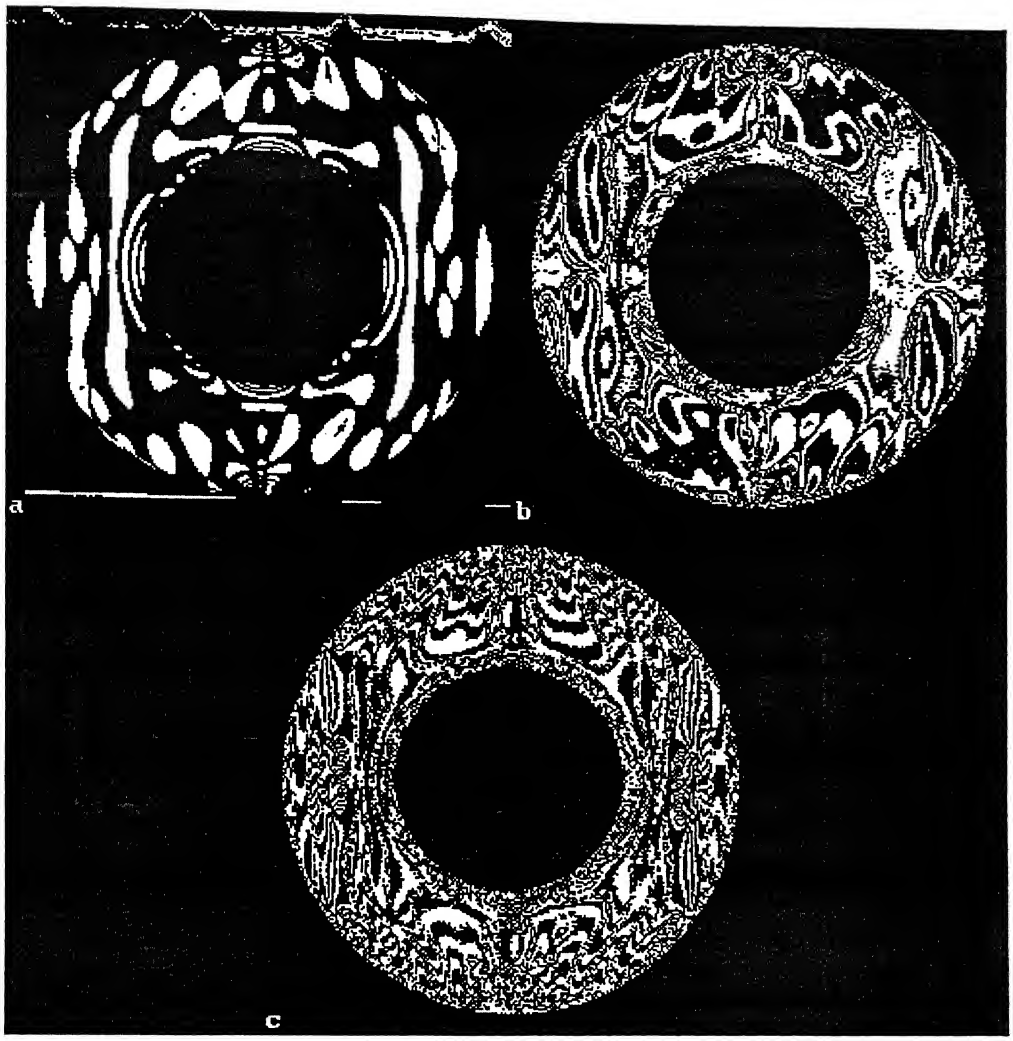

Fig 3.34 Isoclinic plots obtained for the experimentally recorded images of ring under diametral compression. **a** by Dupre et al. **b** by Sarma et al. **c** by Kihara

Figures 3.35 and 3.36 show graphs for the experimentally obtained data at lines y/R = 0.5 and y/R = 0.25 respectively. The experimentally calculated theta is compared with the theta calculated theoretically

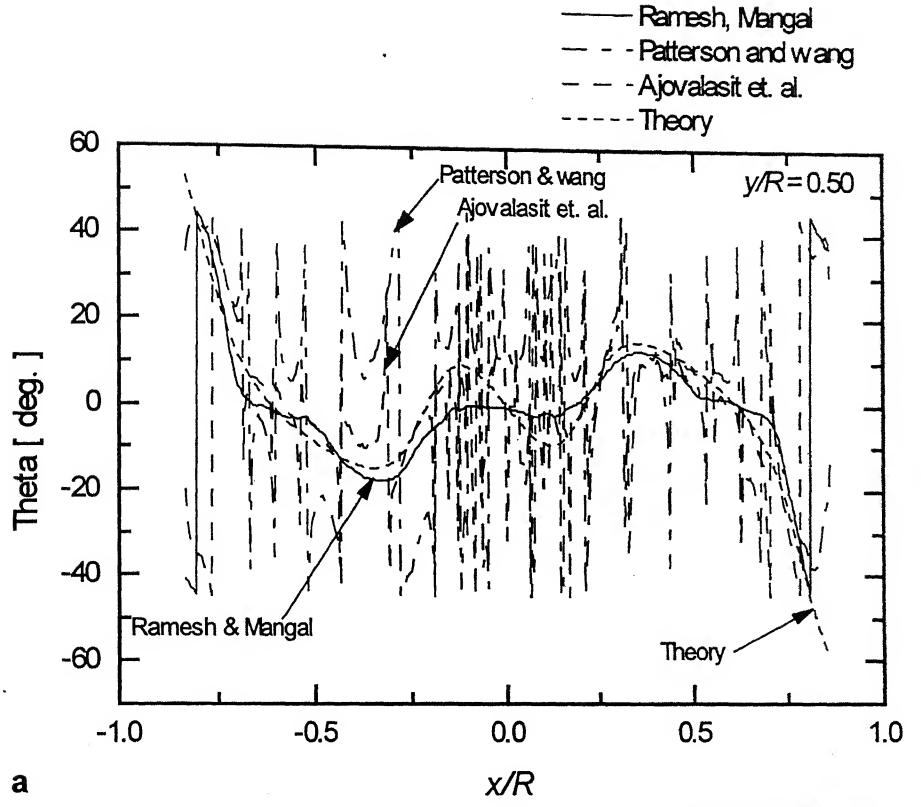

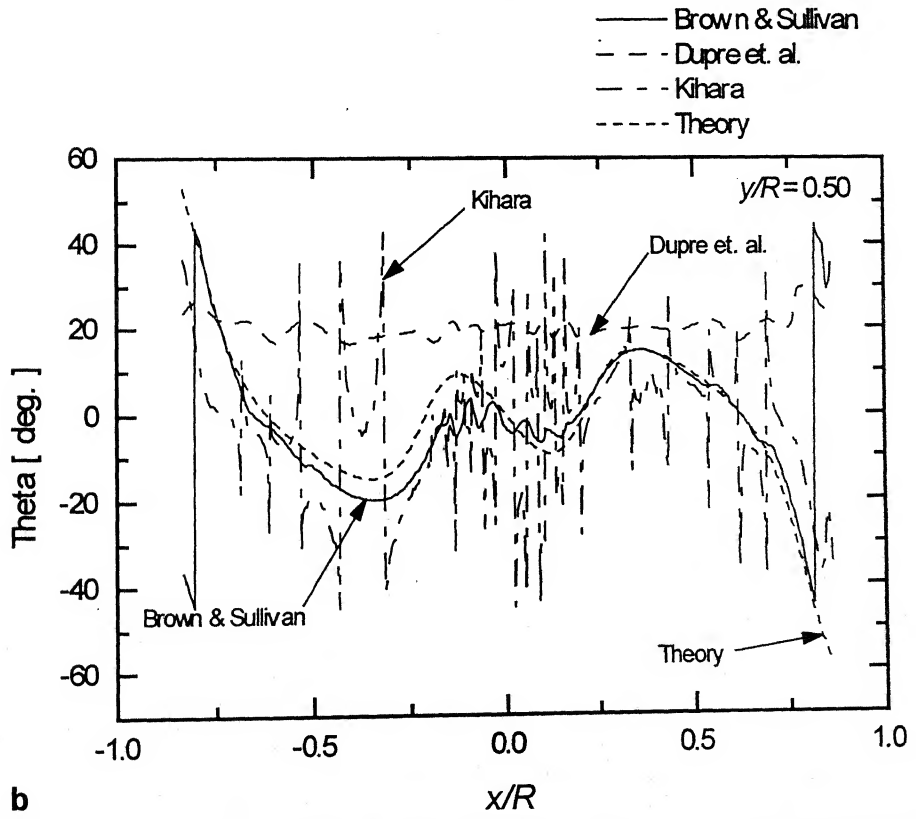

Fig. 3.35.Comparison of experimenatal theta with theoretical theta for line at y/R =0.50 **a** Ramesh & Mangal, Patterson & Wang, Ajovalasit et. al., & theory **b** Brown & Sullivan, Dupre et. al., Kihara, theory.

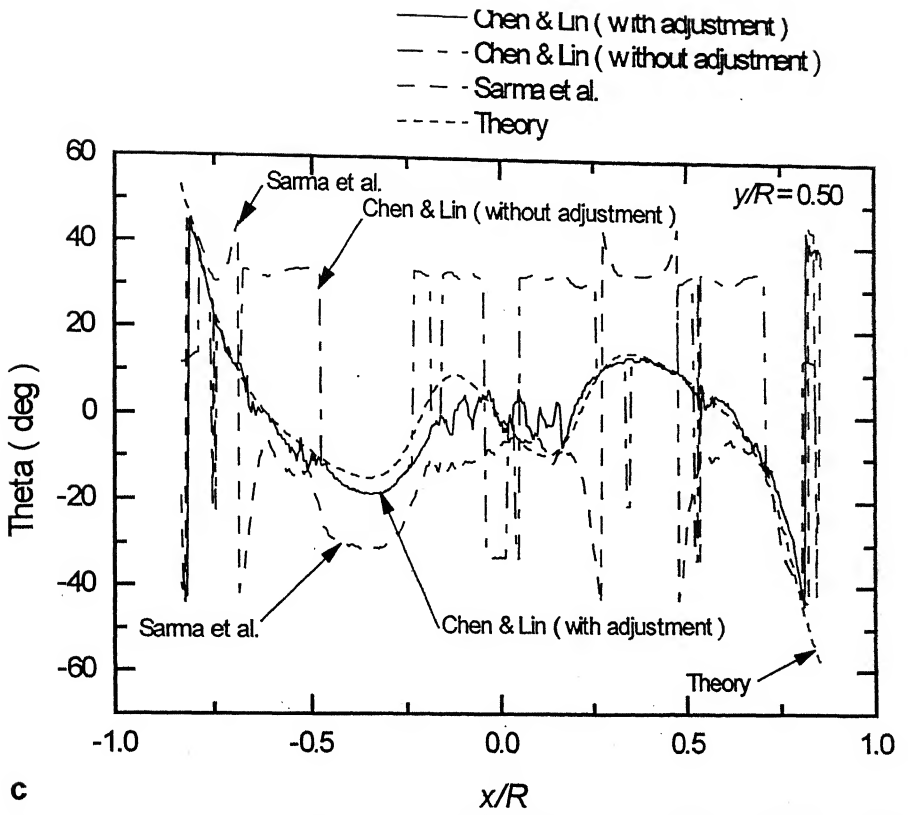

c

Fig. 3.35.c Comparison of Experimenatal theta with theoretical theta for line at y/R =0.50 for Chen & Lin, Sarma et. al. Theory

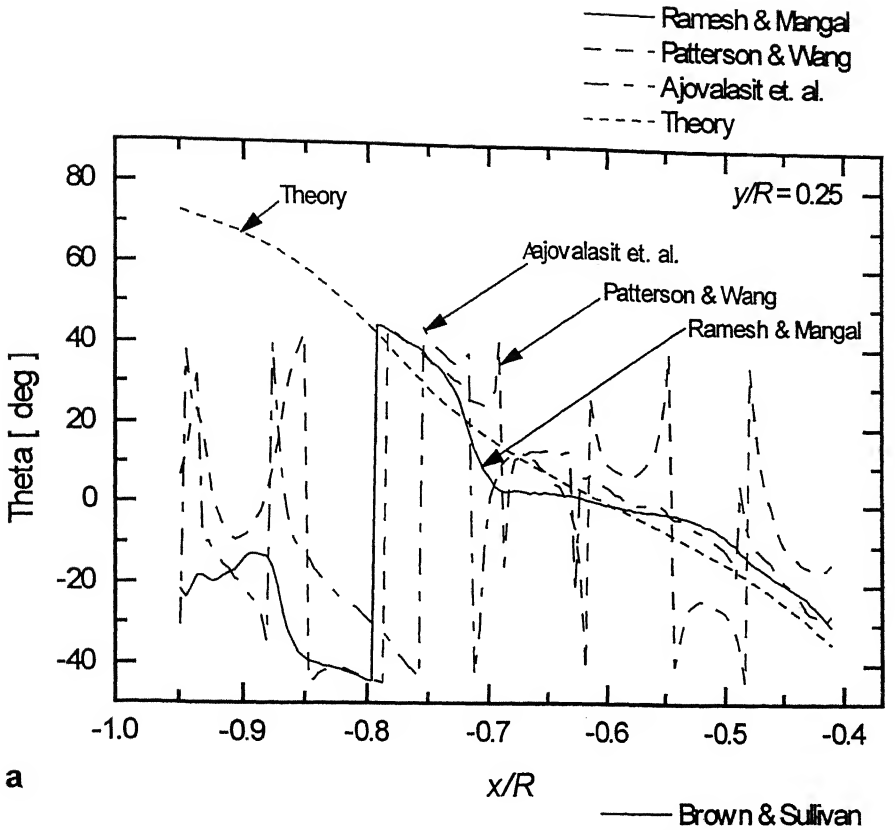

a

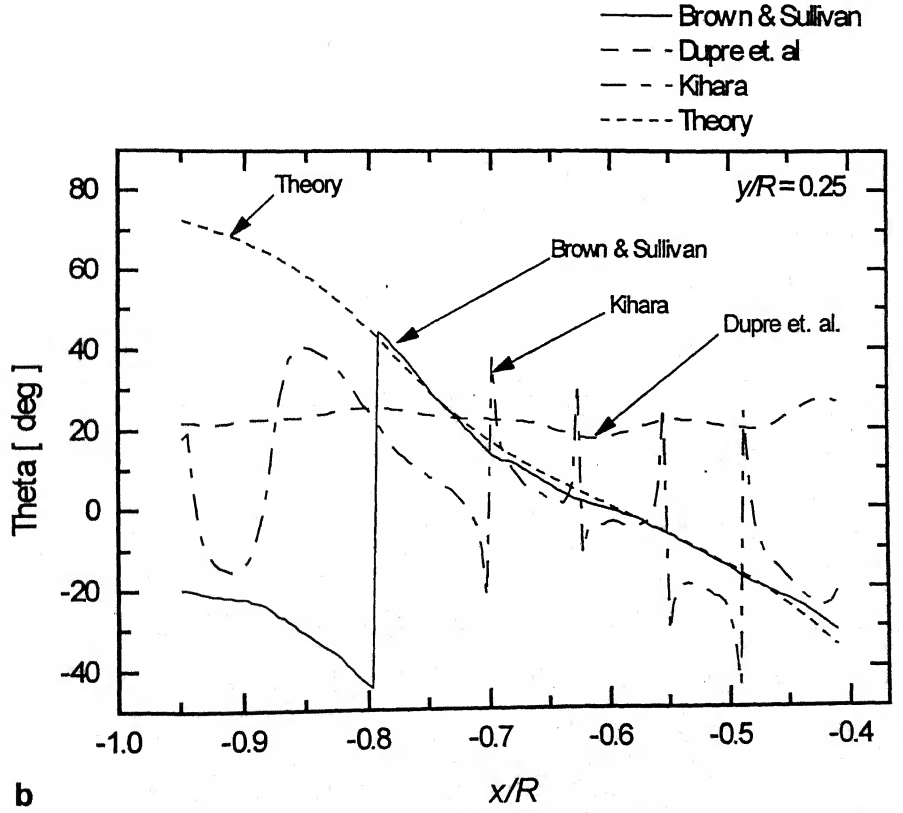

b

Fig. 3.36. Comparison of Experimenatal theta with theoretical theta for line at $y/R = 0.25$ **a** Ramesh & Mangal, Patterson & Wang, Ajovalasit et. al., Theory **b** Brown & Sullivan, Dupre et. al., Kihara, Theory.

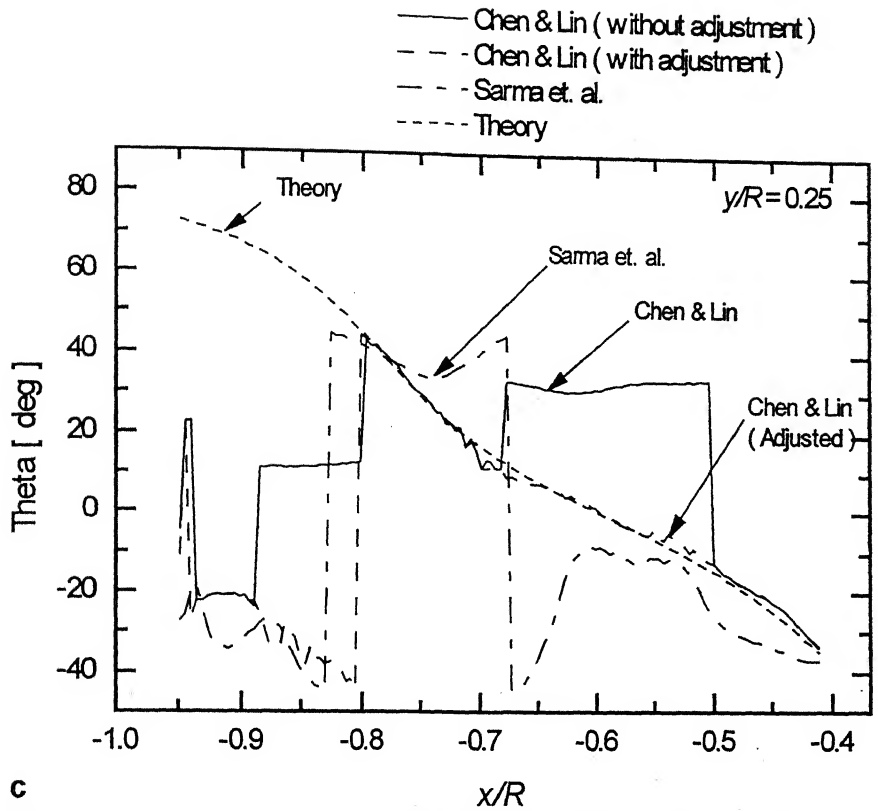

c

Fig. 3.36.c Comparison of Experimenatal theta with theoretical theta for line at y/R =0.25 for Chen & Lin, Sarma et. al. & theory

Figure 3.35 a shows the graph obtained from the methods of Ramesh & Mangal, Patterson & Wang, Ajovalasit et. al. and theory for the line at y/R = 0.5 It shows that the results obtained by the methodologies of Patterson & Wang and Ajovalasit are having sharp hikes. Thus the results obtained are not good. The results obtained by Ajovalasit et. al. are having lesser hikes than Patterson and Wang. This is because of error compensation by using left and right circularly polarized light being used for model illumination. But it is clear that error is not fully compensated. Results by Ramesh and Mangal are closer to the theoretical line. Figure 3.35b shows the graphs obtained from the methods of Brown & Sullivan, Kihara, Dupre et. al. and theory for the line at y/R = 0.5. It shows that the results obtained by Kihara's technique are having sharp hikes, the data follows the trend of the theoretical line in between the hikes. However the results obtained are far from satisfactory. The results obtained by Dupre et. al. are not correct. Results by Brown and Sullivan are closer to the theoretical line. Figure 3.35 c shows the graphs obtained from the methods of Chen & Lin (without adjustment and with adjustment), Sarma et. al. and theory for the line at y/R = 0.5. It shows that the results

obtained by Sarma et.al. technique are having sharp hikes. Thus the results obtained are not good at some portions and on some portions they are close to the theoretical data.. The results obtained by Chen & Lin with adjustment are good and follow the theoretical curve closely. Chen and Lin without any adjustment is not good at some portions and are good in some other portions. Along line at y/R = 0.5 theta is not beyond the range – $\pi/4$ to $+\pi/4$ and hence the utility of these algorithms for a generic situation is not fully varified.

Hence the study was done for the line at y/R = 0.25. Along this line, the theoretical value of θ lies in the range of $-\pi/2$ to $+\pi/2$. Here the results are similar to what has been observed previously. However none of the algorithms give correct value of θ beyond – $\pi/4$ to $+\pi/4$ range.

3.7. Closure

Study of intensity patterns is carried out for the understanding of numerical inaccuracies involved in the isoclinic parameter calculations. The theoretical possibility of arriving at the correct and unwrapped value of isoclinic parameter by using isochromatic parameter is considered. The quality of isoclinic data in circular polariscope for different loads is studied. Using isoclinics from low loads in circular polariscope is recommended. It has been reconfirmed that plane polariscope give a comparatively better isoclinic parameter even at higher loads as compared to the circular polariscope.

From the study conducted in this chapter it is reaffirmed that the results obtained in plane polariscope are better than in circular polariscope. In circular polariscope, the method by Ajovalasit et. al. is found to be better as compared to the method by Patterson & Wang. Even though theoretically the principle stress directions remain constant with respect to the load, experimentally they are distorted at higher loads. In plane polariscope techniques, Ramesh & Mangal, Brown & Sullivan give better results. Method of Chen & Lin also gives good results but an adjustment is required. Methods of Dupre et. al. & Sarma et. al. are not giving satisfactory results. Besides this the theta obtained in all algorithms is wrapped and is in the range of $-\pi/4$ to $+\pi/4$, thus unwrapping is still required from these algorithms.

CHAPTER 4

CONCLUSIONS AND SUGGESTIONS FOR FUTURE WORK

4.1 Conclusion

The main aim of this thesis is to understand the nature and evaluation of isoclinic parameter by PST methods. Methods to improve theta by quadrant method helped in correcting the phase map only for particular cases. The use of logical NOT has showed a way for correcting phase map for any generic problem. However, the method demands identifying the zones for correction interactively.

It is established in the thesis that the orientation of model slow and fast axis has a significant effect on the final result of phase map. The study has showed that one can get a complementary phase map either by changing the direction of loading or by just swapping the intensities I_3 & I_5 and I_4 & I_6 in the calculations. This has led to another study wherein the unwrapping of θ based on intensity information has been carried out. However, due to interaction of δ as well as θ, it was not possible to identify whether one has model fast axis or slow axis at the point of interest based on intensity information alone. A method to get θ correctly in the range $-\pi/2$ to $+ -\pi/2$ has been developed provided δ is known for the problem a priori. The method has been shown to work based on theoretical data. Further refinement is required to apply it for practical situations.

A comparative study on the evaluation of θ by various phase shifting methods in circular polariscope, plane polariscope and polarization stepping method have been carried out. The study showed that, in circular polariscope, the method by Ajovalasit et. al. is found to be better as compared to the method by Patterson & Wang. Even though theoretically the principle stress directions remain constant with respect to the load, experimentally they are distorted at higher loads. In plane polariscope techniques,

Ramesh & Mangal, Brown & Sullivan give better results. Method of Chen & Lin also gives good results but an adjustment is required. Methods of Dupre et. al. & Sarma et. al. are not giving satisfactory results. Besides this the theta obtained in all algorithms is wrapped and is in the range of $-\pi/4$ to $+\pi/4$, thus unwrapping is still required from these algorithms.

4.2.Suggestion for Future Work

1. Theoretically isoclinic parameter does not change with change in load. But experimentally in circular polariscope isoclinic get distorted at higher loads as compared to lower loads under similar conditions. It will be useful to understand the exact reason for this anomaly. Note that in plane polariscope, isoclinics are good even at higher loads.
2. It has been found that background intensity and incident light plays an important role in the accuracy of results. Special efforts can be taken to minimize the background intensity and to have a uniform incident intensity over the model.
3. An interpolation – extrapolation technique can be developed to unwrapp theta based on monitoring the phase changes while processing
4. Special attention should be given to develop the equations and methods which will give θ directly in the range of $-\pi/2$ to $+\pi/2$.

REFERENCES

1. Ramesh K. Digital Photoelasticity: Advanced Techniques and Application. Springer – verlag, Berlin, Germany, 1999.
2. Buckberry, C. and Towers, D. New approach to the full-field analysis of photoelastic stress patterns. Optics and Lasers Engg, 1996, 24, 415-428.
3. Ekman MJ, Nurse AD (1998) Completely automated determination of two-dimensional photoelastic parameters using load stepping. Opt Engng 37(6): 1845–1851
4. Quiroga JA, Gonazalez-Cano A (1997) Phase measuring algorithm for extraction of isochromatics of photoelastic fringe patterns. Appl Optics 36(32):8397-8402
5. Mangal S. K., Data Acquision in Digital Photoelasticity by Phase Shifting Techniques, Ph.D. Thesis, I.I.T. Kanpur, September 1999.
6. Tamrakar D. K., Digital Photoelastic Analysis on MIL Platform. M.Tech. Thesis, Dept. of Mech. Engg., I.I.T. Kanpur, (1999).

A130863

A130863

Date Slip

This book is to be returned on the date last stamped.

.....	.....
.....	.....
.....	.....
.....	.....
.....	.....
.....	.....
.....	.....
.....	.....
.....	.....
.....	.....
.....	.....
.....	.....